Supplementary Figures & Figure Captions

Figure SM1. Combined x-ray elemental maps in Mg (red), Ca (green), and Al (blue) of several type 3 ordinary, CO and CV carbonaceous chondrites discussed in the paper. Images from Krot et al. (2014a).

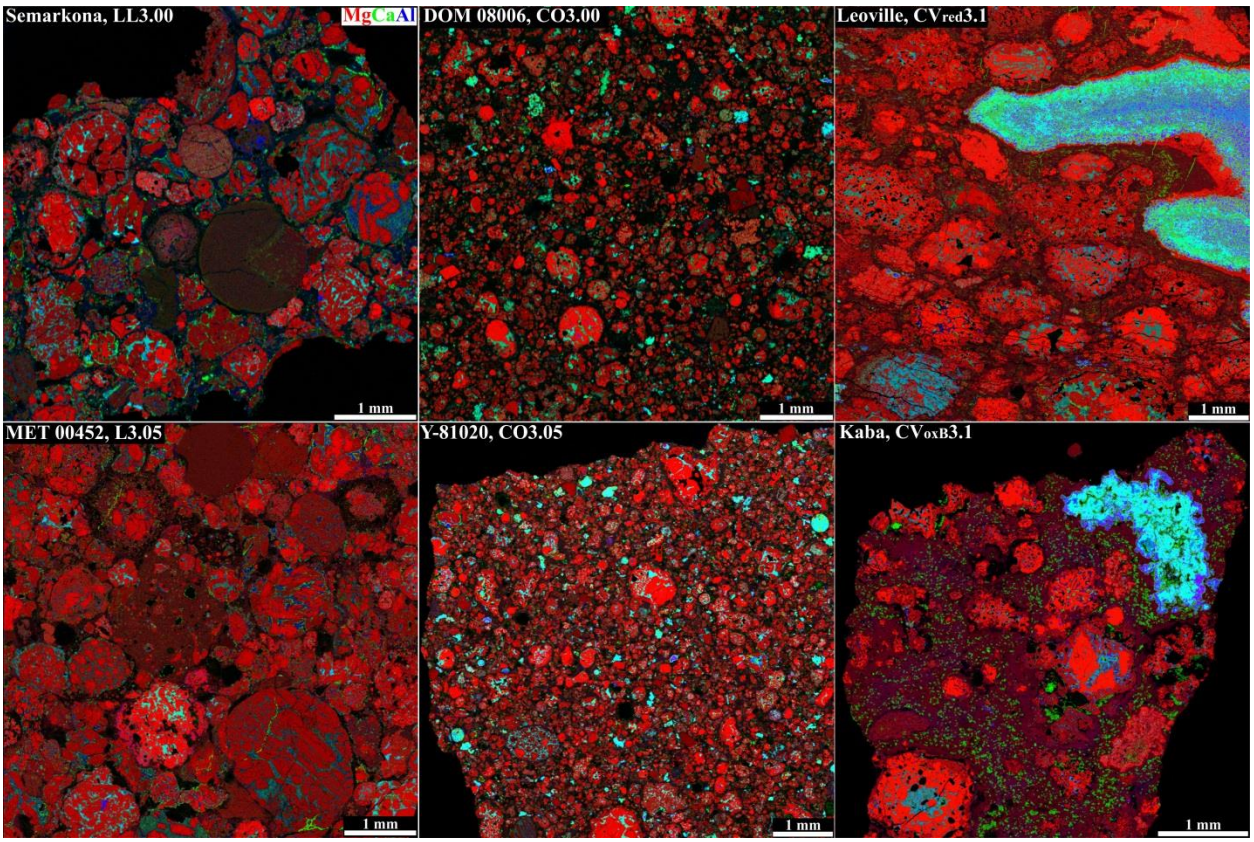

Figure SM2. Transmission electron (a) and backscattered electron images (b–f) of FeNi-carbides and magnetite in Semarkona (LL3.00), DOM 08006 (CO3.00), and Vigarano (CV_{red}3.1). (a,b) FeNi-carbide±FeNi-metal are corroded by magnetite. (c–f) FeNi-metal nodules in chondrules are replaced and overgrown by magnetite. Fine-grained chondrule rims are crosscut by FeNi-carbide–magnetite veins. Regions outlined in (c) and (e) are shown in detail in (d) and (f), respectively. Figures from Dobrică & Brearley (2011, 2020) & Krot et al. (2022a).

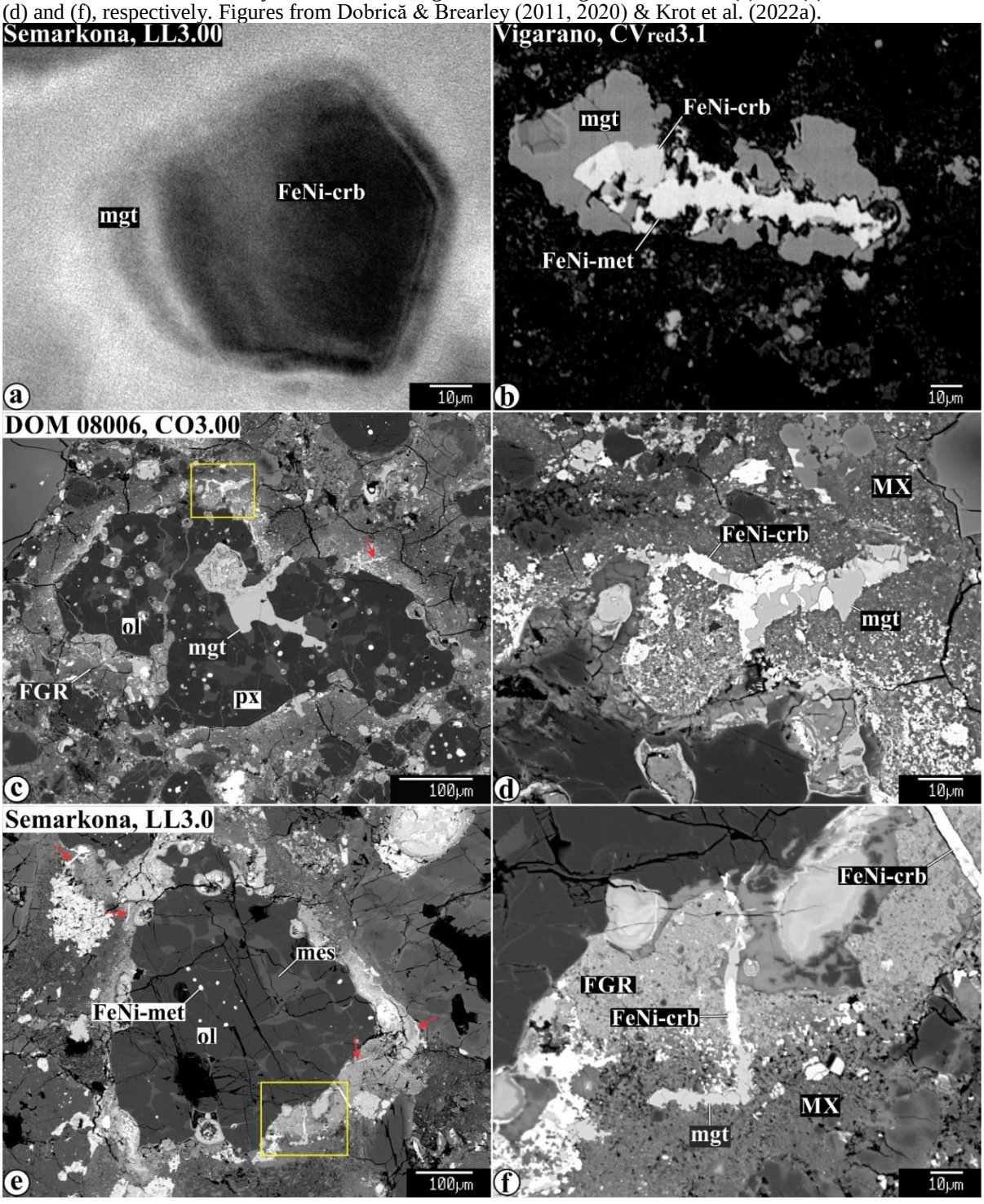

Figure SM3. TEM (a,b) and BSE (c,d) images of phyllosilicates (phyl) and ferroan olivine (fa) replacing amorphous silicates (am) in matrices of Semarkona (LL3.00) and EET 90161 (L3.05).

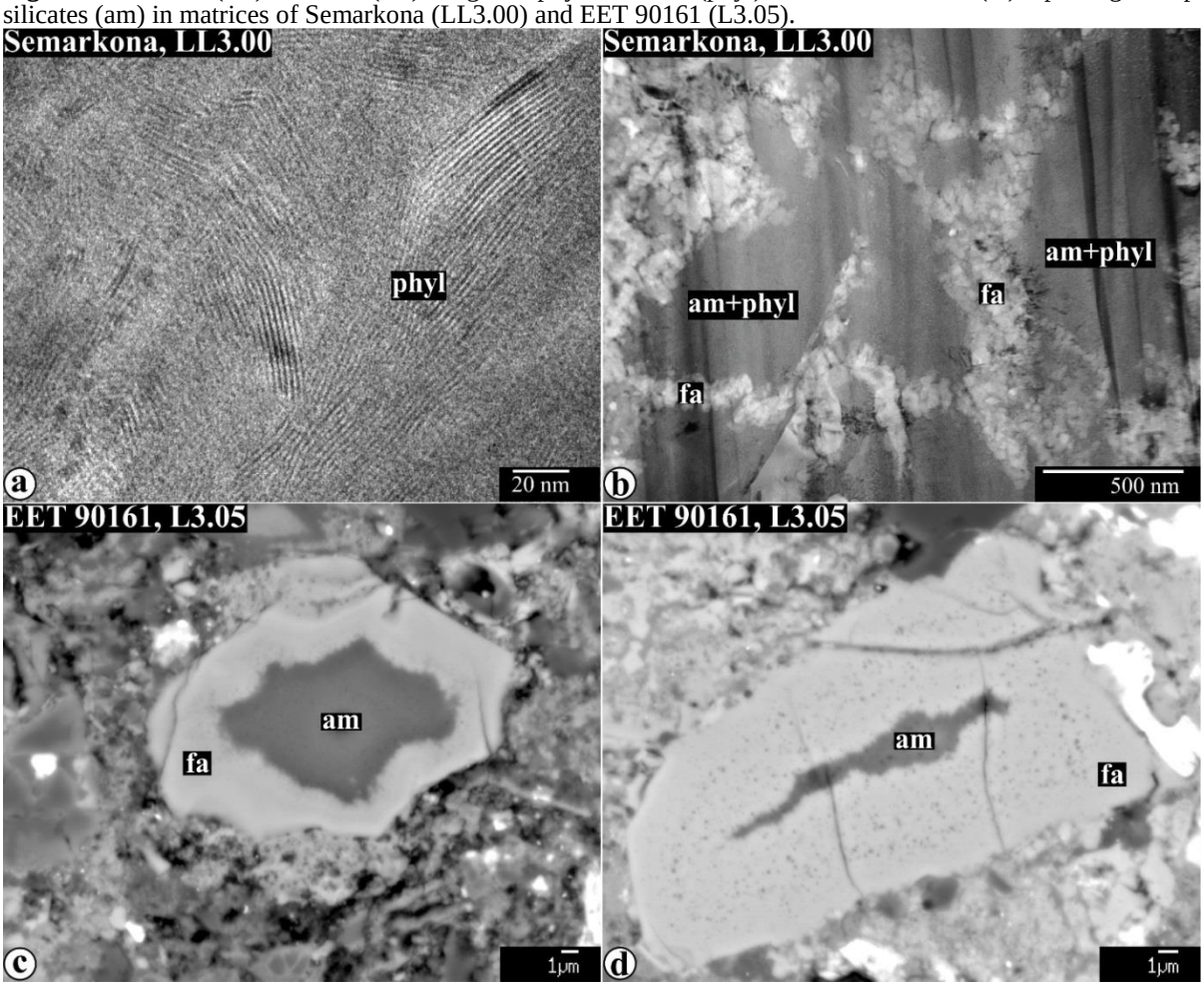

Figure SM4. BSE images of fayalite replacing magnetite in matrix of MAC 88107 (CO3.1) and in chondrule of Kaba (CVoxB3.1). FeNi-metal±sulfide nodules in Kaba chondrule are replaced by "dirty" magnetite and overgrown by "clean" magnetite with elongated inclusions of troilite. Only the clean magnetite is corroded by fayalite.

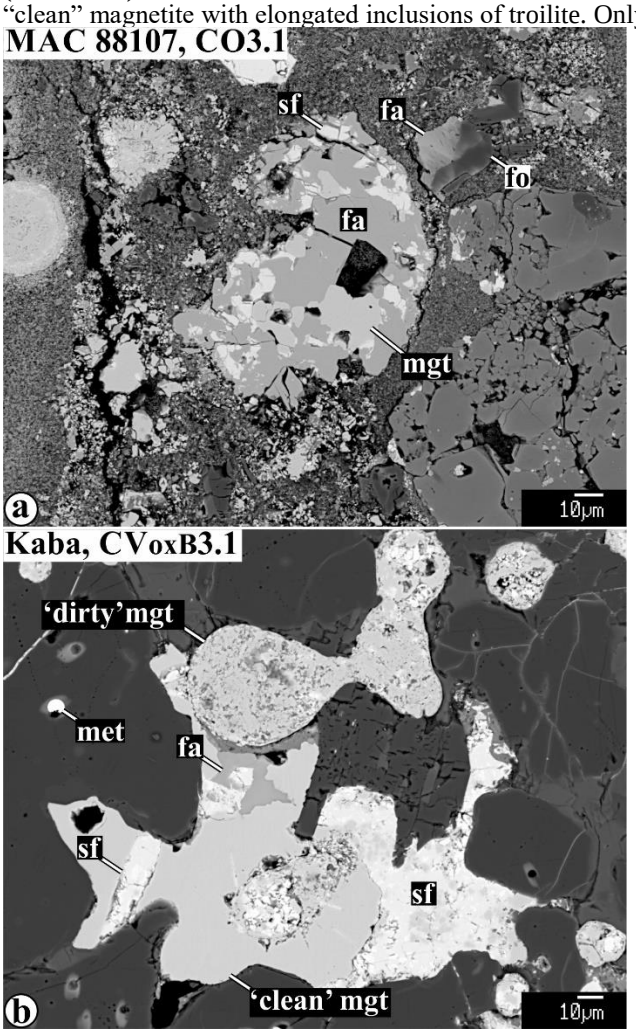

Figure SM5. BSE images of textural occurrences of secondary fayalite in (a–c) Kaba (CVoxB3.1) and MAC 88107 (CO3.1). (a,d) Fayalite+hedenbergite±magnetite overgrowing ferroan olivine chondrule phenocrysts. (b,e) Fayalite-magnetite-sulfide veins crosscutting fine-grained rims around chondrules. (c,f) Coarse fayalite±hedenbergite grains in matrix (MX).

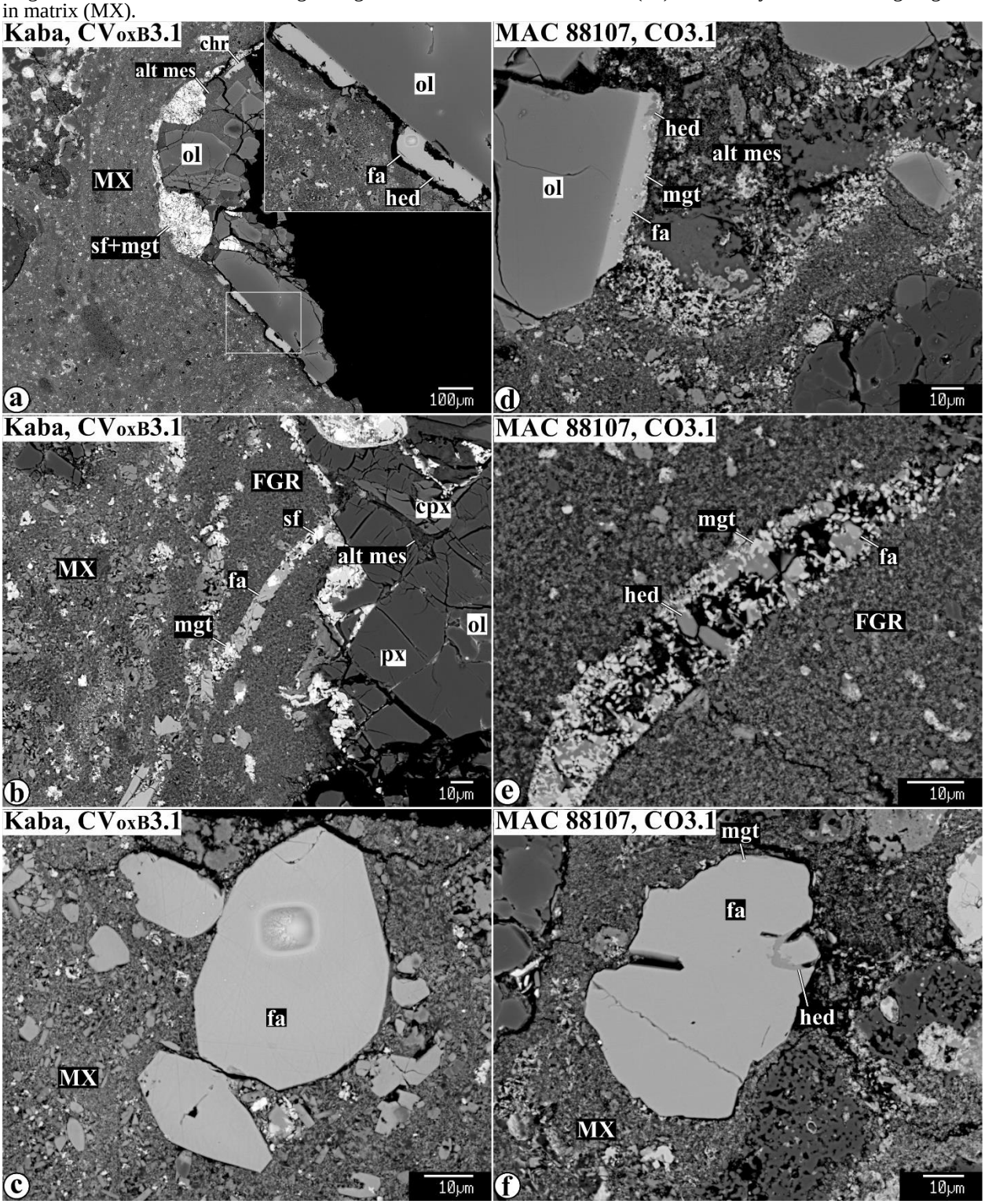

Figure SM6. BSE images of textural occurrences of fayalite in Semarkona (LL3.00). (a) Fine fayalite grains in the matrix and fayalite overgrowing magnesian olivine of a chondrule fragment. (b) Fayalite overgrowing troilite. (c) Fayalite grains in a peripheral part of fine-grained matrix-like rim around magnesium porphyritic chondrule.

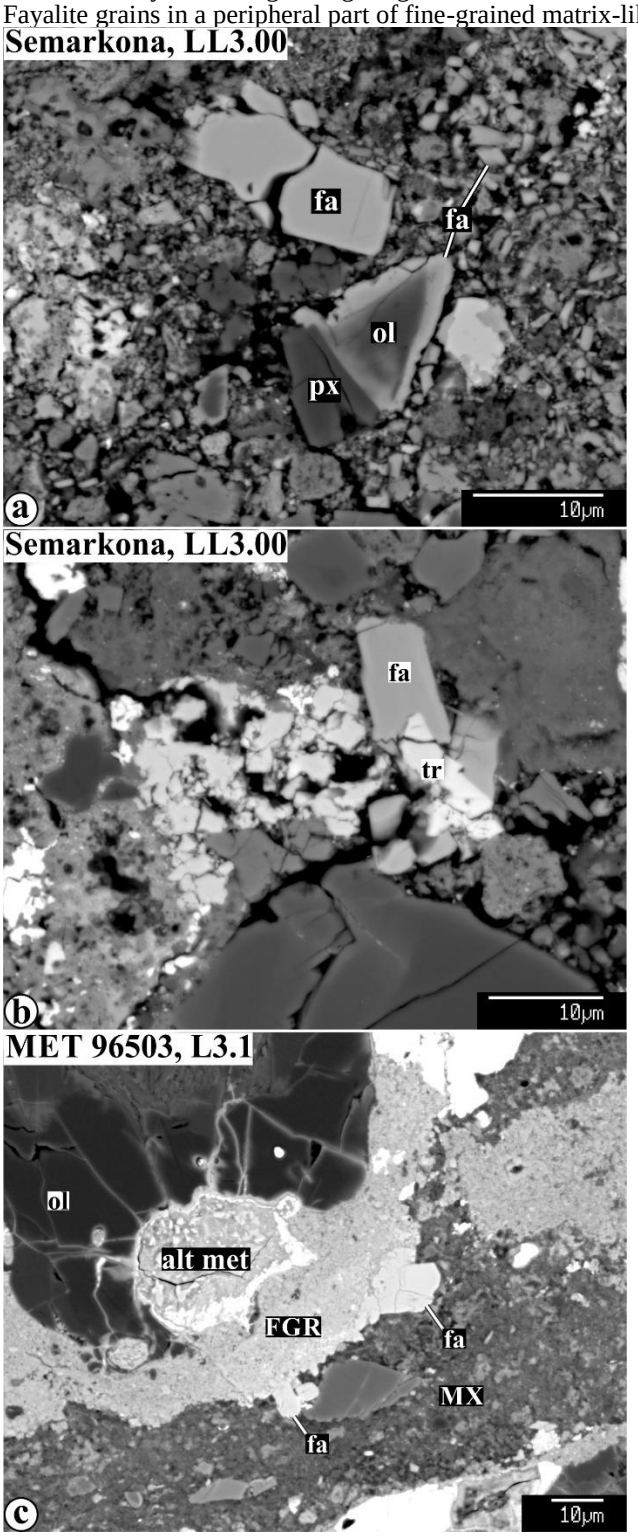

Figure SM7. BSE images of kirschsteinite in (a) MAC 88107 (CO3.1) and (b) Vigarano (CVred3.1). (a) Kirschsteinite associated with fayalite and hedenbergite in the matrix. (b) A layer of kirschsteinite grains separating altered Ca,Al-rich inclusion and fine-grained matrix. The kirschsteinite grains are chemically zoned with peripheral parts composed of kirschsteinite-monticellite solid solution. Images from Krot et al. (2000) and MacPherson et al. (2017).

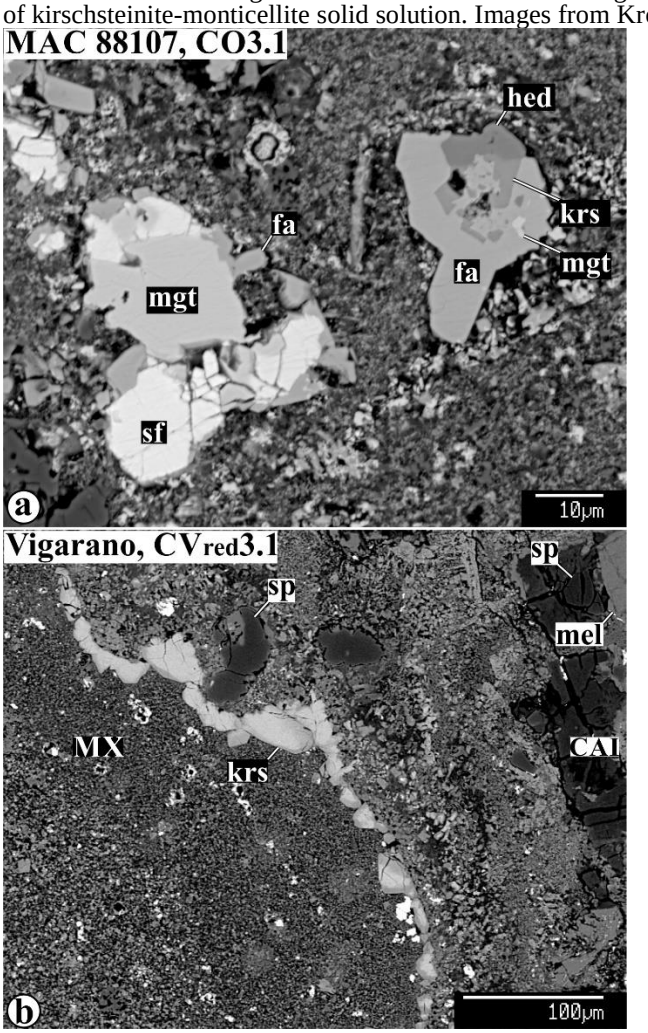

Figure SM8. BSE images of secondary Zn-bearing hercynite (Zn-hrc) replacing grossite (grs) and krotite (krt) in a CAI from Y-81020 (CO3.05). cpx:Al-diopside; hib:hibonite; mel:melilite; pv:perovskite; sp:spinel. Images from Krot et al. (2022b).

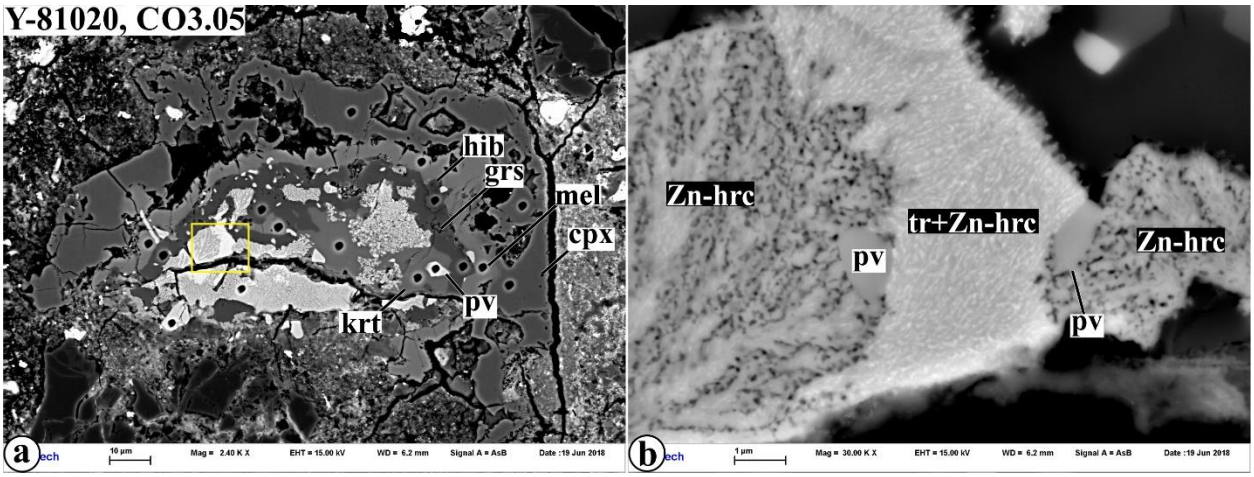

Figure SM9. Combined (RGB) x-ray elemental maps in (a) Ti, Ca, and Al, (b,c) Mg, Ca, and Al, and (d) Cl, Na, and Mg and (e,f) BSE images of major textural types of igneous CAIs from Allende: (a) Compact Type A (CTA), (b) Forsterite-bearing Type B (FoB), and (c–f) Type B. The CAIs are composed of melilite, spinel, fassaite, ±anorthite, and ±forsterite, are surrounded by Wark-Lovering (WL) rim, fine-grained matrix-like rim (FGR), and Ca,Fe-rich silicate layer (CaFe-sil). Secondary Na- and/or Cl-bearing minerals in the Type B CAI show zoned distribution: wadalite (wad) is concentrated in its core; sodalite (sod) and nepheline (nph) occur preferentially in its outer part. The fine-grained rim consists mainly of ferroan olivine (fa) and nepheline; the Ca,Fe-rich silicate layer consist of salite-hedenbergite pyroxenes (sal-hed), andradite (andr), and wollastonite (wol). From Krot et al. (2021).

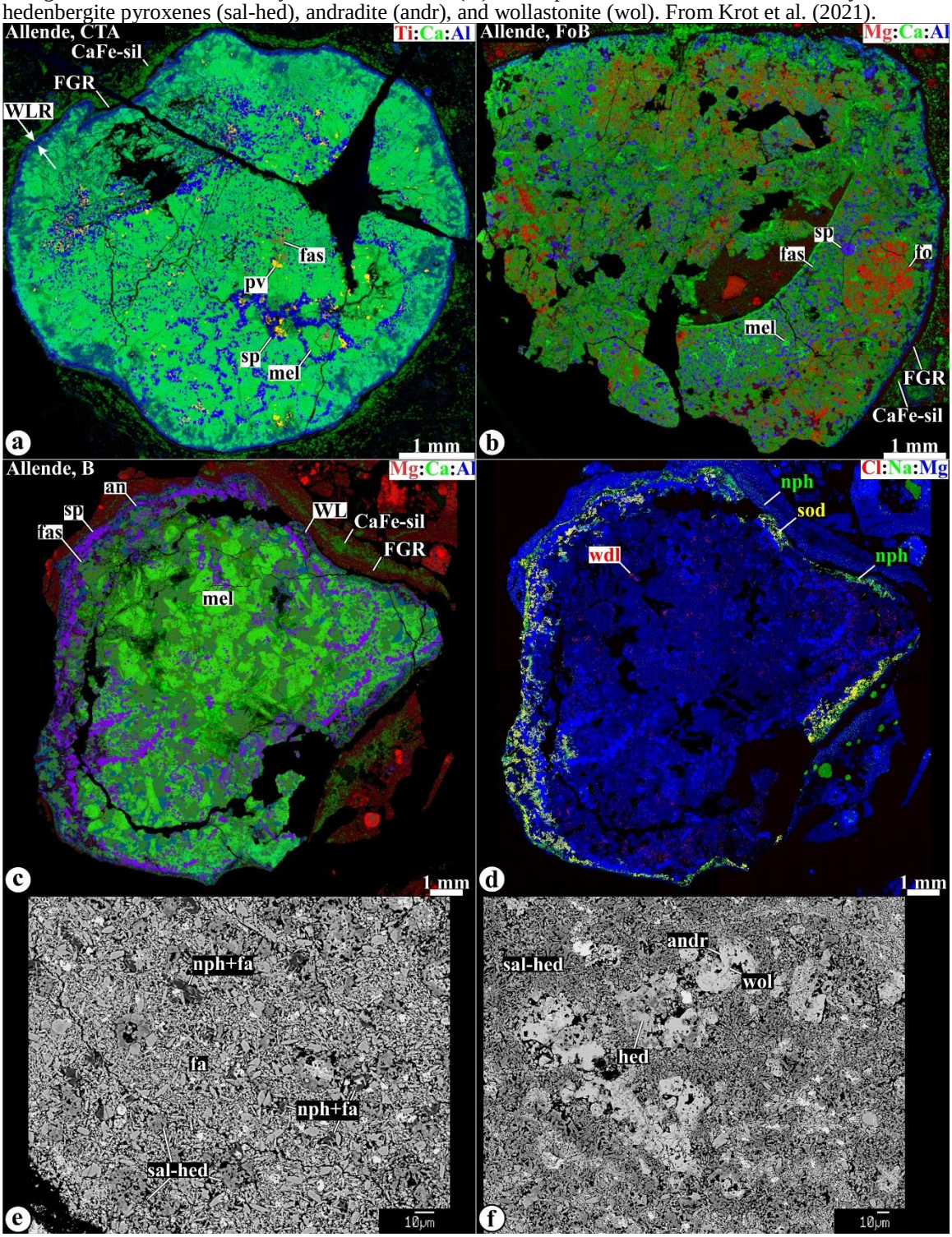

Figure SM10. BSE images of secondary calcite (cal), clintonite (cln), grossular (grl), monticellite (mnl), monticellite-kirschsteinite solid solution (mnl-krs), tilleyite (tlt), and wollastonite (wol) in the Allende igneous CAIs. These minerals formed in the presence of H_2O-CO_2-bearing fluid. From Krot et al. (2021).

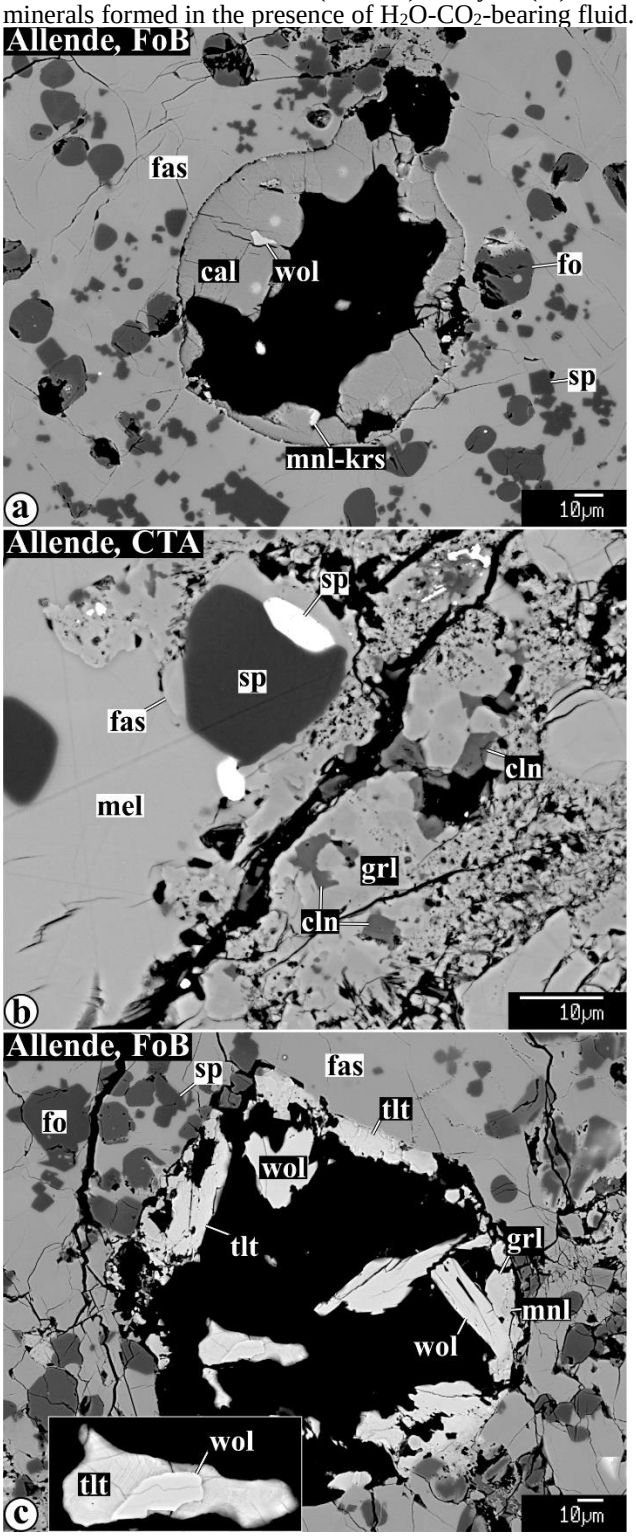

Figure SM11. BSE images of secondary minerals (anorthite, dmisteinbergite, grossular, kushiroite, monticellite, Na-melilite, wadalite) in the Allende igneous CAIs. The secondary minerals precipitate in veins and open spaces of primary melilite and anorthite and suggest formation during dissolution-precipitation from an aqueous fluid. From Krot et al. (2021).

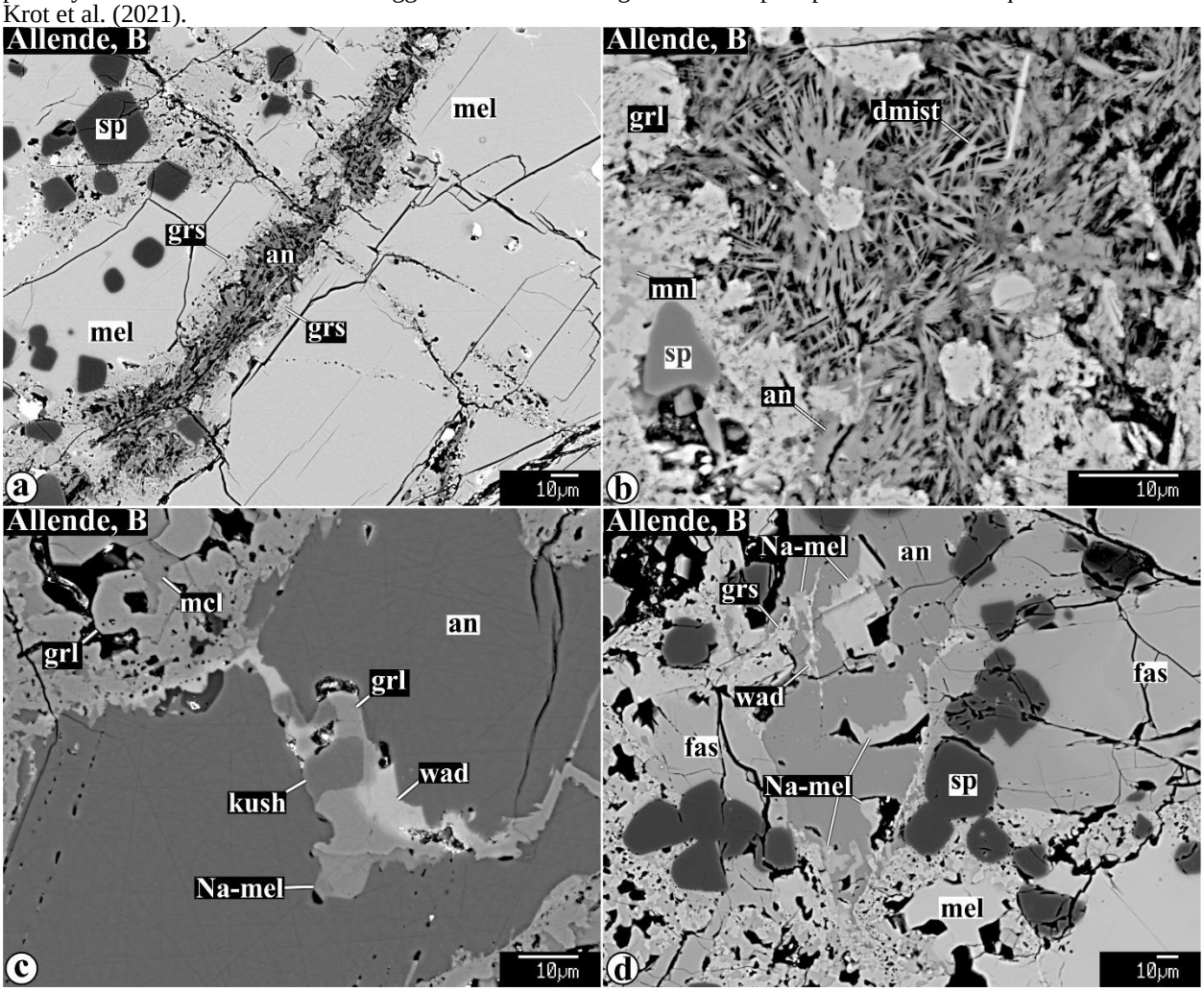

Figure SM12. BSE images of secondary mineral assemblages replacing gehlenitic melilite in the Allende CTA CAIs – (a) grossular + anorthite, (b) grossular + spinel, and (c) grossular + corundum + nepheline. From Krot et al. (2021).

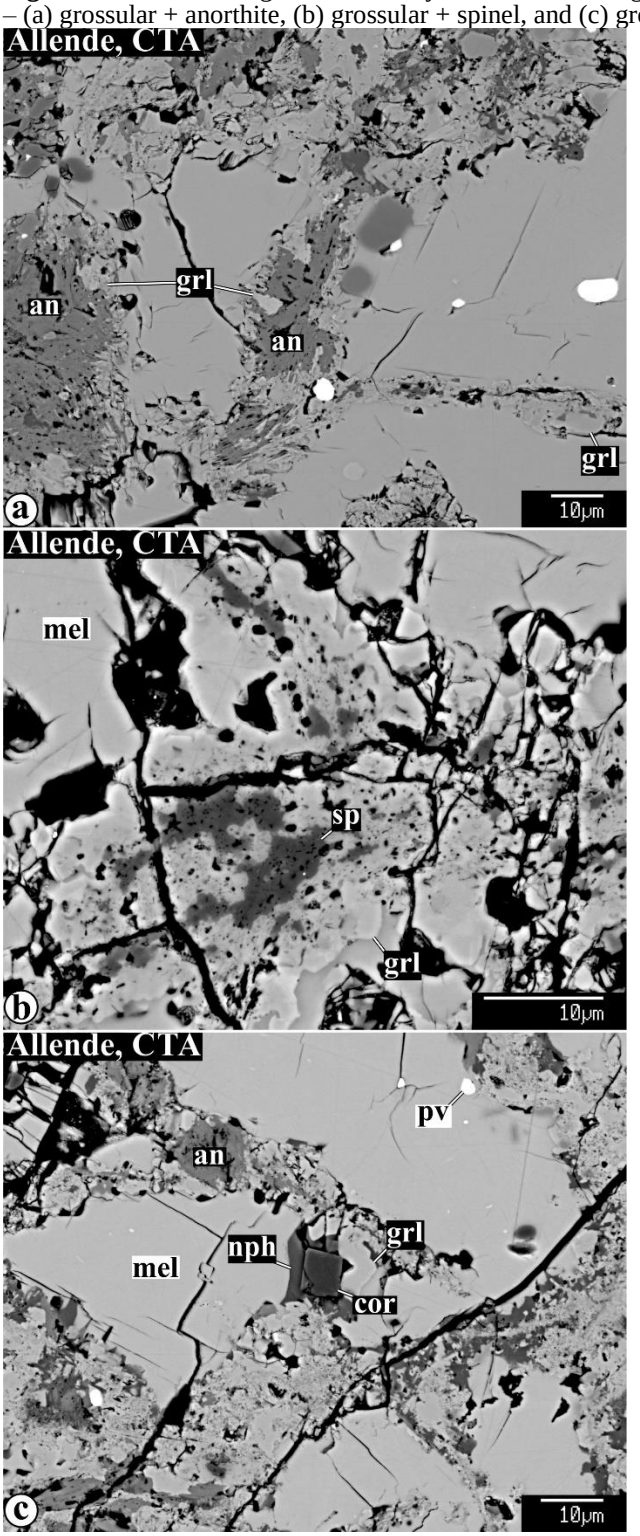

Figure SM13. BSE images of secondary mineral assemblages, (b) grossular + Al-diopside and (c) grossular +_monticellite, replacing åkermanitic melilite in the Allende Type B CAIs. Regions outlined in "a" are shown in detail in "b" and "c". From Krot et al. (2021).

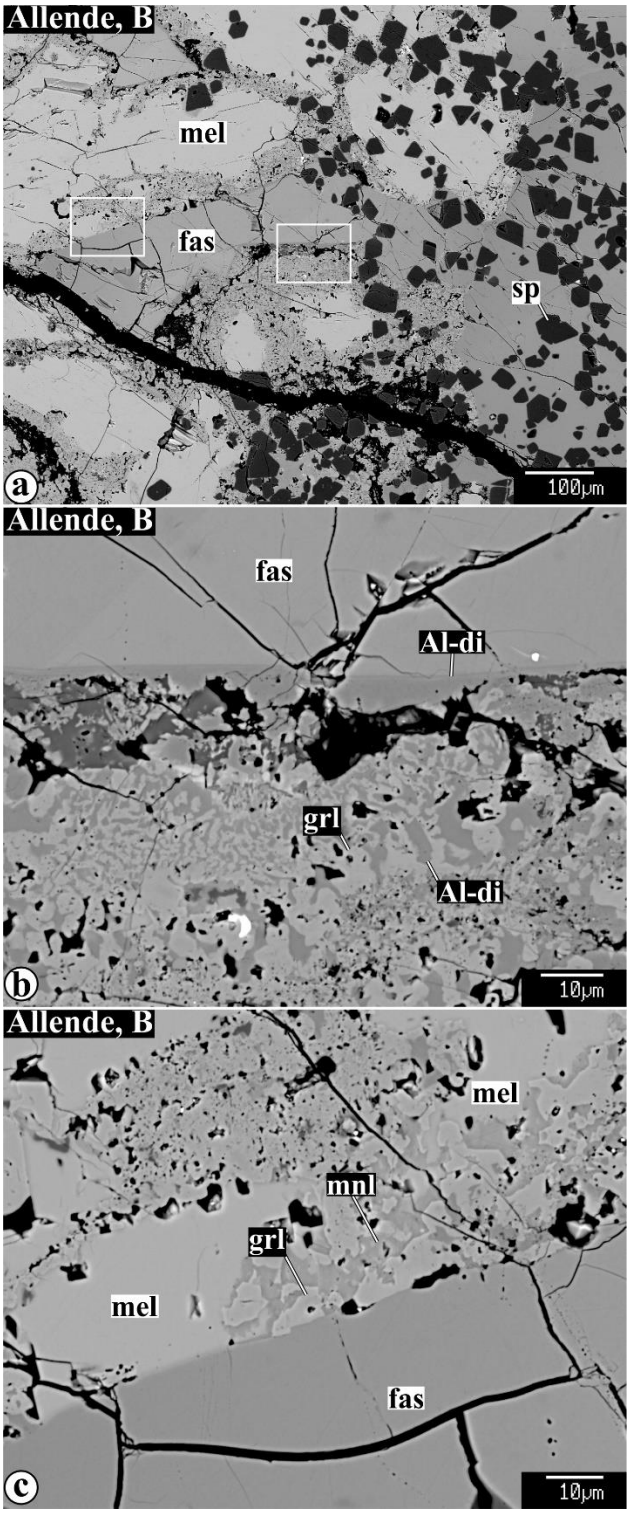

Figure SM14. BSE images of secondary mineral assemblages illustrating multistage alteration of Allende CAIs. (a) Åkermanitic in a core of a FoB CAI is replaced by grossular+monticellite+wollastonite and minor Na-melilite. (b) In the peripheral part of the same CAI, grossular and monticellite are preferentially replaced by Al-diopside. (c) In Type B2 CAIs, the secondary mineral assemblage of grossular+monticellite+wollastonite replacing åkermanitic melilite is crosscut by a vein of monomineralic wollastonite. From Krot et al. (2021).

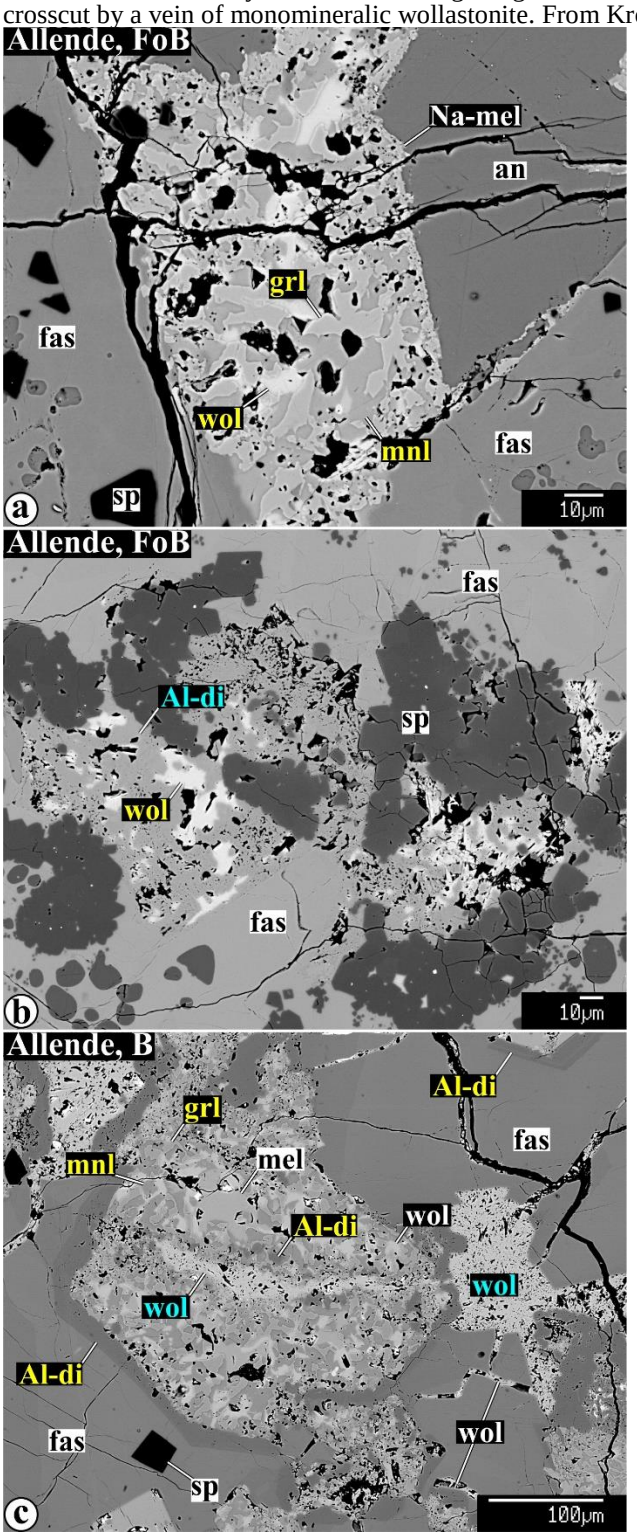

Figure SM15. BSE images of secondary minerals in the Allende igneous CAIs that recorded changes of chemical compositions of metasomatic fluid. (a) Grossular overgrown by layers of more Fe-rich grossular. (b) Monticellite overgrown by Fe-rich monticellite (kirschsteinite-monticellite solaid solution). (c) Chemically-zoned Al-diopside overgrown by hedenbergite and andradite. (d) Grossular overgrown hutcheonite. From Krot et al. (2021).

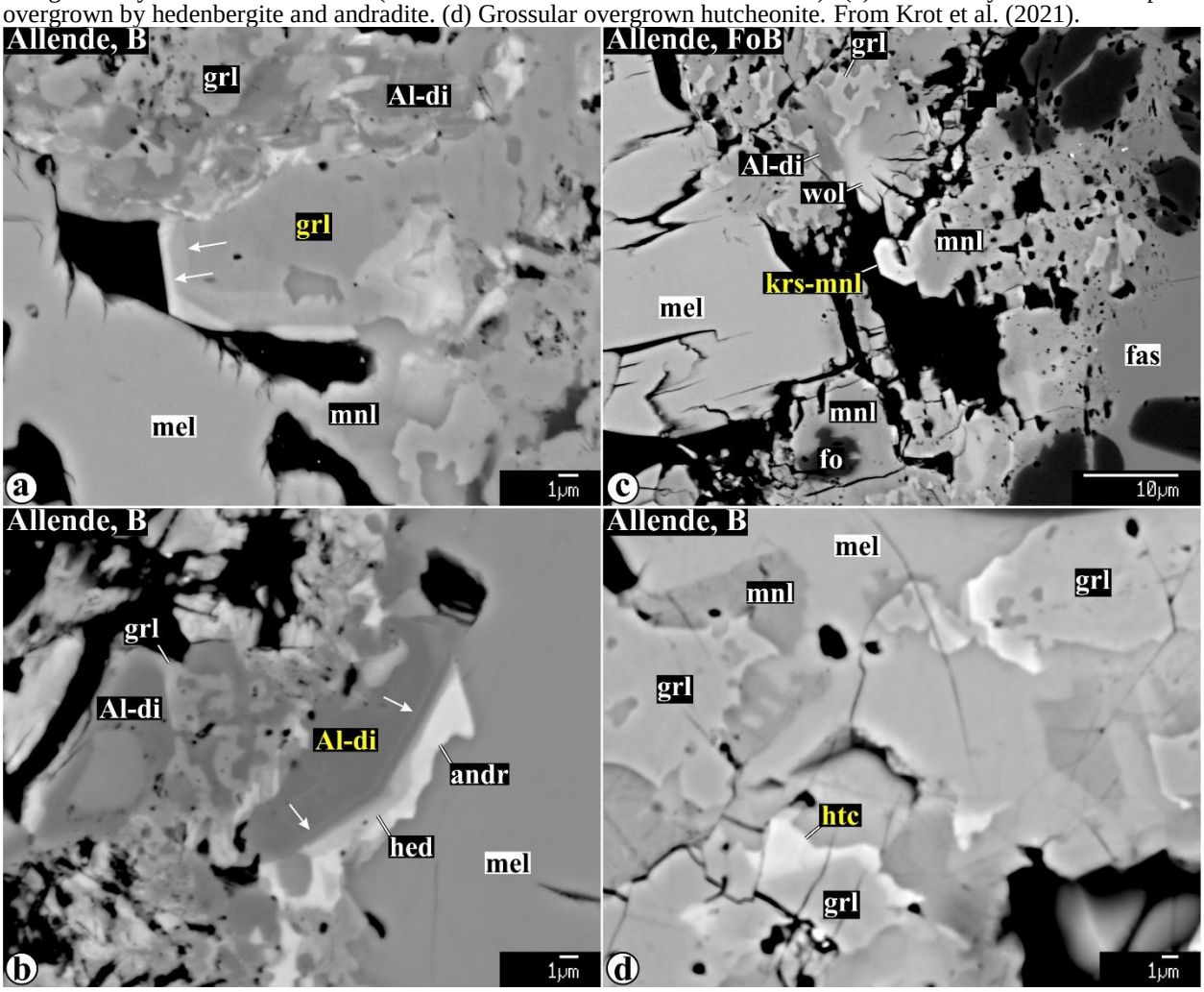

Figure SM16. Combined (RGB) x-ray elemental maps in (a,c,e,) Mg, Ca, Al, (b,d) Ti, Ca, Al, and (f) elemental map in Ti of CK3 igneous (CTA, B, FoB) CAIs. The CAIs consist of coarse-grained primary minerals: anorthite (an), fassaite (fas), forsterite (fo), grossmanite (grs), hibonite (hib), rhönite (rhn), perovskite (pv), and spinel (sp); melilite is nearly completely replaced by secondary minerals (sec). The CAIs are surrounded by Wark-Lovering rims and a layer of CaFe-rich silicates (for details see Figs. SM13–15). From Krot et al. (2024).

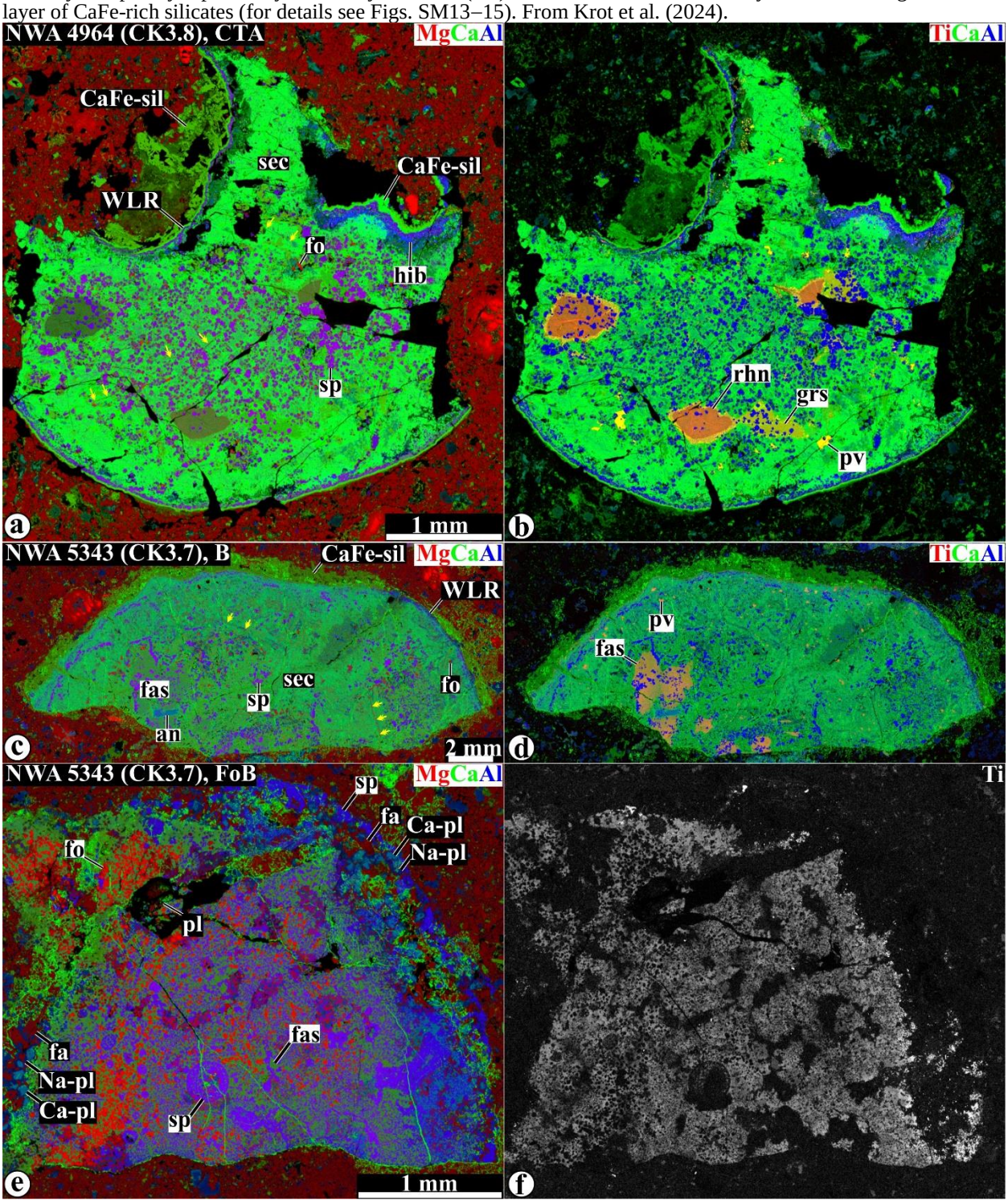

Figure SM17. BSE images of primary and secondary minerals in the CTA CAI from NWA 4964 (CK3.8) (see Figs. SM12a,b). The CAI consists of primary grossmanite, spinel, hibonite, perovskite, rhönite, and very minor melilite that is nearly completely replaced by grossular (grl), FeAl-diopside (Al-di), and minor spinel (sp), clintonite (cln), and forsteritic olivine (fo). Grossmanite is corroded by FeAl-diopside, ilmenite (ilm), sphene (sph), and clintonite. Coarse secondary grossular and FeAl-diopside are overgrown Ti-bearing grossular and Al-diopside, respectively. The CAI is overgrown by a CaFe-rich silicate layer composed of chemically-zoned Fe and Ti-bearing grossular and Al-diopside. From Krot et al. (2024).

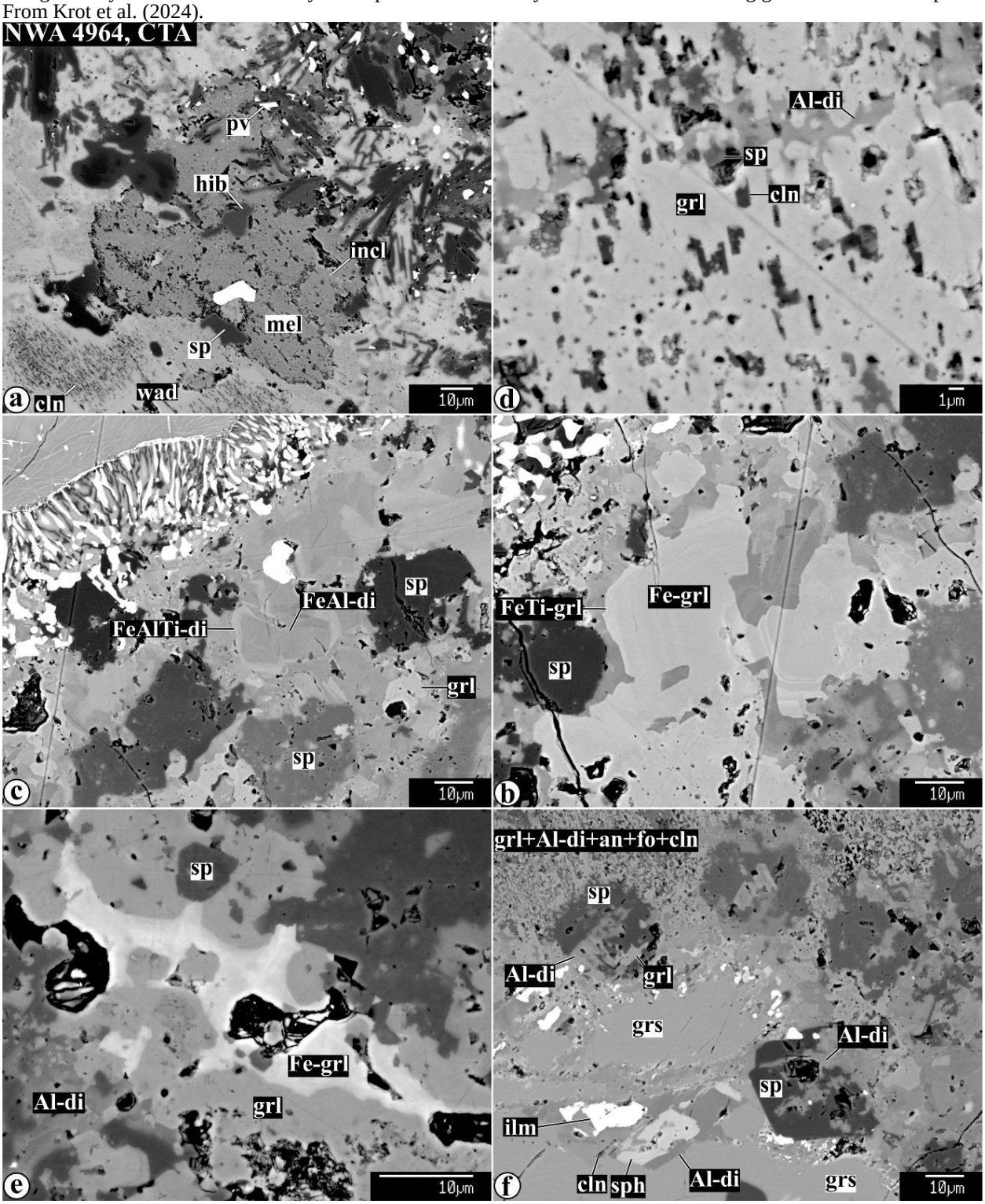

Figure SM17 (cont.).

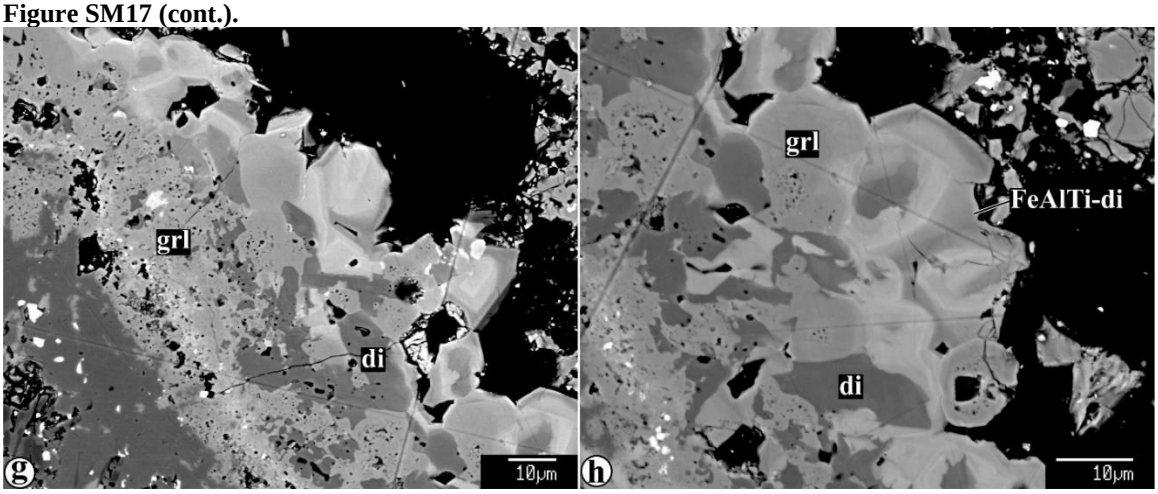

Figure SM18. BSE images of primary and secondary minerals in the Type B CAI from NWA 5343 (CK3.7) (see Figs. SM12c,d). Region outlined in "c" is shown in detail in "d". The CAI consists of primary fassaite, anorthite, and spinel; melilite is completely replaced by grossular (grl), Fe-bearing grossular (Fe-grl), Al-diopside (Al-di), and FeMg-olivine (ol). Fassaite is corroded and crosscut by veins of Ti-bearing grossular (Ti-grl), Fe-bearing fassaite (Fe-fas), Al-diopside, and minor sphene (sph), spinel (sp), and clintonite (cln). Anorthite is only slightly corroded by grossular with minor spinel and clintonite. The CAI is crosscut by veins of ferromagnesian olivine and plagioclase. It also contains a geode partly filled by Al-diopside, plagioclase, FeMg-olivine, and Fe-bearing grossular. From Krot et al. (2024).

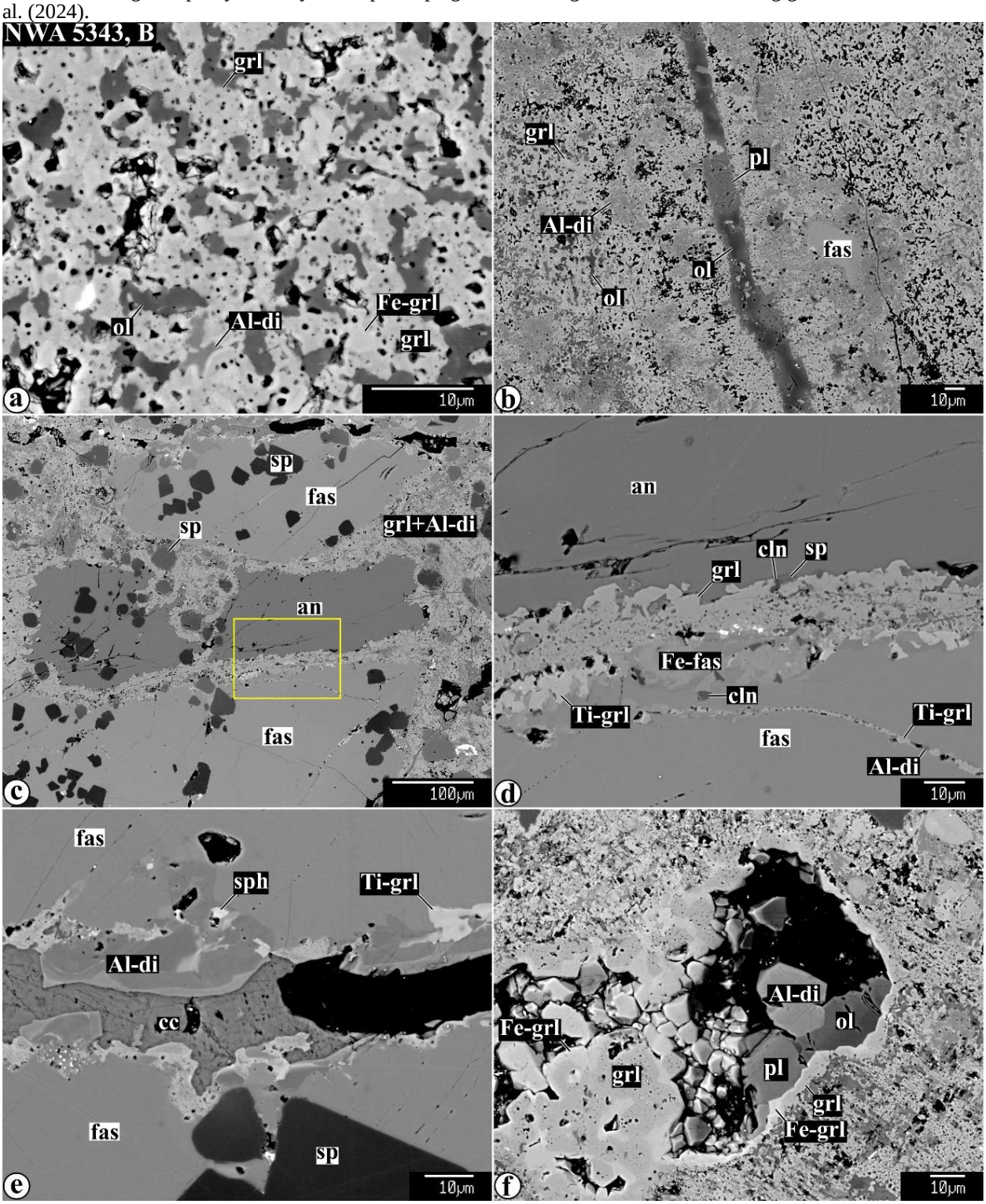

Figure SM19. BSE images of primary and secondary minerals in the FoB CAI from NWA 5343 (CK3.7) (see Figs. SM12e,f). Region outlined in "a" is shown in detail in "b". The CAI consists of primary spinel, forsterite, Al,Ti-diopside, and minor anorthite; melilite is absent. (a, b) In the CAI core, melilite and/or anorthite are replaced by FeAl-diopside (FeAl-di), grossular (grl), anorthite (an), and Na-bearing plagioclase (Na-pl). (c, d) In the CAI mantle, most likely melilite is replaced by coarse ferroan olivine (Fa_{35}) and chemically-zoned plagioclase having Ca-rich cores ($An_{90–99}$) and Na-rich peripheries ($Ab_{79–85}$). From Krot et al. (2024).

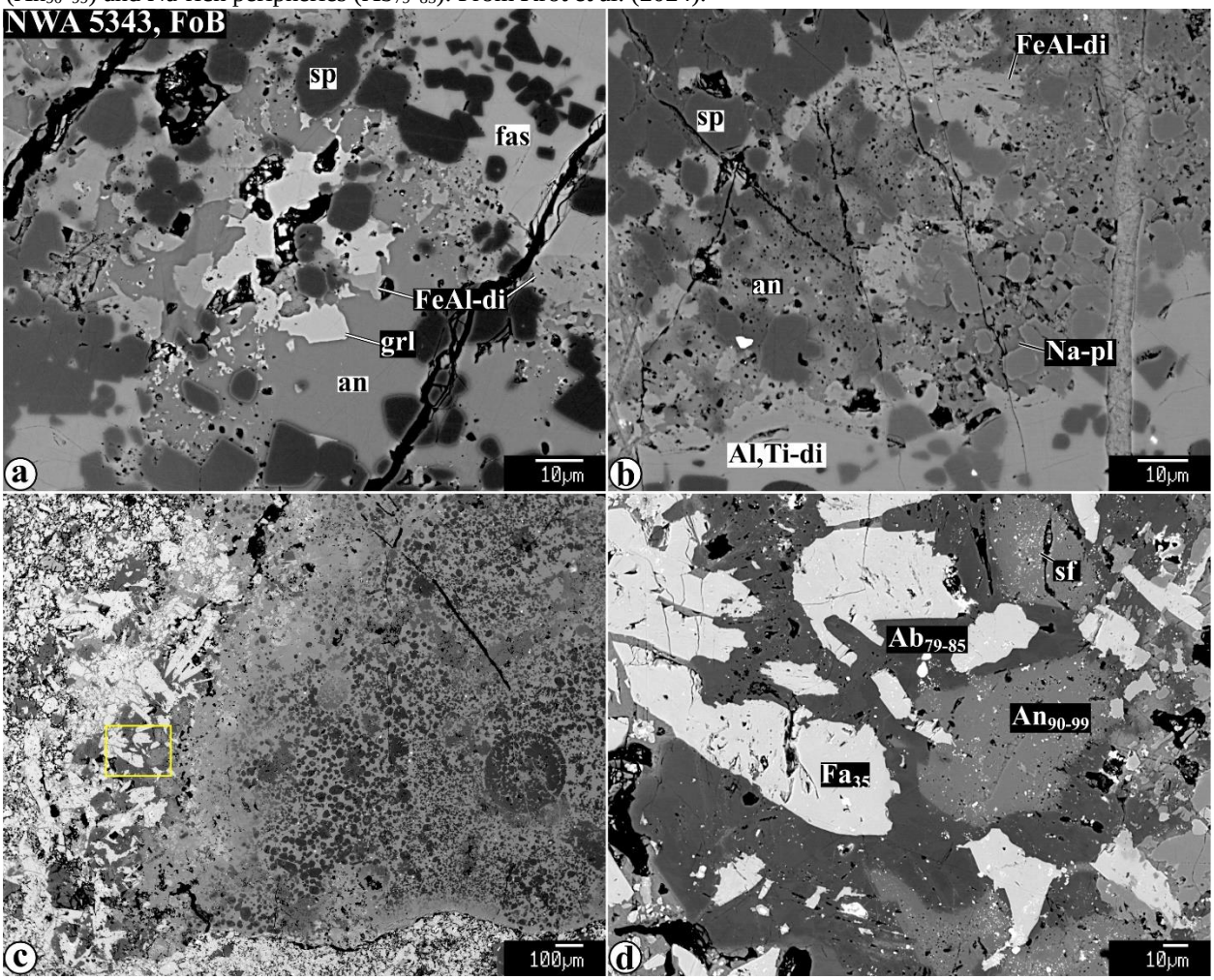

Figure SM20. (a–c) X-ray elemental maps in Ca and (d) BSE image of the Allende dark inclusions (DI) *4302-1*, *IV-1*, and *3b-1* composed entirely of the secondary minerals, mainly ferroan olivine and CaFe-pyroxenes. Dark inclusions contain abundant chondrule pseudomorphs (indicated by yellow stars in "a–c" and shown in "d"). The inclusion *4302-1* is crosscut by multiple CaFe-pyroxene veins (indicated by arrows in "a". All three inclusions are surrounded by CaFe-silicate rims composed of salite-hedenbergite pyroxenes, andradite, and minor kirschsteinite. The inclusions experienced extensive metasomatic alteration prior to incorporation into the Allende host. Subsequently, they experienced *in situ* alteration that resulted in removal of Ca to various degrees that was used to form CaFe-silicate rims around them. From Krot et al. (2001).

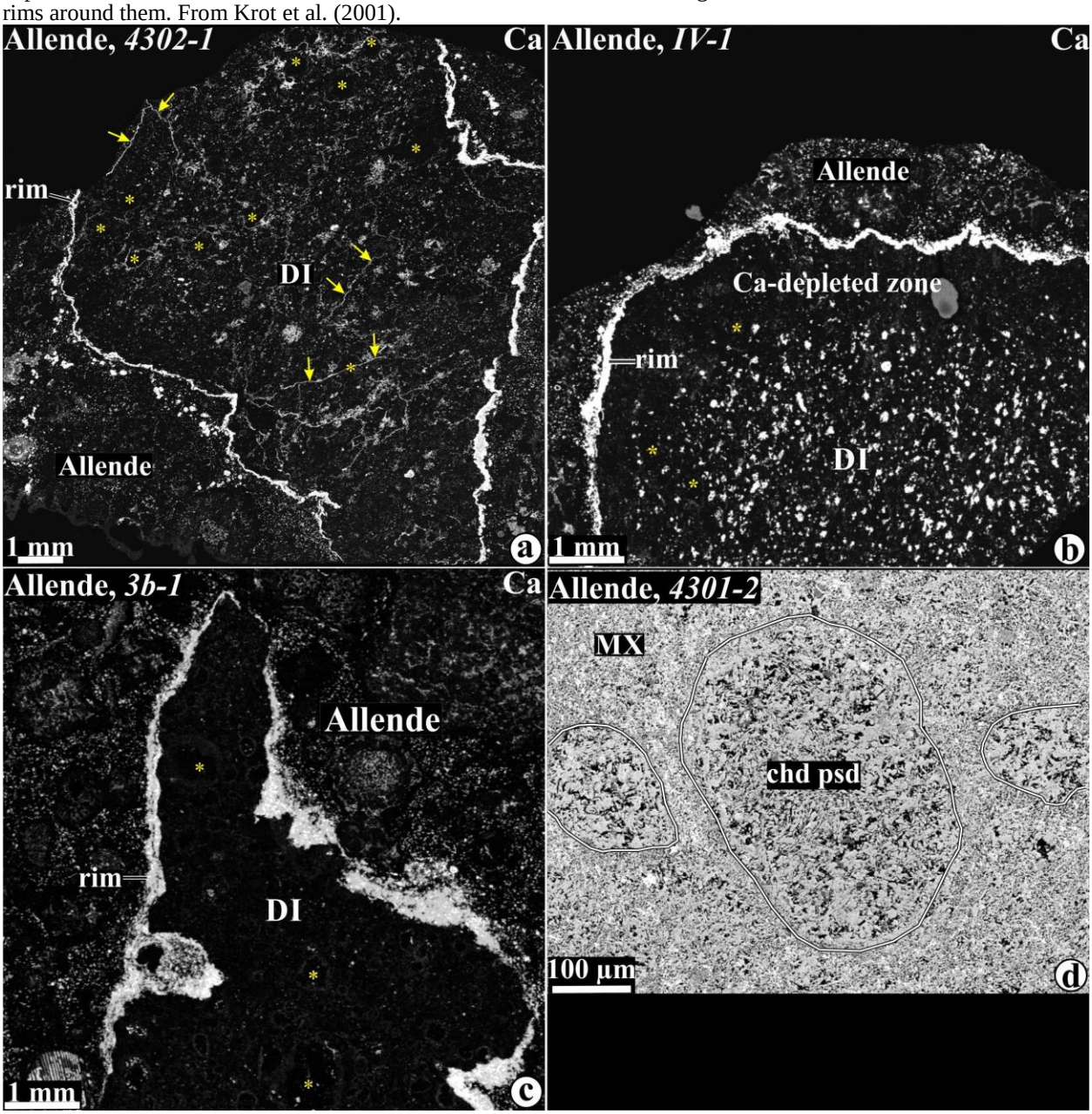

Figure SM21. Oxygen-rich presolar grain abundances for ordinary and carbonaceous chondrites with petrologic types ≥3.00. All errors are 1σ. Data sources: [1] Barosch et al. (2022); [2] Leitner, unpubl.; [3] Floss & Haenecour (2016a); [4] Floss & Haenecour (2016b); [5] Vollmer et al. (2009); [6] Smith et al. (2023); [7] Haenecour et al. (2018); [8] Nguyen et al. (2010); [9] Nittler et al. (2018); [10] Bose et al. (2014); [11] Davidson et al. (2014a).

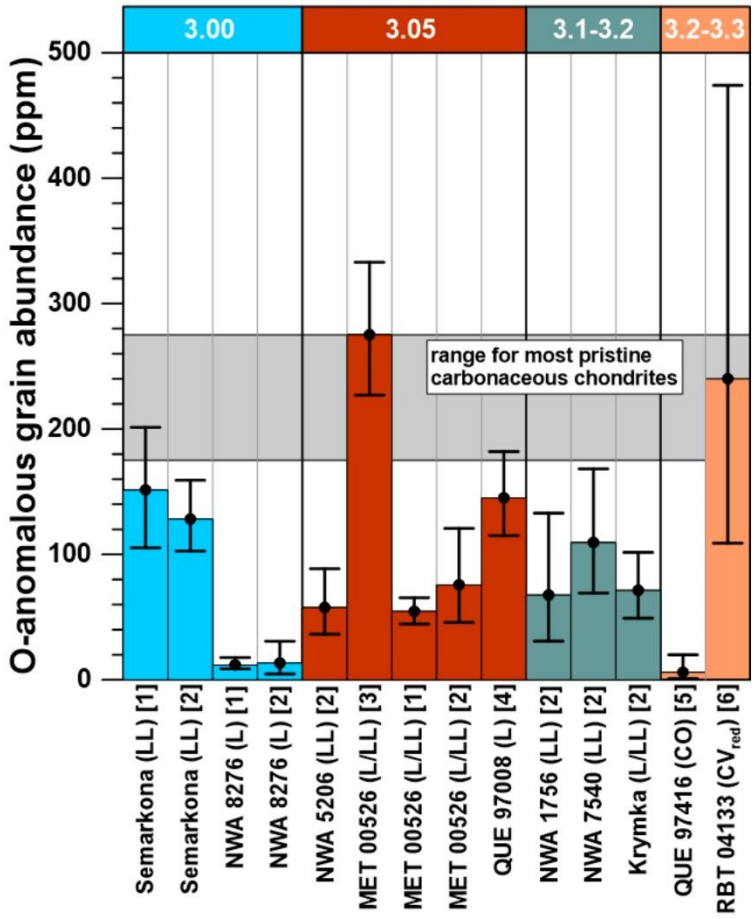

Figure SM22. A modified fragment of water phase diagram from Wikipedia. The labeled stability fields are H_2O vapor (yellow), liquid water (mint green), H_2O ice (sky blue) and H_2O supercritical fluid (pink). The dashed grey lines show a typical range of pressures assumed for the solar nebula. The colored symbols along the vapor condensation curve show measured tensile strengths (Pohl & Britt 2020) of different meteorite types (see legend in the lower right corner). Calculated mantle pressures in different Solar System bodies are shown by the labeled red symbols in the upper left corner for comparison. The dashed blue lines outline approximate fields of 'dry' subcritical and superheated steams and the light blue band along the vapor condensation curve corresponds to *P*-*T* conditions of the 'wet' subcritical steam equilibrated with an aqueous solution.

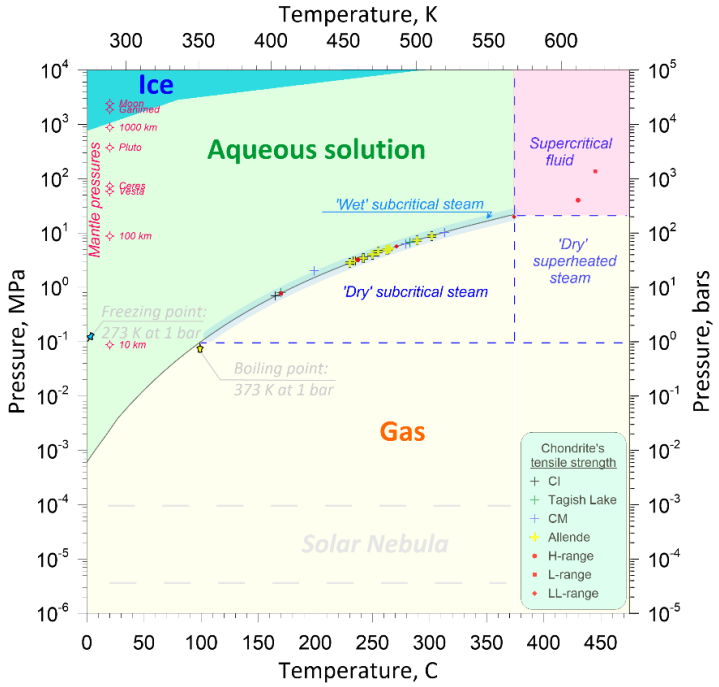

Figure SM23. Maximum solubility of different solutes in the saturated H_2O steam (solid lines) and the aqueous solution formed by its condensation (dash lines). From Krot et al. (2021).

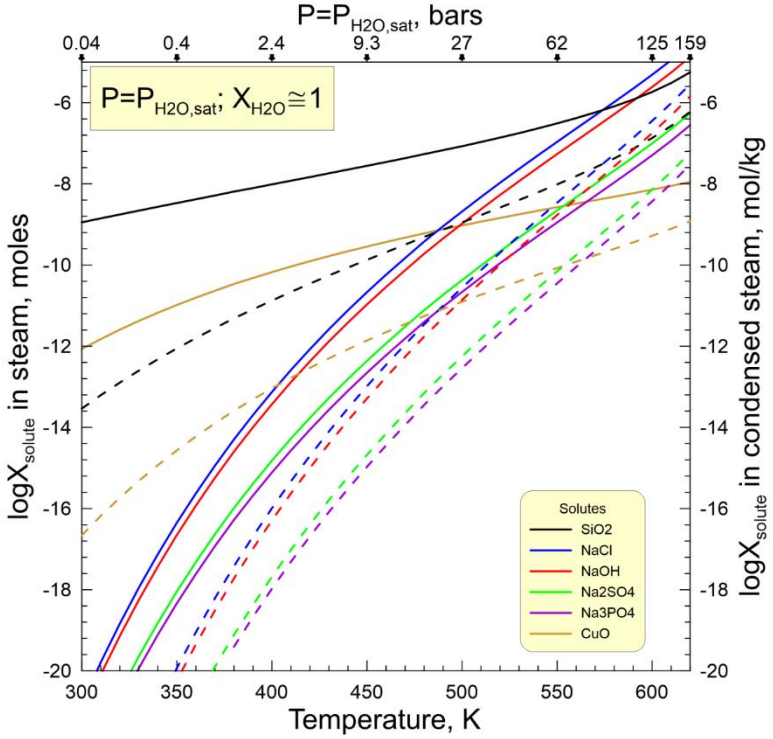

Figure SM24. Phase relations in the water-free Fe-C-O-H system. **A** – $p_{CO_2} = 10^{-7}$ bar, X_{Fe}= 0.95; **B** – $p_{CO_2} = 10^{-7}$ bar, X_{Fe}= 0.5; **C** – $p_{CO_2} = 10^{-1}$ bar, X_{Fe}= 0.95; **D** – $p_{CO_2} = 10^{-1}$ bar, X_{Fe}= 0.5. Dashed lines show metastable equilibria. Fresh and altered metals contain ~5 and 50 at.% Ni, respectively. The topology of the phase diagrams depends upon partial pressure of CO_2 (p_{CO_2}) and the Fe content in metal (X_{Fe}). At $p_{CO_2} < 0.05$ bar the metal-bearing invariant assemblage consists of metal, cohenite, and magnetite (A, B). At $p_{CO_2} > 0.05$ bar fresh metal is in equilibrium with wüstite and Hägg-carbide (C), but the altered metal coexists with Hägg carbide and magnetite (D). Hägg-carbide is metastable relative to elemental carbon and fresh or altered metal at temperatures above ~700 and ~650 K, respectively. Cohenite is metastable at all temperatures.

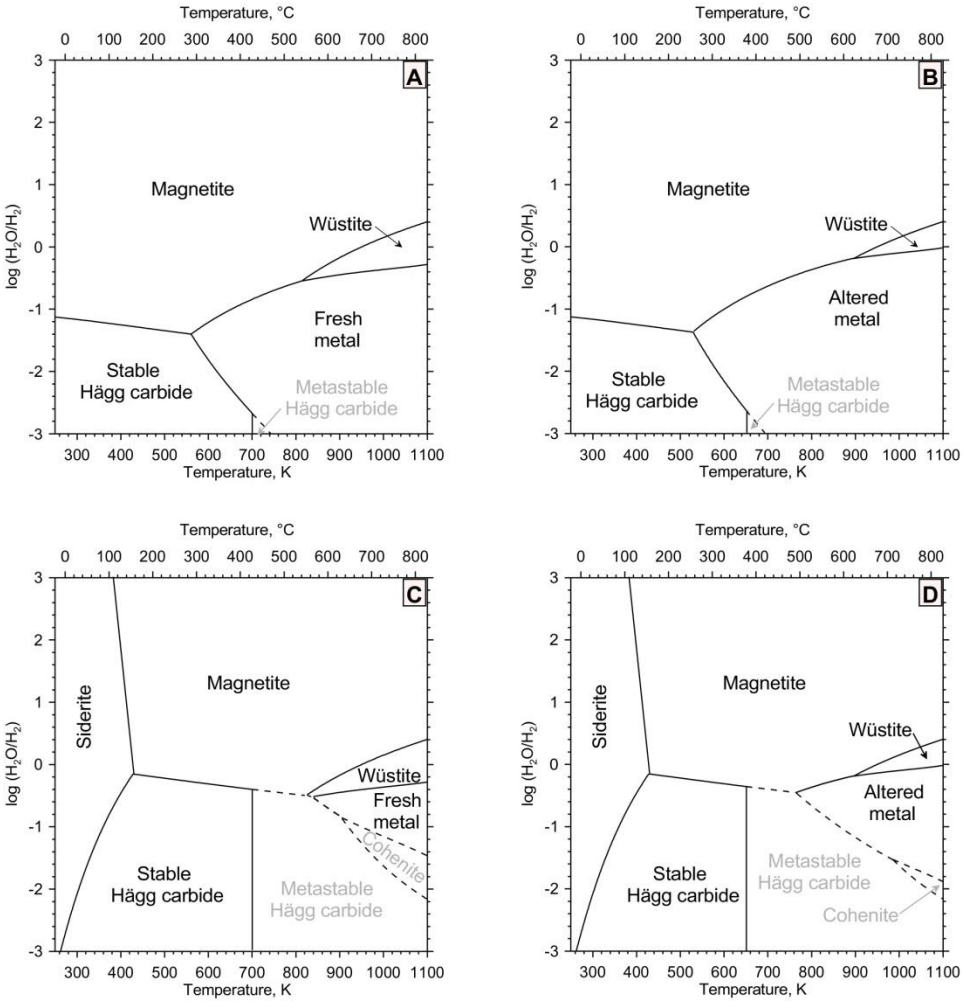

Figure SM25. Phase relations among hedenbergite (Hed), andradite (Andr), fayalite (Fa) and magnetite (Mgt) in the Si-Fe-Ca-O-H system at different temperatures and H_2O/H_2 ratio of the gaseous phase. The activities of SiO_2 ($aSiO_2$) in these diagrams correspond to aqueous solution equilibrated with Kaba ($CV_{oxB}3.1$) matrix at total pressure of 100 bar and different temperatures. Solid circles show compositions of aqueous solutions and gaseous phases equilibrated with the Kaba matrix at corresponding temperatures (Petaev & Mironenko, 1997). Andradite in the upper left fields of all diagrams is the only mineral equilibrated with magnetite and fayalite; magnetite shown in addition to andradite is an excessive phase included to account for the mass-balance of R44. From Krot et al. (1998).

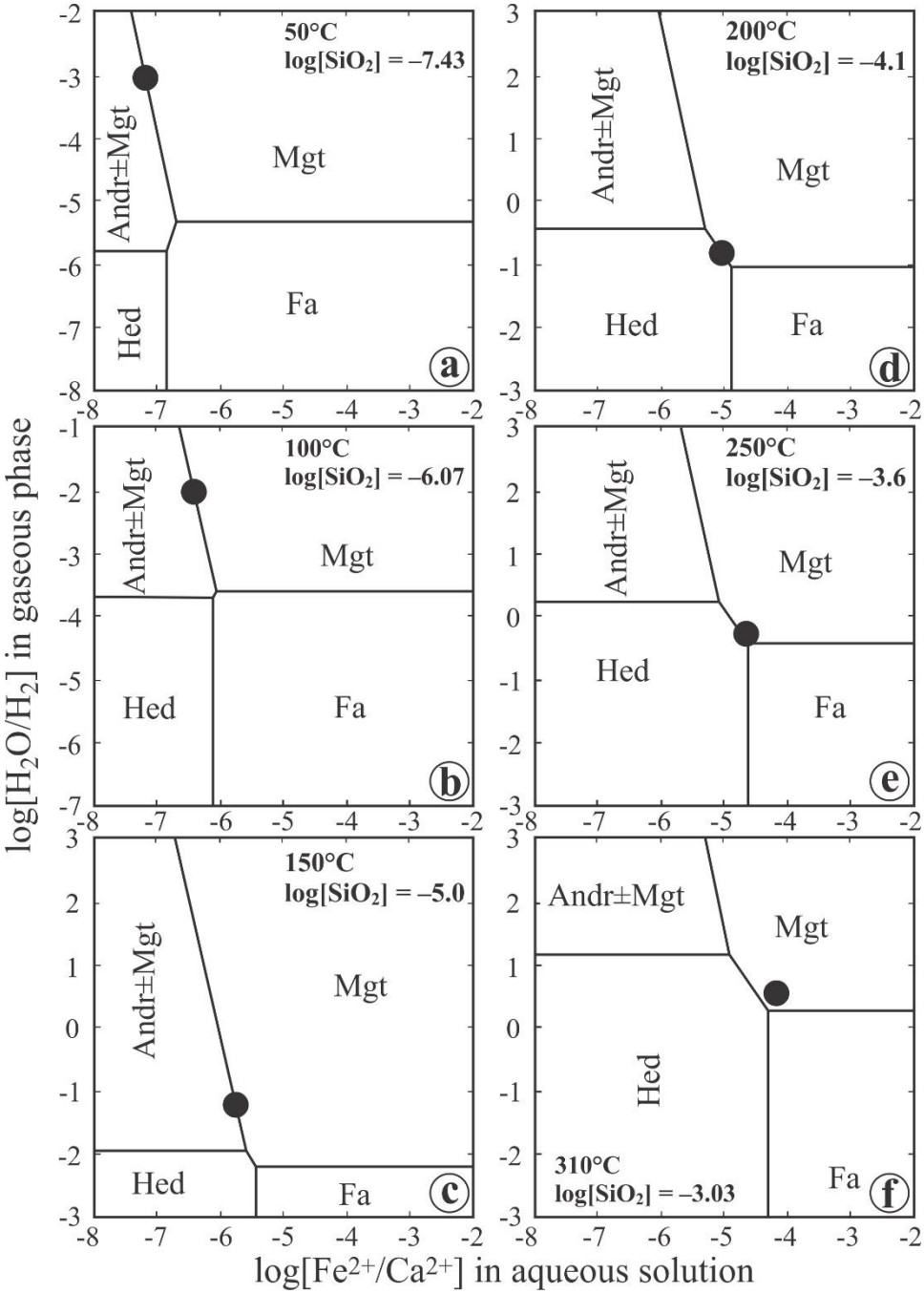

Figure SM26. (upper) The equilibrium mineralogy formed through alteration of the CV_{OxB}-like bulk composition at total pressure (P) of 30 bar above pressure of water saturation as a function of temperature and bulk water/rock (W/R) mass ratio. The dark gray curve shows the boundary between aqueous and metamorphic conditions. The closed light-gray fields show conditions where fayalite is present in equilibrium mineral assemblages. In each field, the fayalite content of ferroan olivine is indicated. Other curves with arrows represent boundaries of stability for some minerals present in the calculated equilibrium assemblage. Minerals are present to the side of the curve where each arrow points. The light gray field shows the coexisting fayalite, troilite, and magnetite. From Jogo et al. (2009). (lower) Composition of olivine in equilibrium with aqueous solution as a function of its temperature and Mg^{2+}/Fe^{2+} ratio.

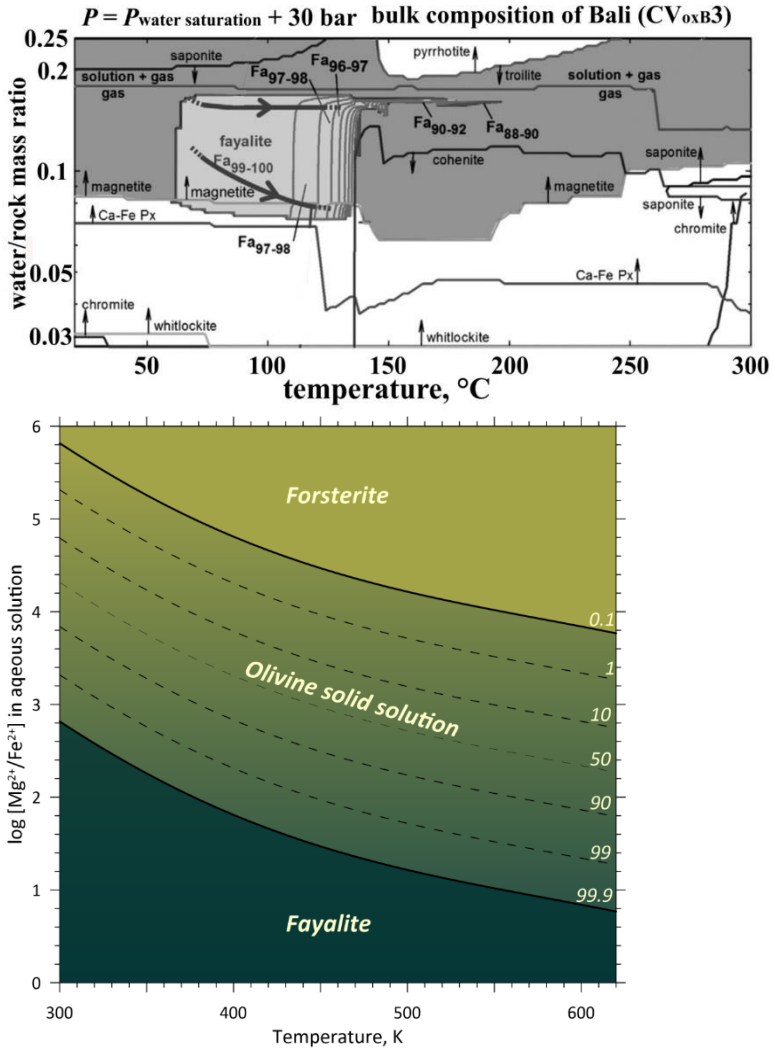

Figure SM27. Phase relations among CaFe-rich minerals in the Fe-Ca-Si-O-H system at (a) 200°C and (b) 250°C. Andr = andradite; Hed = hedenbergite, Mgt = magnetite; Wol = wollastonite; Ol = olivine. Stability fields of olivines in the dark inclusions (Fa_{40}) and the Allende host (Fa_{50}) are shown by solid and dotted lines, respectively. Hedenbergite in the lower middle fields of both diagrams is the only mineral equilibrated with fayalitic olivine; wollastonite shown in addition to hedenbergite is an excessive phase included to account for the observed breakdown of andradite to wollastonite and hedenbergite by reaction R51. Dashed lines show H_2O/H_2 ratios of the gaseous phases equilibrated with the aqueous solutions. At a temperature of ~250°C, olivines from both the DIs and Allende are in equilibrium with andradite, whereas at ~200°C the equilibrium mineral assemblage consists of fayalitic olivine and hedenbergite. From Krot et al. (2000).

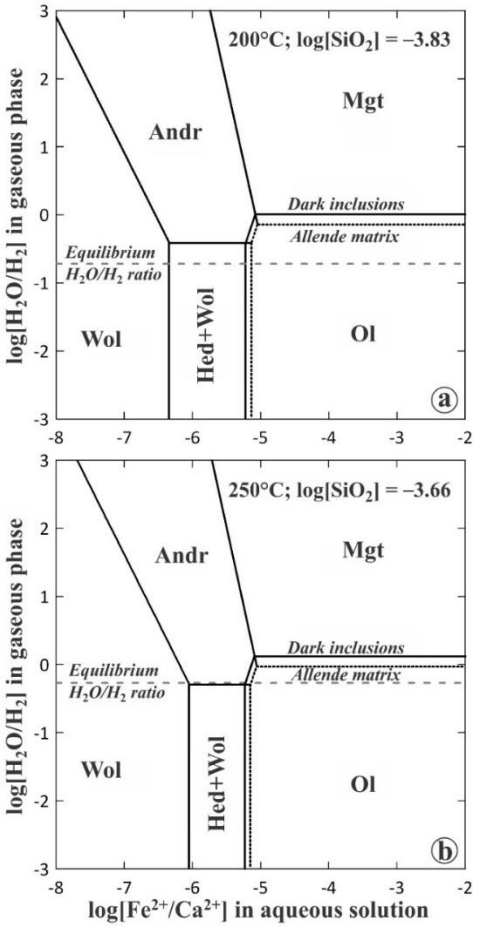

Figure SM28. Temperature stability of CaFe-silicates in the Fe-Ca-Si-O-H system: Andr = andradite, Fa_{50} = Allende matrix olivine, Hed = hedenbergite, Mgt = magnetite, Wol = wollastonite. Thin lines show the phase boundaries of the reaction R51 at different hedenbergite contents in pyroxenes indicated by numbers. Dotted line shows variations of the equilibrium H_2O/H_2 ratios in the gaseous phase. Intersection of the dotted line with the andradite–hedenbergite–wollastonite phase boundary at 242°C defines the lower temperature limit of andradite stability. At temperatures above 277°C, Allende matrix olivine becomes unstable and must be replaced by magnetite if equilibrium among the gaseous phase, aqueous solution and solid phases is maintained. From Krot et al. (2000).

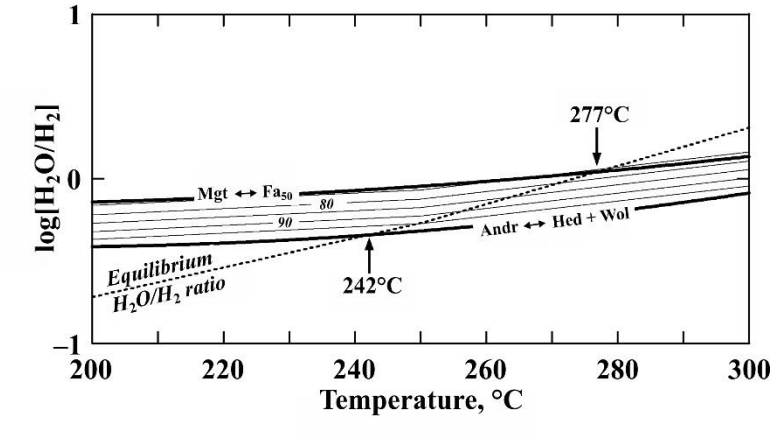

Figure SM29. Replacement reactions of krotite by hercynite and of perovskite by ilmenite, and variations in chemical compositions of secondary spinel-hercynite solid solution (ss), $(\text{forsterite-fayalite})_{ss}$, $(\text{grossular-almandine})_{ss}$, and $(\text{monticellite-kirschsteinite})_{ss}$ as a function of log $[Ca^{2+}/Fe^{2+}]$, log $[Ca^{2+}/Zn^{2+}]$, log $[Ca^{2+}/Fe^{2+}]$ and temperature of aqueous solution.

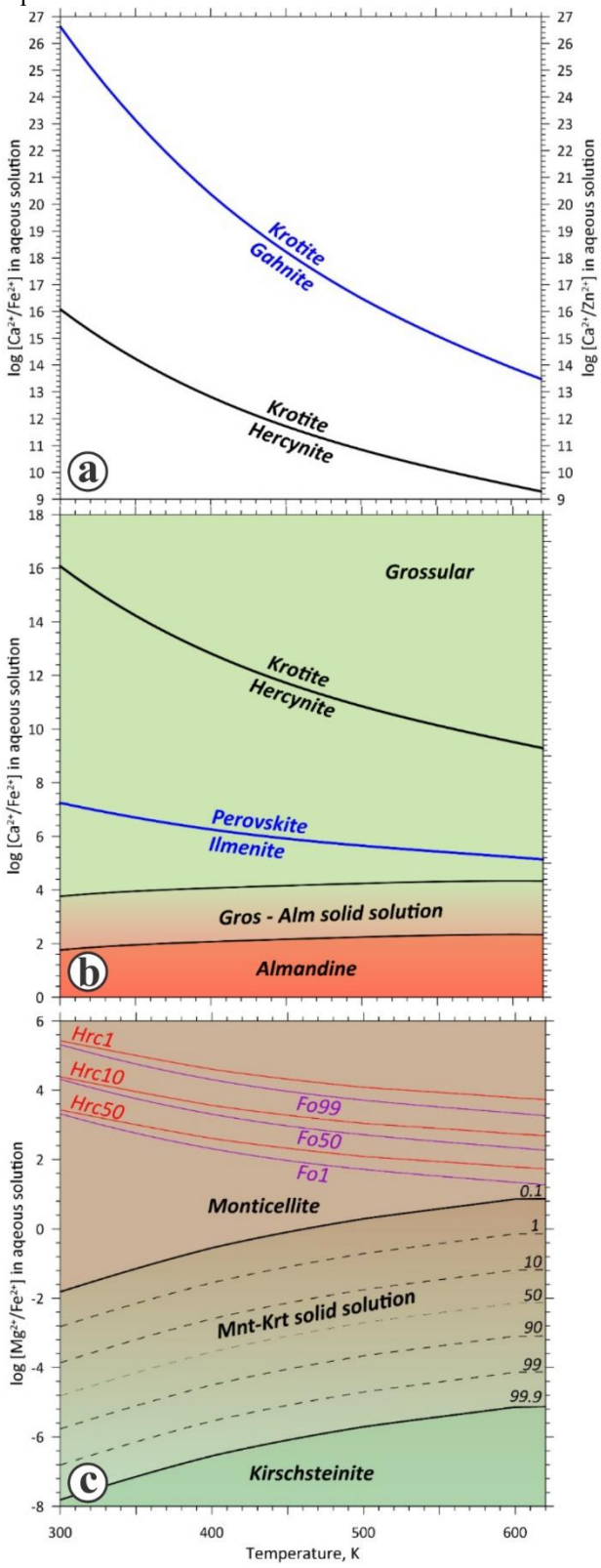

Figure SM30. Phase boundaries of reactions (R21, R25, and R28) involving either (a) gaseous or (b) aqueous silica. The lack of analcime among alteration products places an upper limit on X_{H4SiO4} or X_{SiO2} in steam and aqueous solution, respectively. In the bottom panel, the "condensed steam" field designates an aqueous solution formed by *in situ* condensation of steam as opposed to the "external" aqueous solution, which comes to a CAI from matrix as a liquid. From Krot et al. (2021).

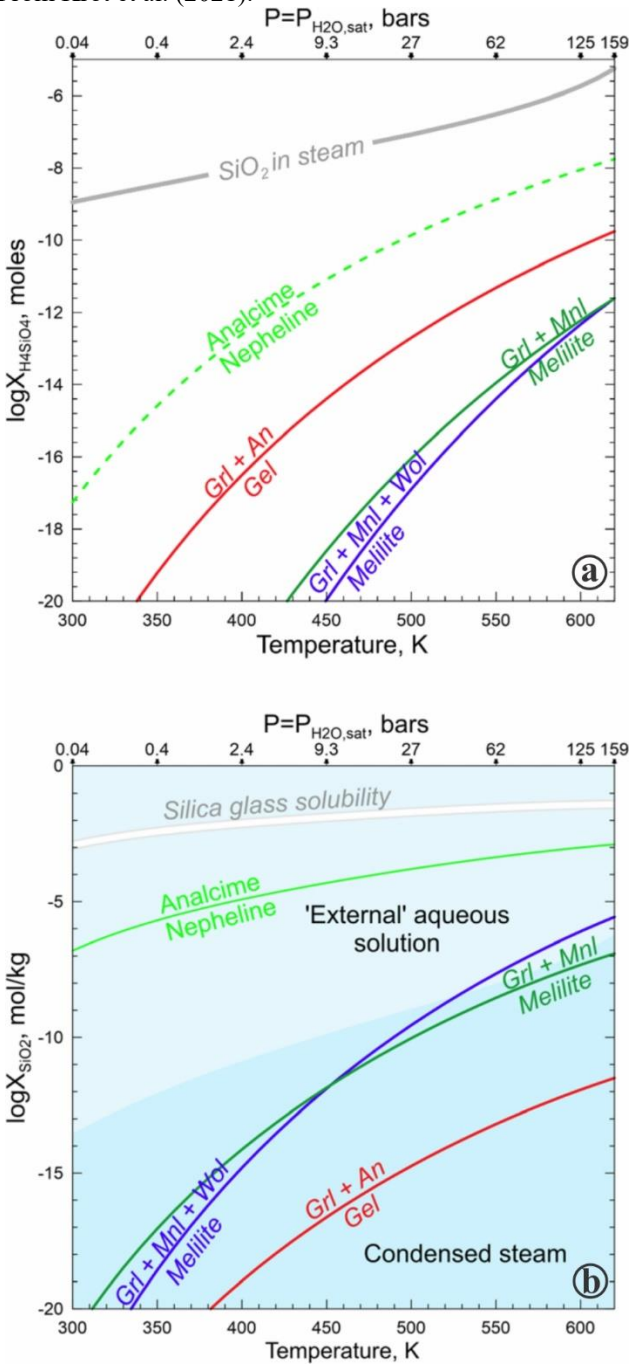

Figure SM31. Calcite – silicate reactions with (a) gaseous H_4SiO_4 or (b) aqueous SiO_2 and Ca^{2+}. The relative stabilities of calcite and wollastonite are greatly dependent on the presence or lack of aqueous solution. If steam does not condense (a), stabilization of calcite requires high amounts of CO_2. At lower CO_2 concentrations in the steam, reactions involving other silicates are metastable (shown by dashed lines) and cannot proceed as written. If steam condenses (b), then even very low (ppm) levels of CO_2 would result in precipitation of calcite from an aqueous solution with rather low Ca^{2+} concentrations of ~10^{-5}÷10^{-4} mol/kg_{H_2O}.

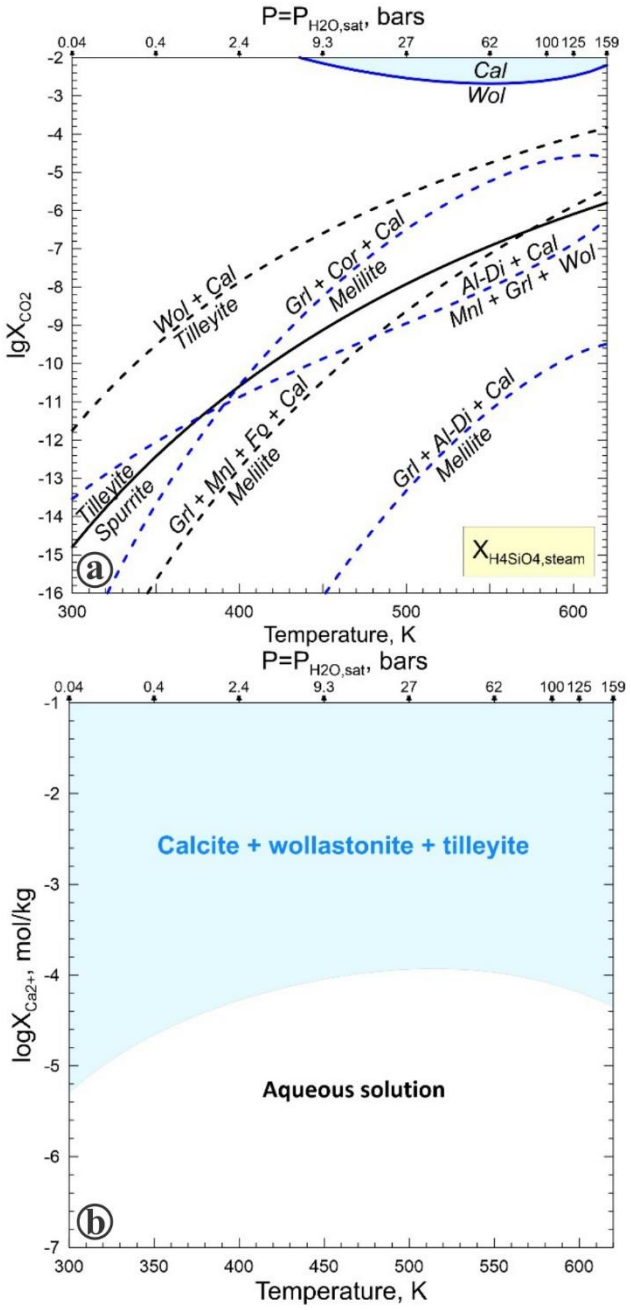

Figure SM32. Phase boundaries of reactions involving addition of either (a,b) aqueous SiO_2 or (c,d) gaseous H_4SiO_4 and removal of Ca in the form of dissolved Ca bicarbonate, $Ca^{2+} + 2HCO_3^-$, at XCO_2 defined by wollastonite−calcite−tilleyite equilibrium (R56) and different values of SiO_2 activity and H_4SiO_4 fugacity defined by reactions R21 and R28. In each plot, the labeled curves of different colors separate the "primary" (above the curves) and "secondary" (below the curves) assemblages which correspond to the reactants and products of each reaction, respectively. The gray calcite saturation line separates two different phase assemblages containing silicates + calcite + aqueous solution above the line and silicates + aqueous solution below it. The tilleyite and spurrite saturation curves show conditions when a mineral starts to crystallize from an aqueous solution according to a reaction $Ca^{2+} + HCO_3^- + SiO_2 \rightarrow xCaO{\cdot}ySiO_2{\cdot}zCO_2 + CO_{2(g)} + H_2O_{(g)}$. From Krot et al. (2021).

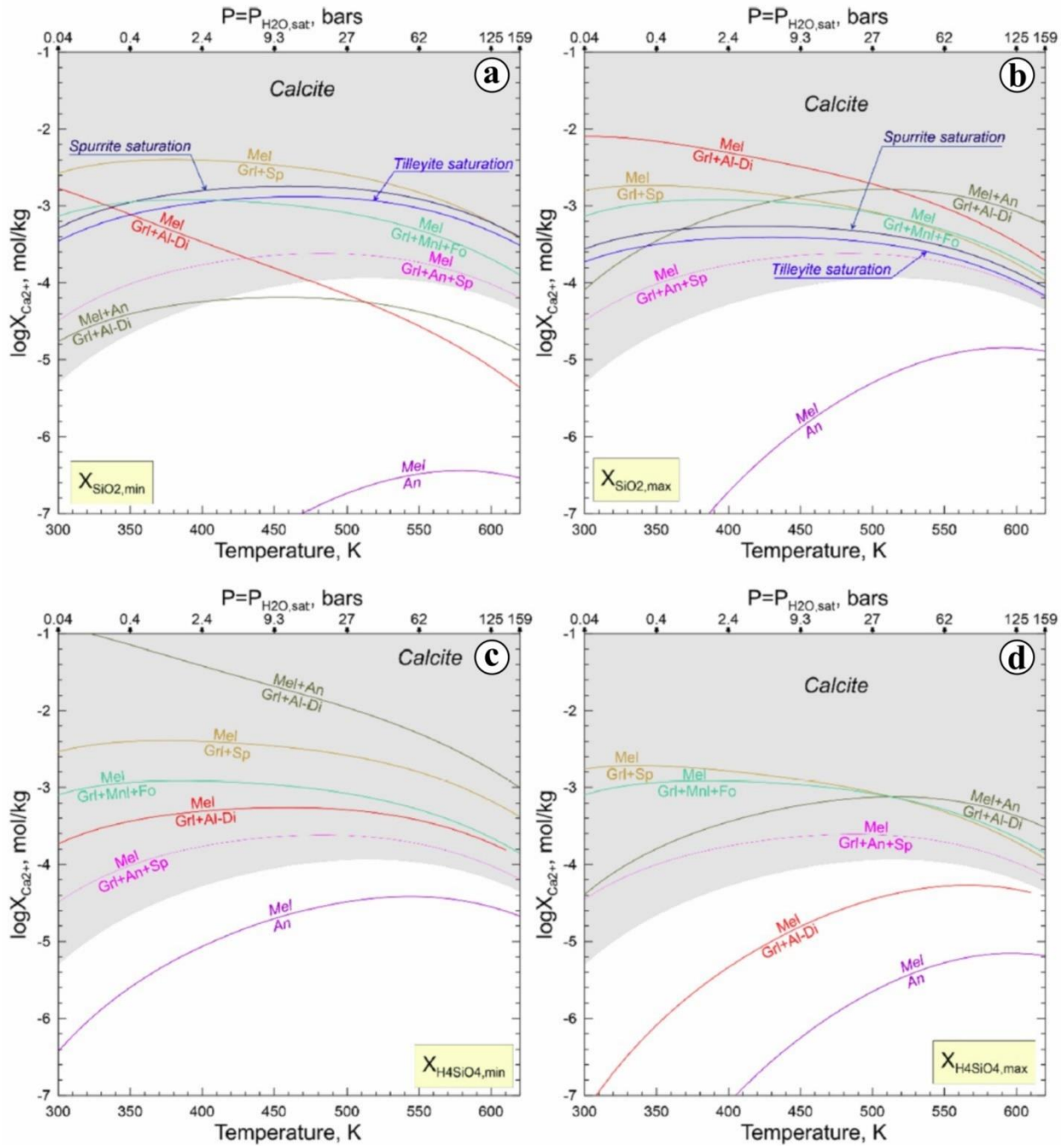

Figure SM33. Phase boundaries of reactions R31 and R32 involving addition of Na^+ and Cl^- and removal of Ca^{2+}. The "condensed steam" field designates an aqueous solution formed by *in situ* condensation of steam as opposed to the "external" aqueous solution, which comes to a CAI from outside (matrix?) as a liquid.

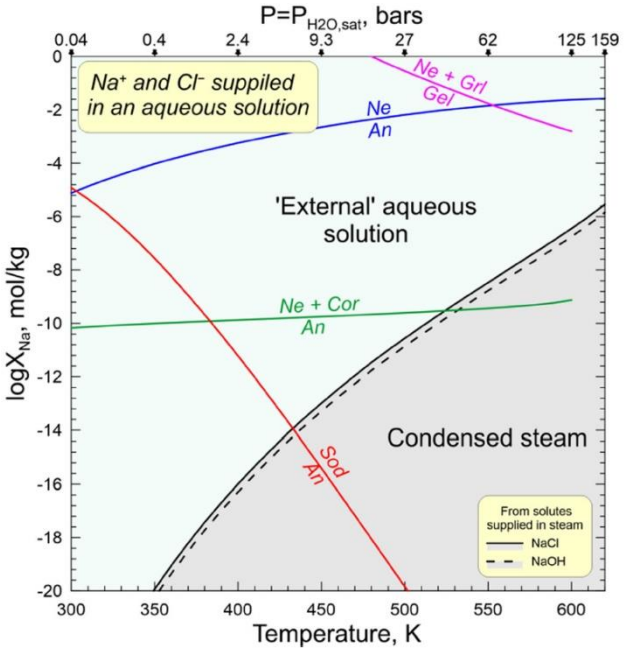

Figure SM34. The inferred initial $^{53}Mn/^{55}Mn$ ratios [$(^{53}Mn/^{55}Mn)_0$] in secondary fayalite and kirschsteinite in CV, CO-like and ordinary chondrites. Data acquired using matrix-matched standards (filled symbols) are very limited (for references, see Table SM6).

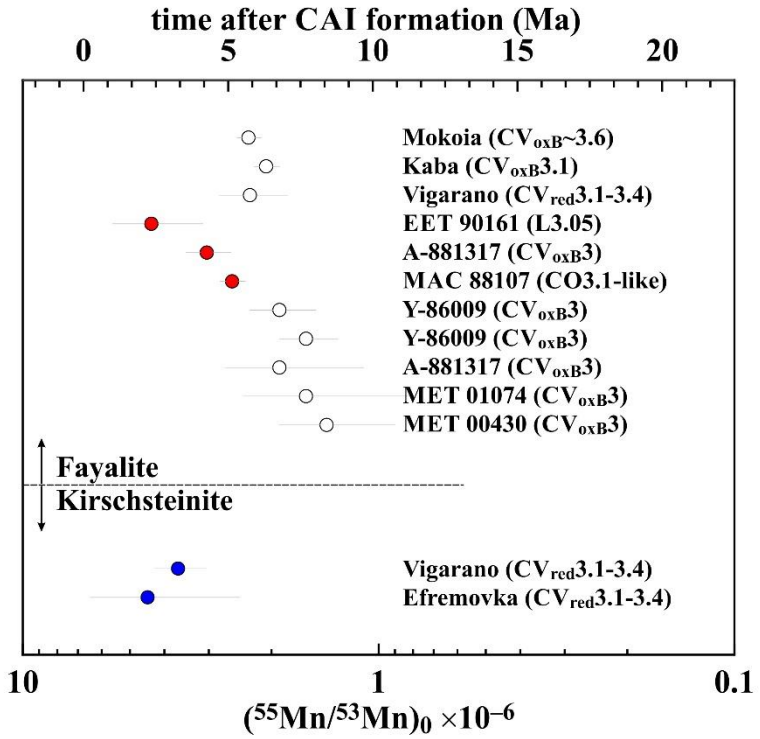

Figure SM35. Mn/Cr relative sensitivity factor in olivine as a function of fayalite contents. From Doyle et al. (2016).

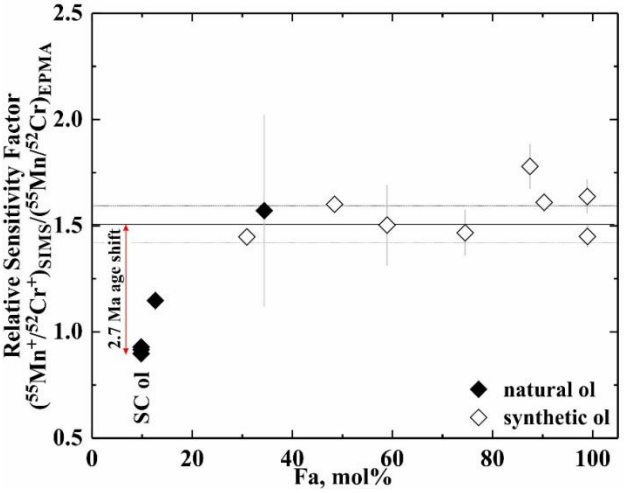

Figure SM36. Mn-Cr evolutionary diagram of kirschsteinite in Vigarano ($CV_{red}3.1$) and fayalite in A-881317 ($CV_{oxB}3.1$). Data from MacPherson et al. (2017).

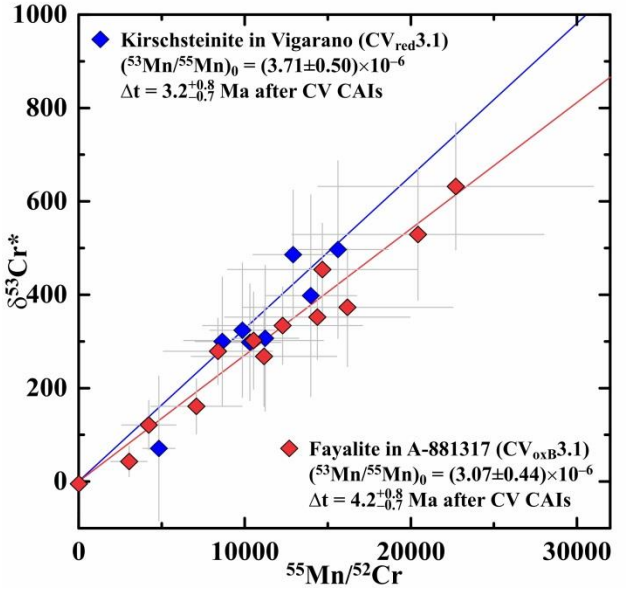

Figure SM37. Al-Mg evolutionary diagram for primary melilite and secondary grossular in several Allende Type B CAIs. Data from a single CAI, *TS-34*, are outlined in the legend. In this CAI, melilite plots along an isochron with a slope of $(5.4\pm0.3)\times10^{-5}$, indistinguishable from the canonical initial $^{26}Al/^{27}Al$ ratio [$(^{26}Al/^{27}Al)_0$] of $(5.25\pm0.02)\times10^{-5}$. Nearly minomineralic grossular replacing gehlenitic melilite shows resolvable excess of ^{26}Mg ($^{26}Mg^*$); data plot along the isochron defined by melilite suggesting that $^{26}Mg^*$ in grossular was inherited from melilite and has no chronological significance. Grossular replacing åkermanitic melilite having very small $^{26}Mg^*$ has high $^{27}Al/^{24}Mg$ ratio and no resolvable $^{26}Mg^*$. This grossular coexists with monticellite and wollastonite having $^{27}Al/^{24}Mg$ ratio of ~ 0. Data from Krot et al. (2010).

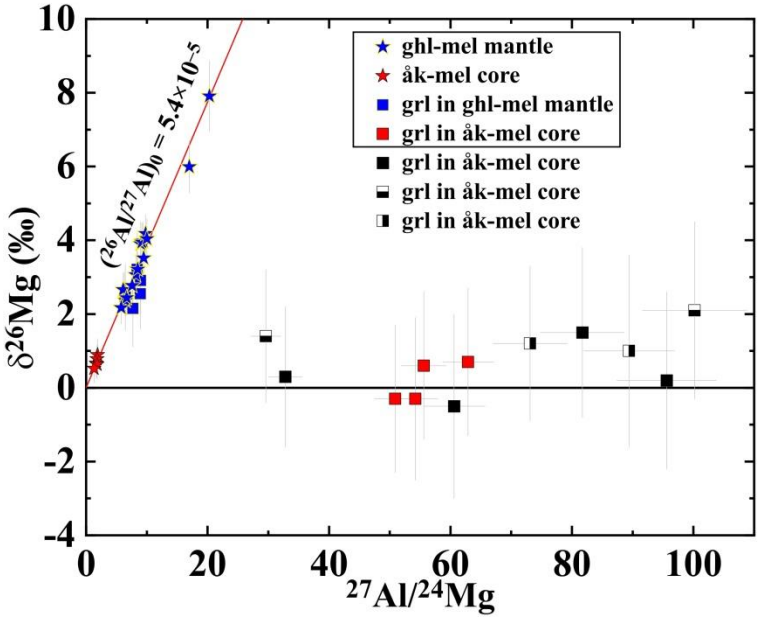

Figure SM38. (a) Combined X-ray map of the Allende Type B CAI *HN3-1b* in Mg (red), Ca (green), and Al (blue). (b, c) BSE and cathodoluminescence images of a region indicated by white rectangle in "a". Two areas analyzed, an#f-1 and an#f-2, in an anorthite grain are outlined. (d–i) $^{23}Na^{+}$ / $^{27}Al^{+}$, $^{27}Al/^{24}Mg$, $\delta^{26}Mg$ isotopographs of the areas an#f-1 and an#f-2. Both regions contain abundant submicron inclusions of an unidentified Mg-rich phase most likely exsolved from anorthite (black dots in "e" and "h"). (j) Al-Mg evolution diagram for anorthite grain calculated from $^{27}Al/^{24}Mg$ and $\delta^{26}Mg^*$ isotopographs. The $\delta^{26}Mg^*$ isotopograph is visually equivalent to the $\Delta^{26}Mg$ isotopograph but is noisier. Each data point represents average and standard deviation in ~3×3 μm^2 area. ^{26}Al-^{26}Mg systematics of anorthite grain is disturbed due to the redistribution of Mg isotopes through Mg-self diffusion during thermal metamorphism. Similar conclusion was reached by (Yurimoto et al. 2000). From Nagashima et al. (2011).

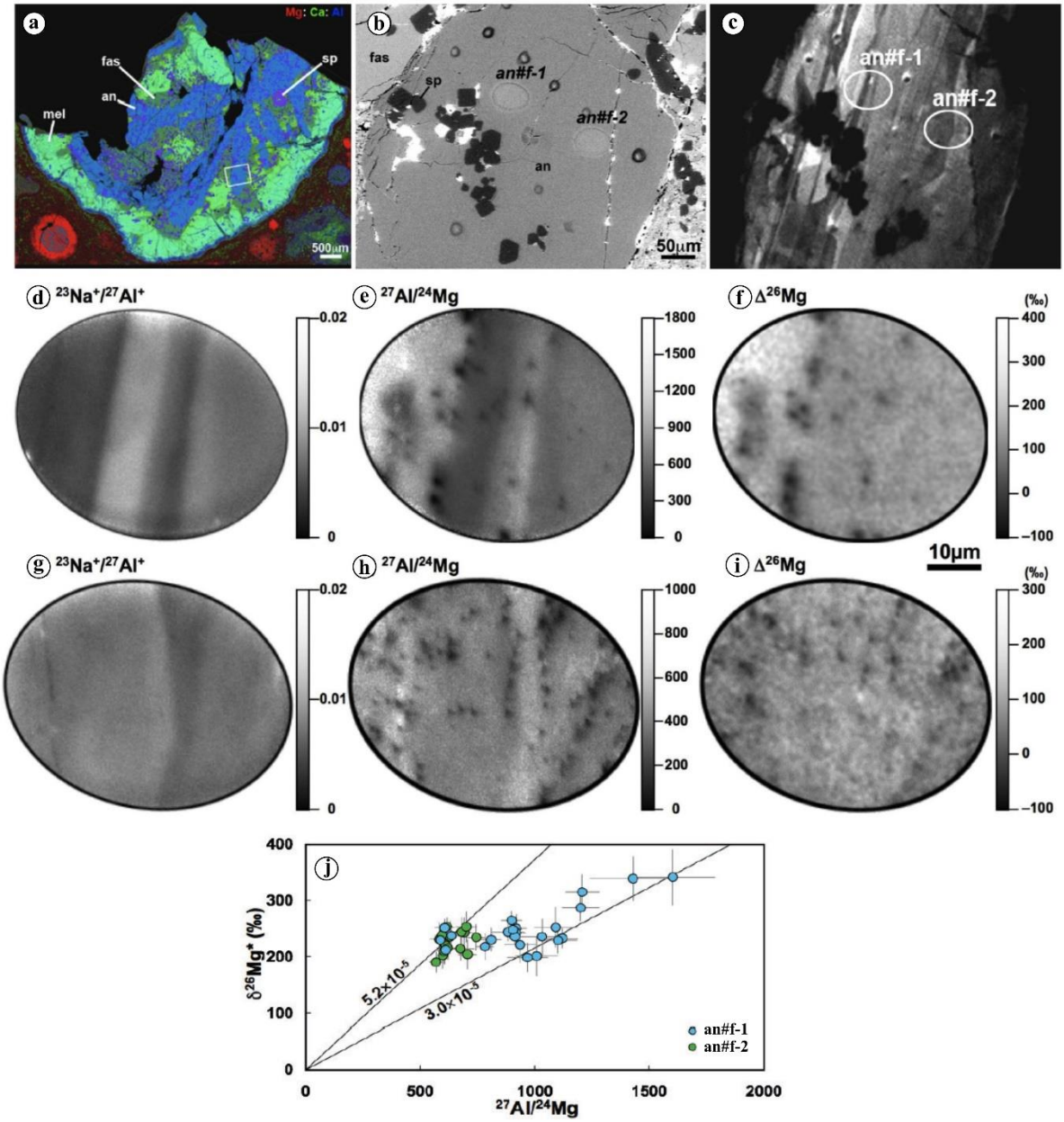

Figure SM39. (a) BSE image of melilite in a CTA CAI from NWA 4964 (CK3.8) and (b, c) Al-Mg evolutionary diagrams of this CAI. The melilite contains abundant submicron inclusions of grossular and possibly other minerals (spinel, hibonite) and is nearly pure gehlenite. Spinel (sp), hibonite (hib), and grossmanite (grs) define an internal isochron with $(^{26}Al/^{27}Al)_0 = (5.09\pm0.58)\times10^{-5}$; melilite shows resolvable excess of ^{26}Mg, but has very high $^{27}Al/^{24}Mg$ ratio and plots along correlation line with $^{26}Al/^{27}Al$ of 1.94 ± 10^{-5}. Data from Krot et al. (2023).

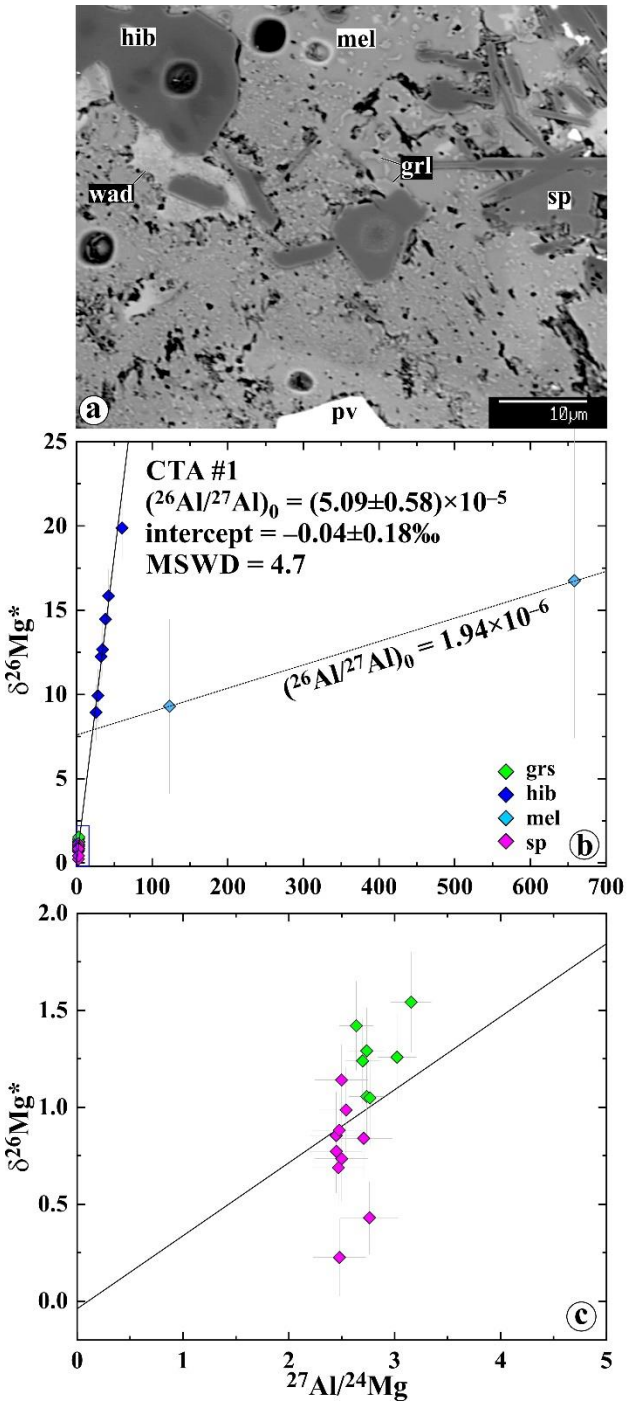

Figure SM40. ^{129}I-^{129}Xe ages of magnetite in CV3, CK3, CO3, CM2, and CI1 chondrites and chondritic components (chondrules, matrix, CAIs, and dark inclusion) separated from several CV3 chondrites. Magnetite separates from CO chondrites are not clean and contain several I-Xe carriers. (for references, see Tables SM7–SM9).

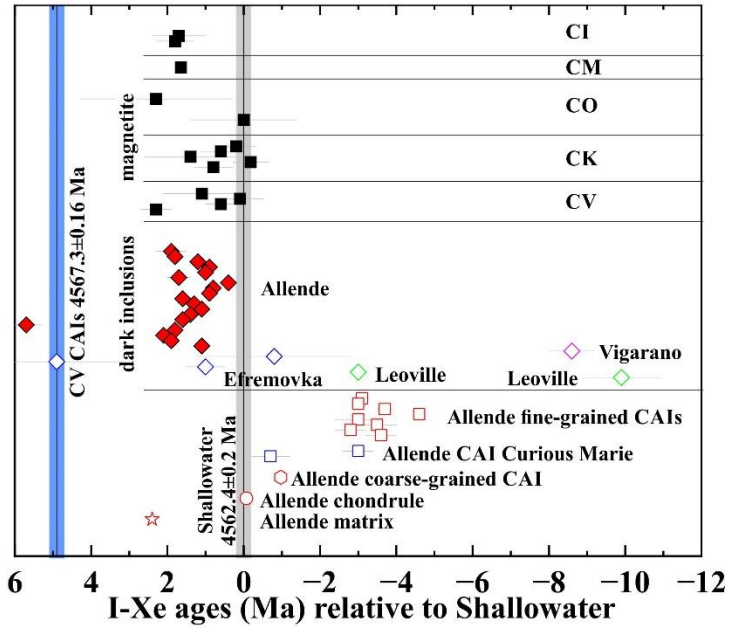

Figure SM41. ^{129}I-^{129}Xe ages of chondrules (red – high-temperature releases; blue – low-temperature releases) from ordinary chondrites. For references see Table SM9.

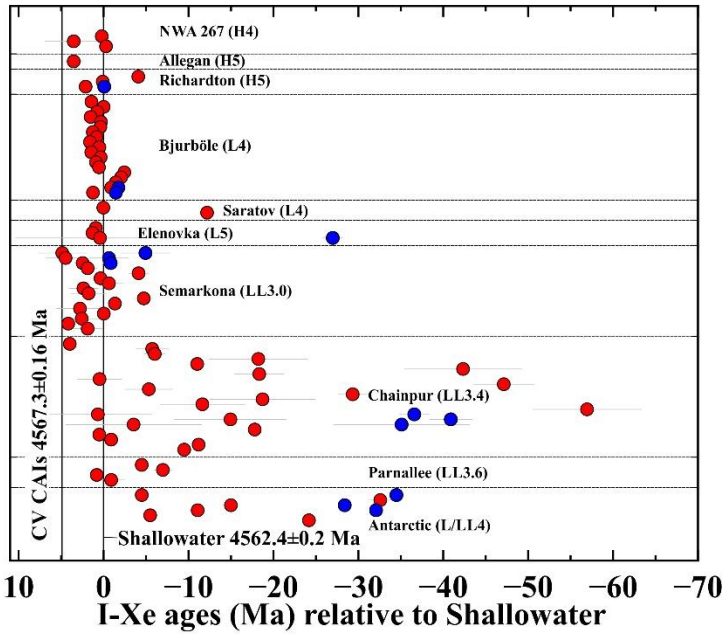

Figure SM42. (a) $\delta^{17}O$ *vs.* $\delta^{18}O$ and (b) $\Delta^{17}O$ of individual phases in chondrules and fine-grained refractory inclusions (spinel-rich CAIs and AOAs) from the C3.00 carbonaceous chondrite Acfer 094. Chondrules and refractory inclusions (data for individual inclusions are separated by dash lines in "b") have internally uniform O-isotope compositions. an = anorthite; avr = average of individual chondrules; cpx = high-Ca pyroxene; fo = forsterite; lpx = low-Ca pyroxene; mel = melilite; ol = FeMg-olivine; sp = spinel. Hereafter: CCAM = carbonaceous chondrite anhydrous mineral line (Clayton et al., 1977); PCM = primitive chondrule mineral line (Ushikubo et al., 2012); TF = terrestrial fractionation line. Data from Ushikubo et al. (2012, 2017).

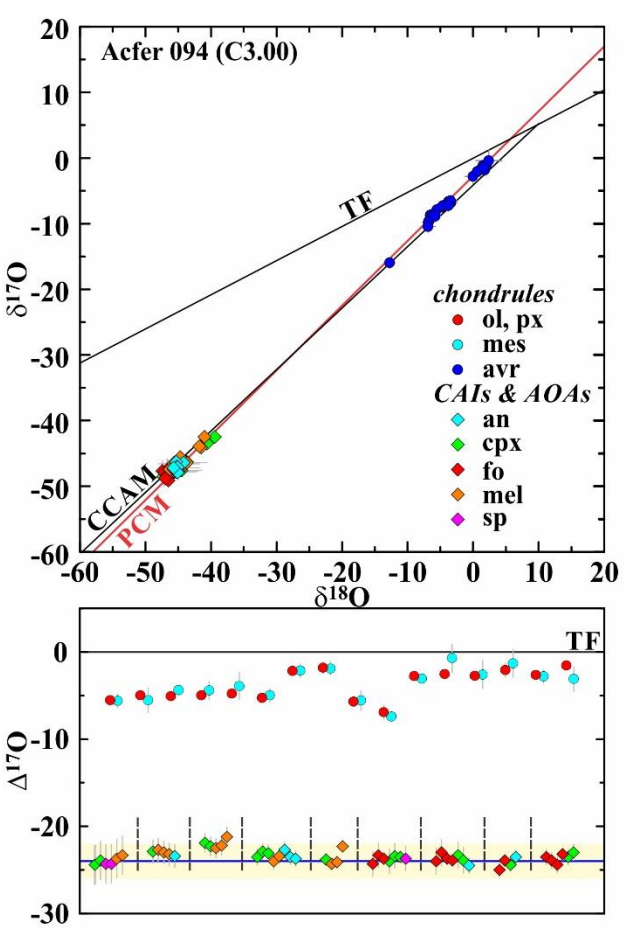

Figure SM43. (a, c, e) $\delta^{17}O$ *vs.* (b, d, f) $\delta^{18}O$ and $\Delta^{17}O$ aqueously formed fayalite and magnetite in unequilibrated ordinary chondrites Semarkona (LL3.00), EET 90161 (L3.05), MET 00452 (L3.05), MET 96503 (L3.1), NEW 3358 (H3.1), Ngawi (L3.0–6 br.), and Vicencia (LL3.2). Fayalite and magnetite plot along mass-dependent fractionation lines with $\Delta^{17}O$ of ~ 4.0–4.8‰ which correspond to $\Delta^{17}O$ of aqueous fluid on the H, L, and LL parent bodies. There are no resolvable differences in $\Delta^{17}O$ of the fluids in different UOCs. Data from Doyle et al. (2015), Keil et al. (2015), Ebert et al. (2020), and Krot et al. (2022a).

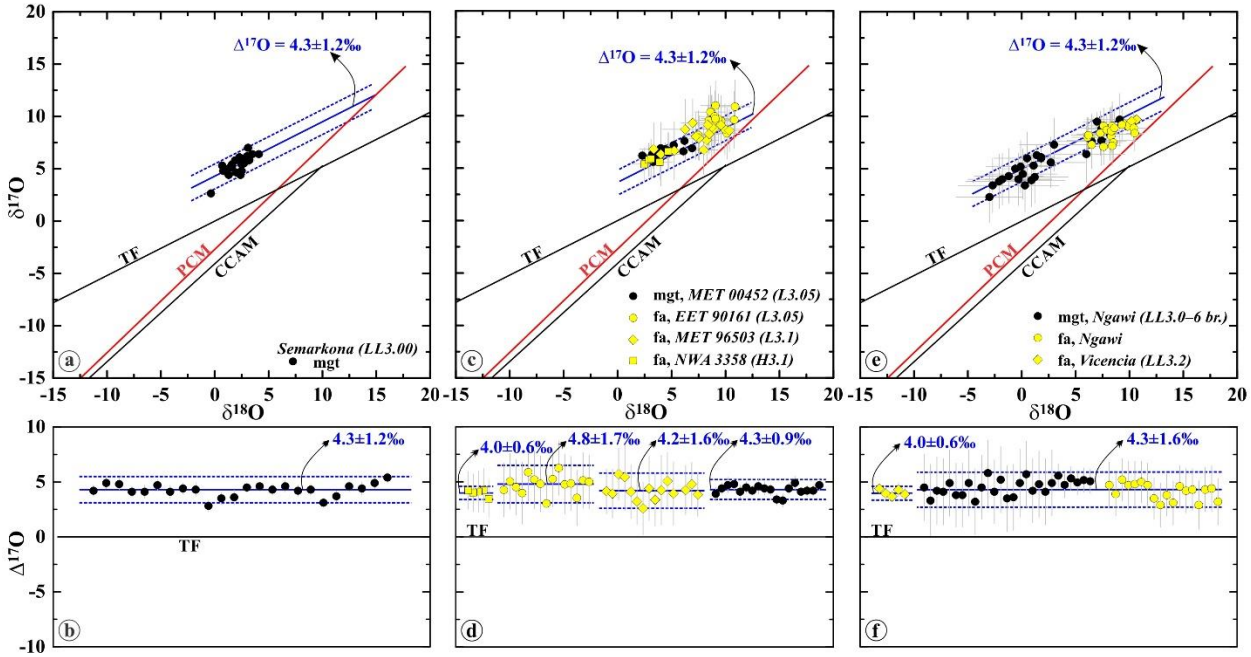

Figure SM44. (a, c, e) $\delta^{17}O$ *vs.* $\delta^{18}O$ and (b, d, f) ^{17}O of aqueously formed fayalite and magnetite in Y-81020 (CO3.05), EET 90043 (CO3.1), and MAC 88107 (CO3.1-like) carbonaceous chondrites. Fayalite and magnetite plot along mass-dependent fractionation lines with $\Delta^{17}O$ of ~ –0.2‰, –0.3‰ and –1.8‰, respectively, which correspond to $\Delta^{17}O$ of aqueous fluid on their parent bodies. Data from Doyle et al. (2015) and Krot et al. (2022a).

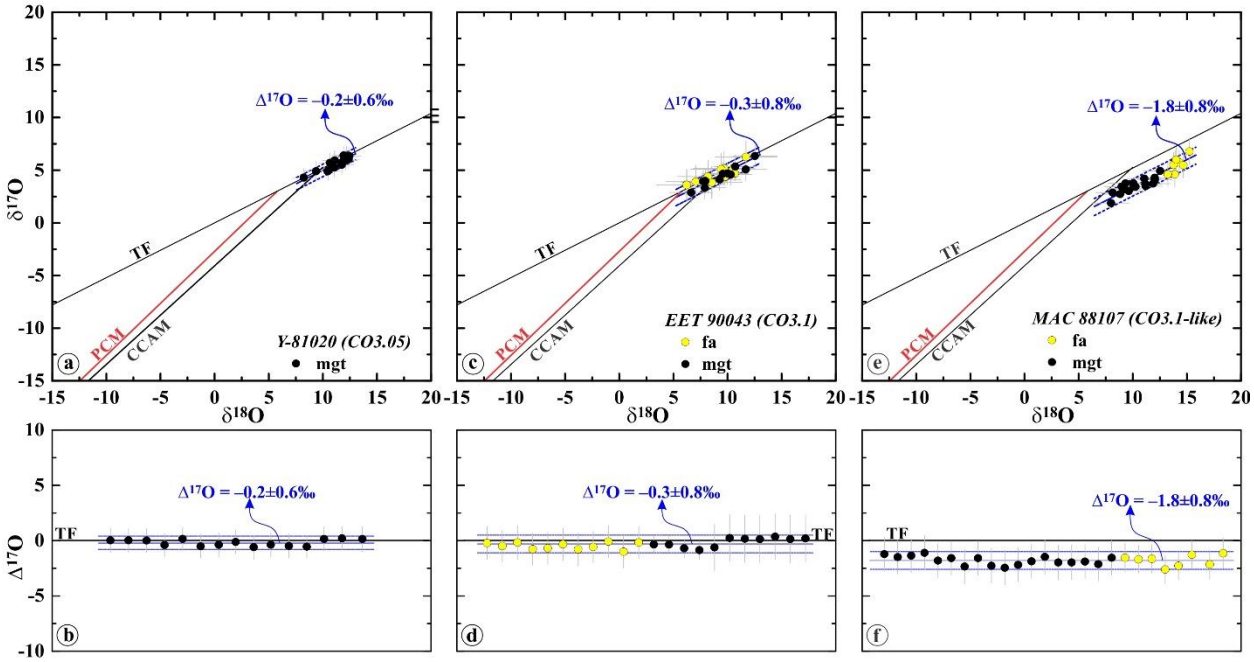

Figure SM45. (a, c) $\delta^{17}O$ *vs.* $\delta^{18}O$ and (b, d) $\Delta^{17}O$ of aqueously formed fayalite and magnetite in (a, b) weakly-metamorphosed CV chondrites: Kaba ($CV_{oxB}3.1$), Mokoia ($CV_{ox}B3.1$), and A-881317 ($CV_{oxB}3.2$), and (c, d) more metamorphosed CK and CV chondrites: Allende (CV3.6), Dar al Gani 431 (CK3), NWA 4964 (CK3.8), Watson 002 (CK3), and Ningqiang (CK3an) chondrites. In weakly-metamorphosed CVs, both fayalite and magnetite show a range of $\Delta^{17}O$ values suggesting these minerals recorded evolution of O-isotope composition of aqueous fluid (as indicated by green arrows). Data from [1] Marrocchi et al. (2016, 2018); [2] Doyle et al. (2015) and Krot et al. (2022a). In metamorphosed CKs, magnetite has a limited range of $\Delta^{17}O$, possibly, reflecting isotope equilibration with matrix silicates during thermal metamorphism. Data from Choi et al. (1997), Choi & Wasson (2003), and Davidson et al. (2014b).

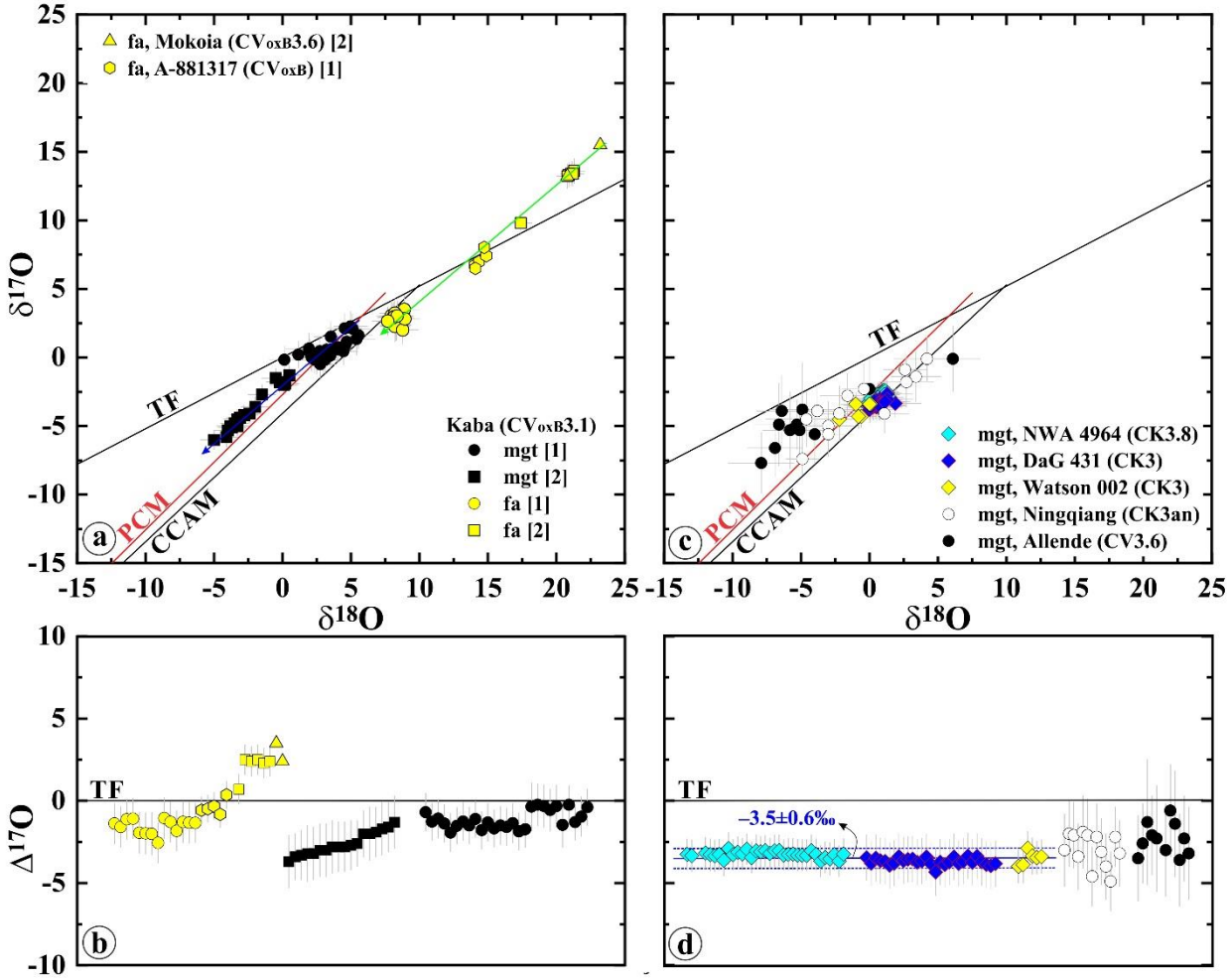

Figure SM46. $\delta^{17}O$ *vs.* $\delta^{18}O$ of secondary minerals in coarse-grained igneous CAIs from Allende (CV3.6), NWA 4964 (CK3.8), and NWA 5343 (CK3.7) carbonaceous chondrites. Secondary minerals plot along mass-dependent fractionations lines with a similar $\Delta^{17}O$ value of ~ –3.5‰ that corresponds to $\Delta^{17}O$ of metasomatic fluids in these meteorites. Data from Krot et al. (2022b, 2023).

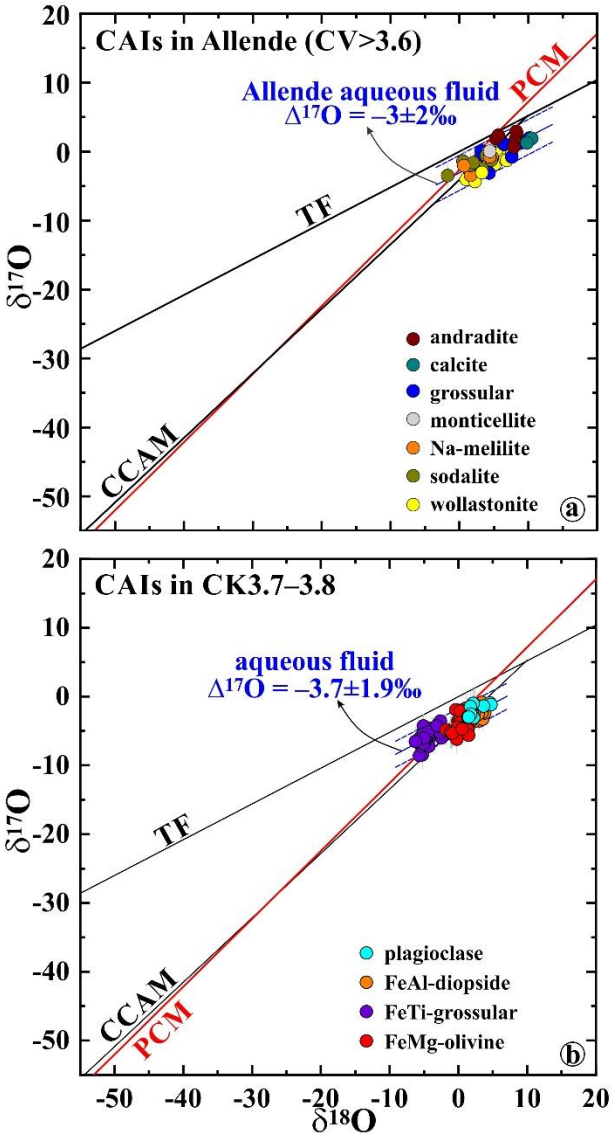

Figure SM47. (a) $\delta^{17}O$ *vs.* $\delta^{18}O$ and (b) $\Delta^{17}O$ of individual minerals in refractory inclusions from Semarkona (LL3.00) and NWA 3358 (H3.1). Fine-grained CAI and AOAs from Semarkona (LL3.00) have homogenous O-isotope compositions ($\Delta^{17}O$ ~ –23±2‰) (most analyses are mixed phases). Most CAIs and AOAs from NWA 3358 have heterogeneous O-isotope compositions with hibonite, spinel, Al,Ti-diopside, and forsterite being ^{16}O-enriched ($\Delta^{17}O$ ~ –24±2‰) compared to melilite and anorthite ($\Delta^{17}O$ range from ~ –25 to ~ –7±2‰). The most ^{16}O-depleted analyses of anorthite overlap with $\Delta^{17}O$ of aqueous fluid on the H chondrite parent body (as inferred from $\Delta^{17}O$ of aqueously formed fayalite in NWA 3358, see Fig. 6 in Ebert et al. 2020) suggesting isotope exchange with the fluid. an = anorthite; cpx = Al±Ti-diopside; fo = forsterite; hib = hibonite; mel = melilite; pv = perovskite; sp = spinel. Data from McKeegan et al. (1998), Itoh et al. (2007), and Ebert et al. (2020).

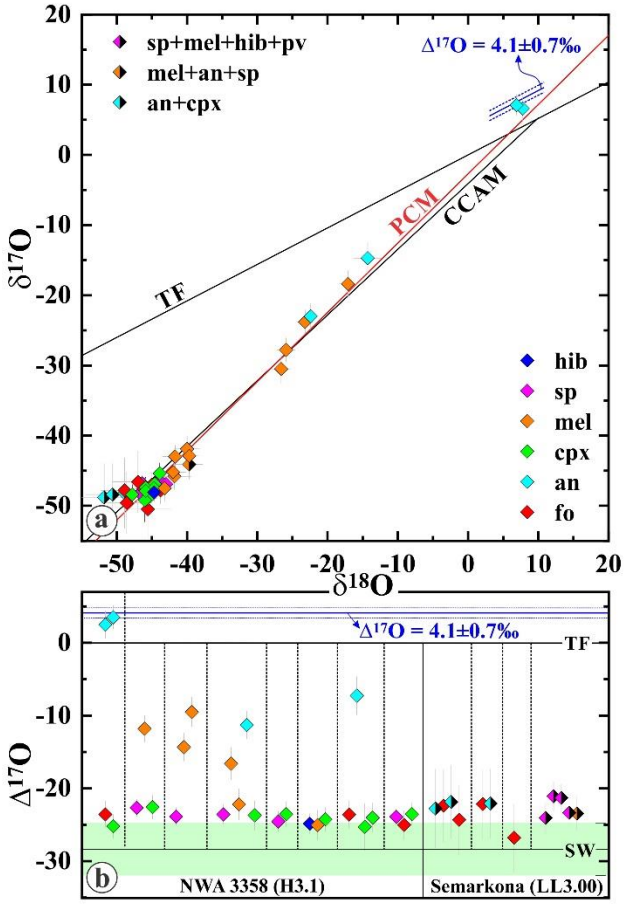

Figure SM48. (a) $\delta^{17}O$ *vs.* $\delta^{18}O$ and (b) $\Delta^{17}O$ of individual minerals in grossite-bearing CAIs and their Wark-Lovering (WL) rims from CO3 chondrites of different petrologic subtypes. CAIs in CO3.0 chondrites have uniform solar-like O-isotope compositions, whereas those in CO chondrites of higher petrologic subtype are isotopically heterogeneous: grossite, krotite, and melilite are ^{16}O-depleted compared to hibonite and Al-diopside. The most ^{16}O-depleted minerals overlap with O-isotope composition of aqueous fluid in CO3 chondrites that is inferred from compositions of aqueously-formed fayalite, magnetite, and Zr-bearing hercynite. cor = corundum; cpx = Al,Ti-diopside; fa = fayalite; fo = forsterite; grs = grossite; hib = hibonite; krt = krotite; mel = melilite; mgt = magnetite; pv = perovskite; lpx = low-Ca pyroxene; sp = spinel; SW = solar wind (McKeegan et al., 2011); zr-hrc = Zn-hercynite. Mineral formulae are listed in Table 1. Data from Krot et al. (2019a).

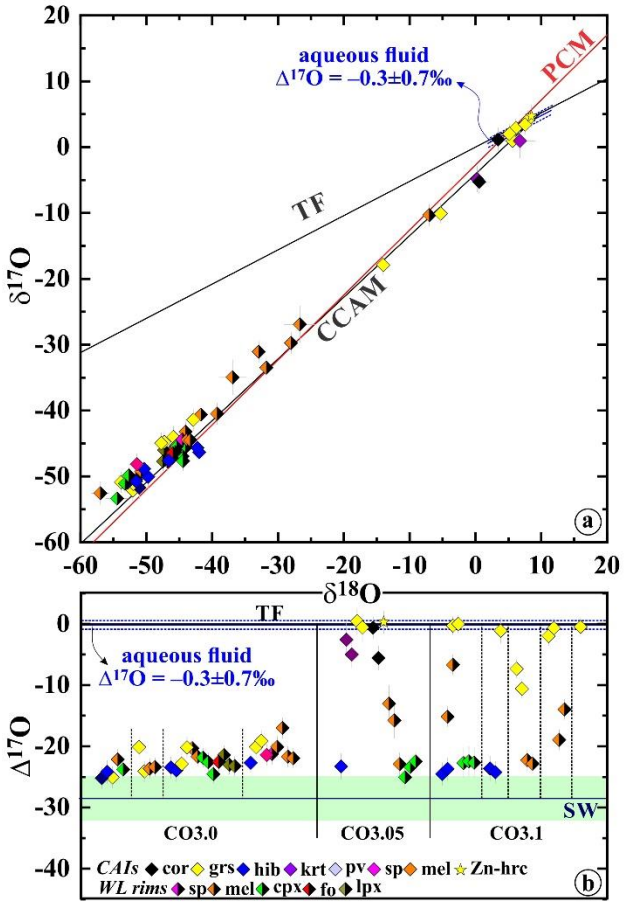

Figure SM49. $\Delta^{17}O$ values of individual minerals in ultrarefractory CAIs from (a) CM, CR, and CH3.0 chondrites, (b) CO3 chondrites, and (c) CV3 chondrites. Most CAIs in chondrites of petrologic types ≤3.0 have uniform $\Delta^{17}O$, whereas most CAIs in chondrites of higher petrologic subtypes are isotopically heterogeneous: Zr-, and Sc-bearing minerals (davisite, kangite, panguite, tazheranite, warkite), melilite, and perovskite are ^{16}O-depleted compared to Al,Ti-diopside, corundum, forsterite, hibonite, and spinel. cor = corundum; Al,Ti-di = Al,Ti-diopside; cor = corundum; dav = davisite; er = eringaite; fo = forsterite; grs = grossite; hib = hibonite; kng = kangite; lpx = low-Ca pyroxene; mch = machiite; mel = melilite; png = panguite; pv = perovskite; qz = quartz; sp = spinel; tzr = tazheranite; wrk = warkite. Mineral formulae are listed in Table 1. Data from Krot et al. (2019b).

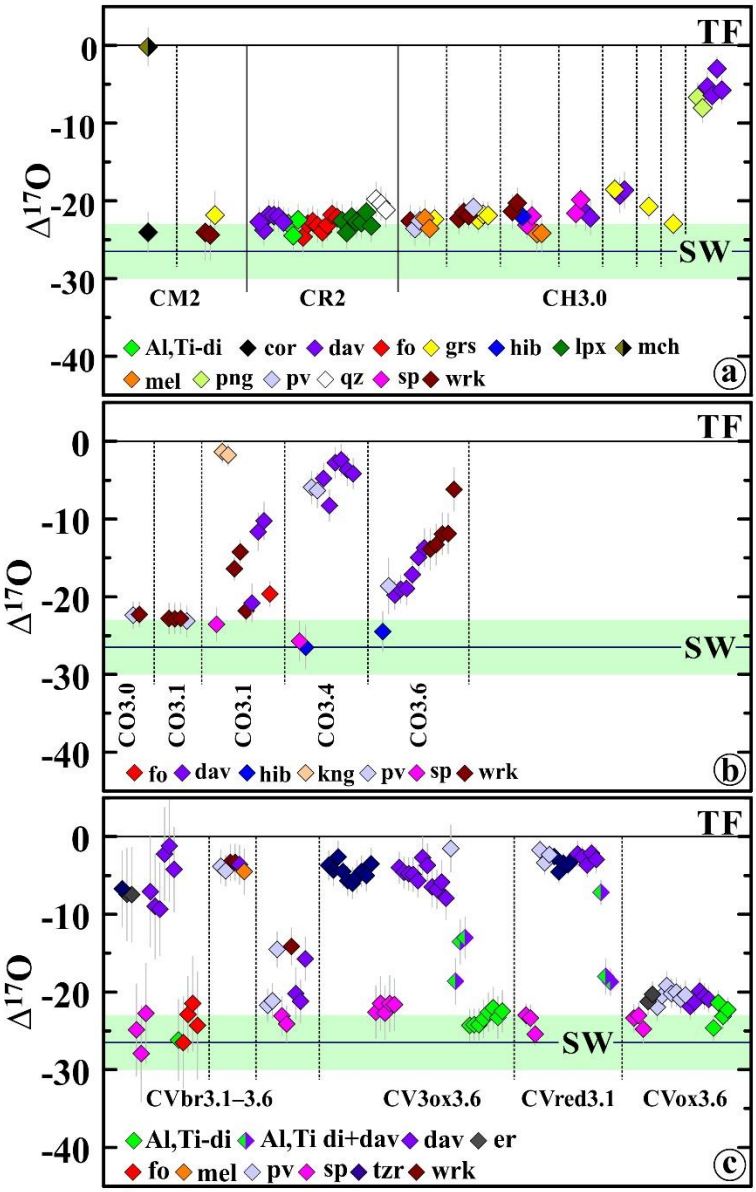

Figure SM50. $\delta^{17}O$ *vs.* $\delta^{18}O$ of primary minerals in coarse-grained igneous CAIs (CTA, B, and FoB) from Allende (CV3.6), NWA 4964 (CK3.8), and NWA 5343 (CK3.7). Forsterite, hibonite, low-Ti Al-diopside, and rhönite have solar-like ^{16}O-rich compositions. Melilite, anorthite, and high-Ti pyroxenes (fassaite and grossmanite) are ^{16}O-depleted to various degrees. The most ^{16}O-depleted compositions overlap with the inferred compositions of aqueous fluids in these meteorites which are inferred from O-isotope compositions of secondary minerals in these CAIs (see Fig. SM46a) suggesting poscrystallization O-isotope with the fluid. Inclusions of melilite and high-Ti pyroxenes in spinel and perovskite often preserved ^{16}O-rich compositions. Data for the Allende CAI TS-34 are from Kawasaki et al. (2018); other data are from Krot et al. (2022b, 2023).

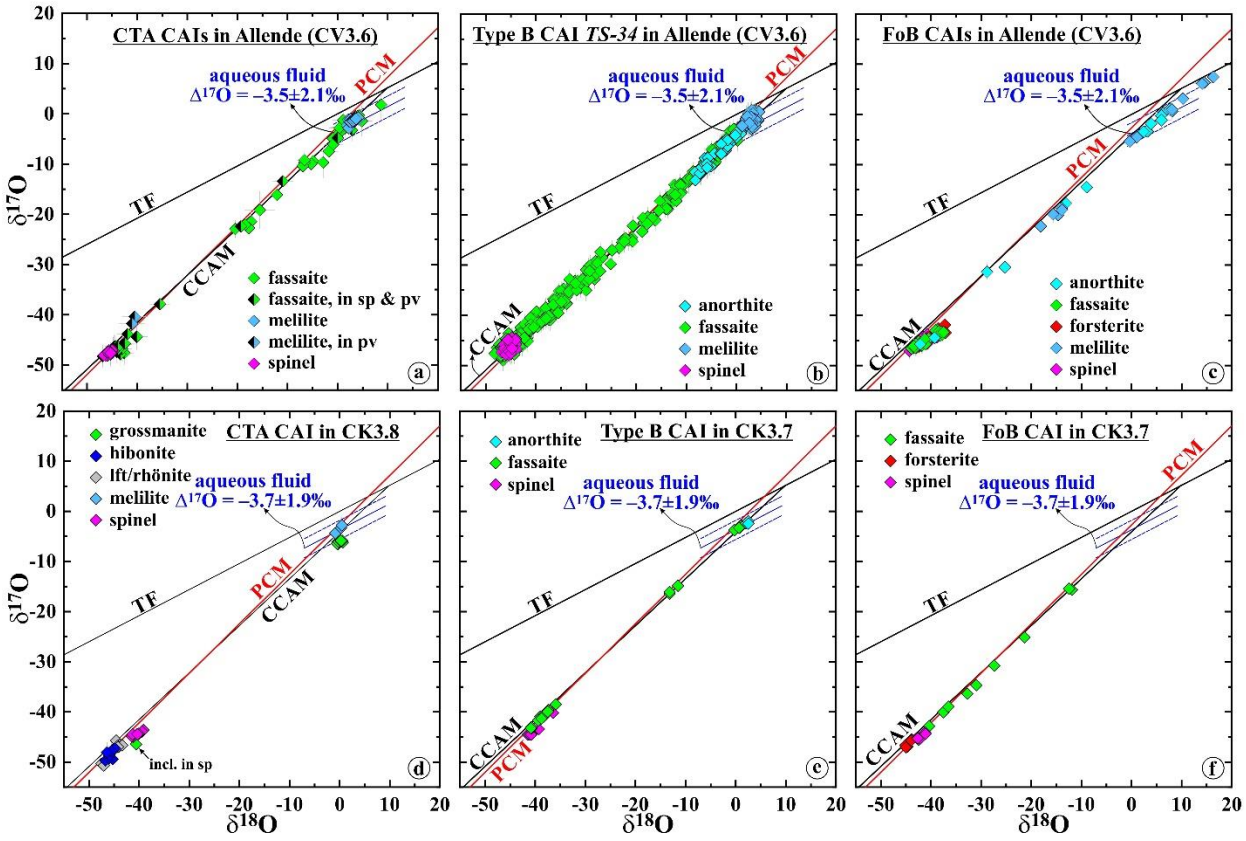

Figure SM51. $\Delta^{17}O$ *vs.* TiO_2 in pyroxenes from coarse-grained igneous CAIs in Allende (CV3.6), NWA 8418 (CV4), NWA 4964 (CK3.8), and NWA 5343 (CK3.7). In Allende CAIs, pyroxenes with TiO_2 contents < ~8 wt% have solar-like $\Delta^{17}O$; pyroxenes with higher TiO_2 are ^{16}O-delpeted to various degrees. The most Ti-rich pyroxenes have $\Delta^{17}O$ that overlap with $\Delta^{17}O$ of the Allende aqueous fluid. Inclusions of high-Ti pyroxenes inside spinel preserved ^{16}O-rich compositions. In CAIs from CK3.7–3.8 and CV4 chondrites, even low-Ti pyroxenes are ^{16}O-depleted. Data from Krot et al. (2022b) and MacPherson et al. (2023).

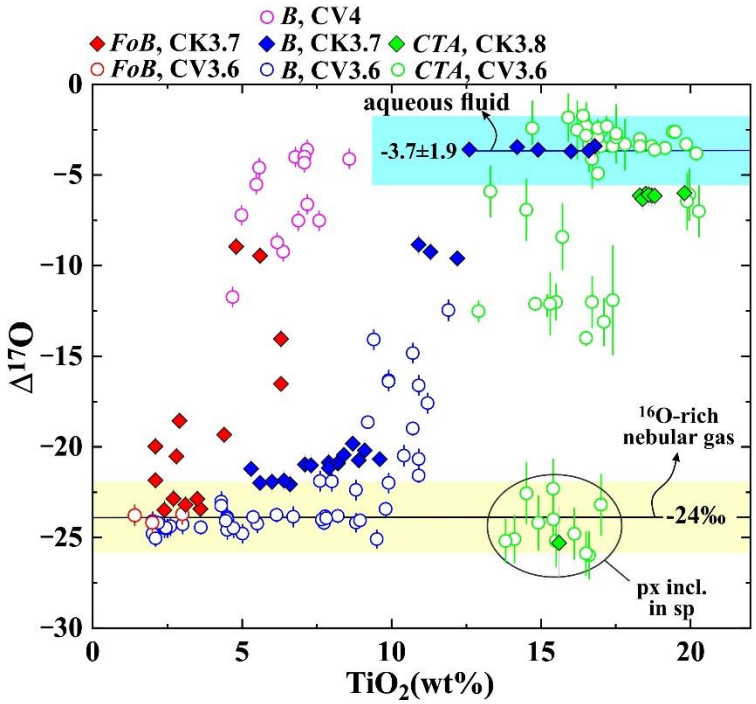

Figure SM52. Arrhenius plot of oxygen diffusion coefficients in spinel, åkermanite, gehlenite, diopside, forsterite, and anorthite under dry and wet conditions. Data from Giletti (1978), Farver (1989), Yurimoto et al. (1989), Ryerson & McKeegan (1994), and Costa & Chakraborty (2008).

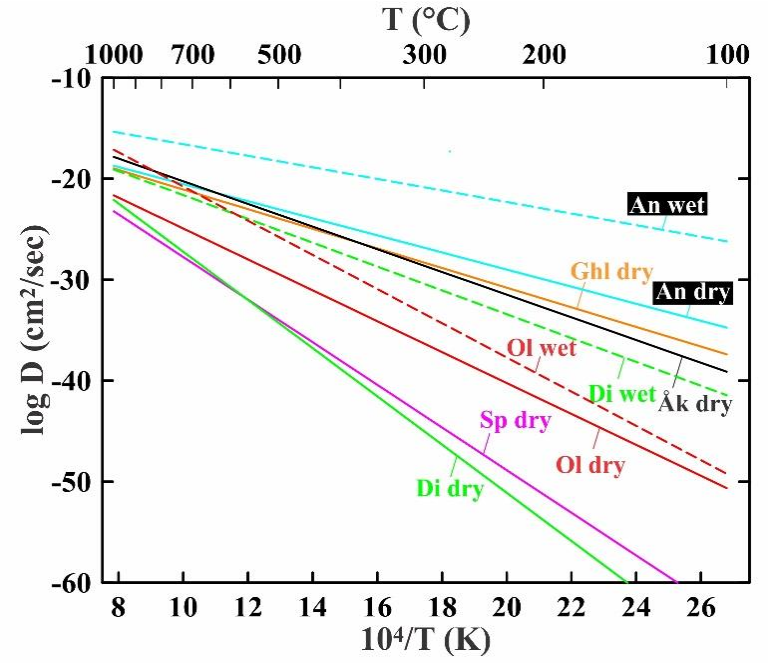

Figure SM53. $\delta^{17}O$ *vs.* $\delta^{18}O$ of primary chondrule phases and aqueously-formed magnetite and fayalite in (a) Semarkona (LL3.00), (b) Y-81020 (CO3.05), and Kaba ($CV_{oxB}3.1$). Magnetite and fayalite are out of O-isotope equilibrium with chondrule olivine and pyroxene phenocrysts. Chondrule mesostasis and plagioclase are ^{16}O-depleted relative to the phenocrysts; their $\Delta^{17}O$ values approach $\Delta^{17}O$ of fayalite and magnetite suggesting O-isotope exchange with aqueous fluid to various degrees. Data for chondrule silicates are from Kita et al. (2010), Krot et al. (2022), and Fukuda et al. (2022).

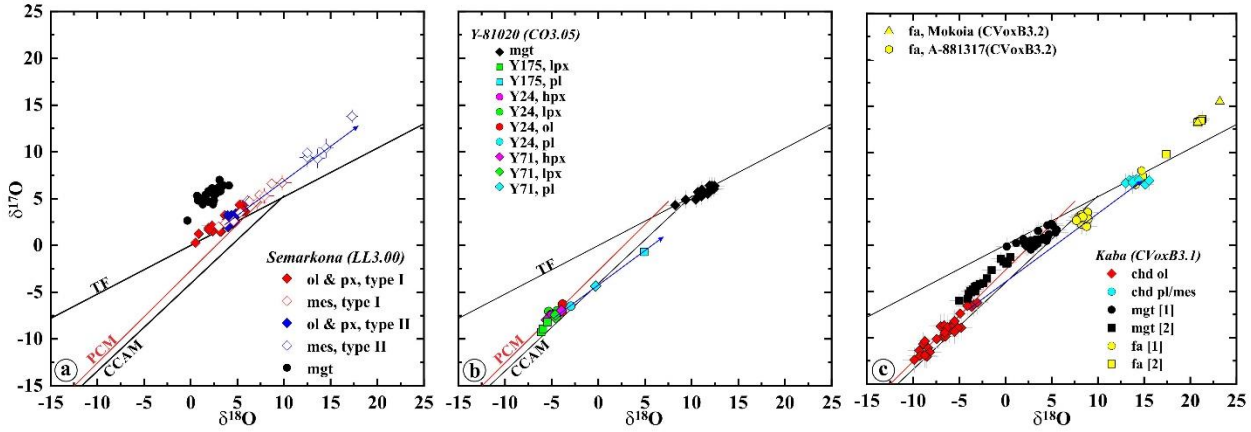

Figure SM54. Whole-rock hydrogen content (reported as 1/H in wt%) *vs.* δD of (a) UOCs and (b) CV3, CO3, and CK3−4 carbonaceous chondrites. Error bars represent 1σ standard deviations for chondrites having multiply reported hydrogen compositions (data and associated references are listed in Table SM10).

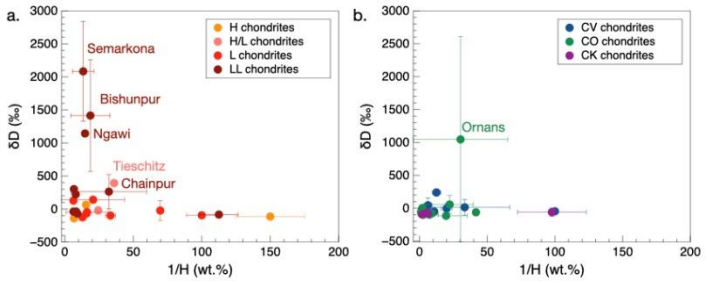

Figure SM55. (a) Positive correlation between δD and atomic C/H ratio of the IOM of UOCs. Data from Alexander et al. (2007, 2010). (b, c) NanoSIMS images showing the δD composition of the IOM of the Grosvenor Mountains (GRO) 95502 (H3.2) (a) before and (b) after a 600°C flash heating. The color-scale is the same for both images adapted from Remusat et al. (2016).

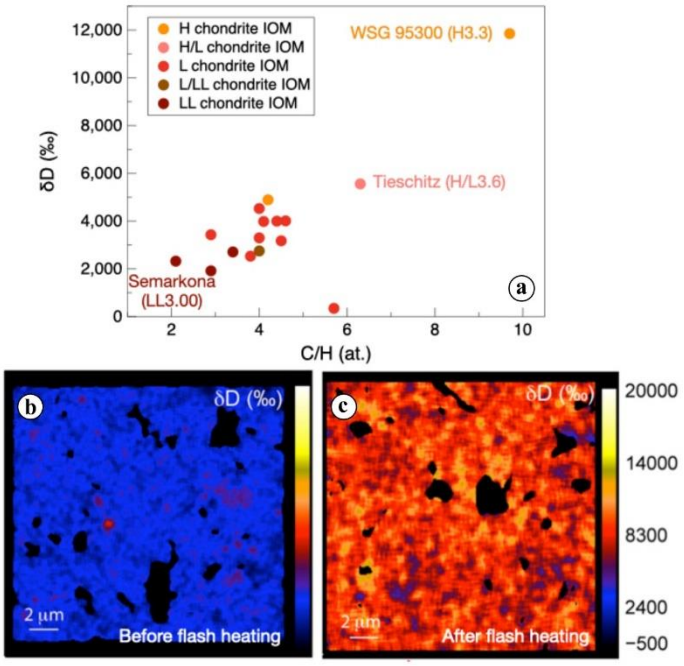

Figure SM56. NanoSIMS images of a matrix area of Semarkona (LL3.00) showing (a) the distribution of $^{13}C^-$ as a proxy for the presence of carbon-rich particles and (b) the δD distribution with the presence of a large variability and extreme δD-enrichments in C-poor areas. Adapted from Piani et al. (2015).

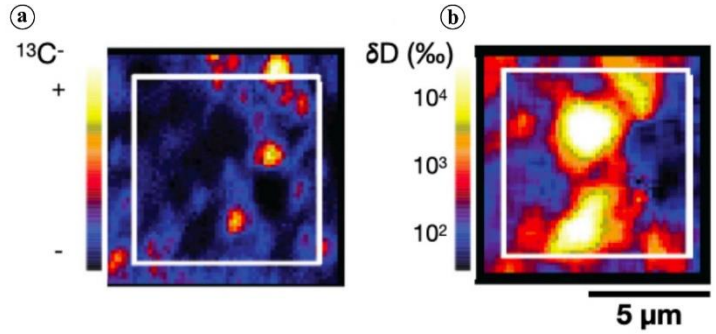

Figure SM57. BSE images of sulfides associated with aqueously formed fayalite and magnetite in Kaba ($CV_{oxB}3.1$) and NWA 3358 (H3.1). Region outlined in "a" is shown in detail in "b". (a,b) FeNi-metal nodules are oxidized and sulfidized and overgrown by clean magnetite with elongated inclusions of sulfide. (c,d) Fayalite grains overgrowing elongated sulfide grains.

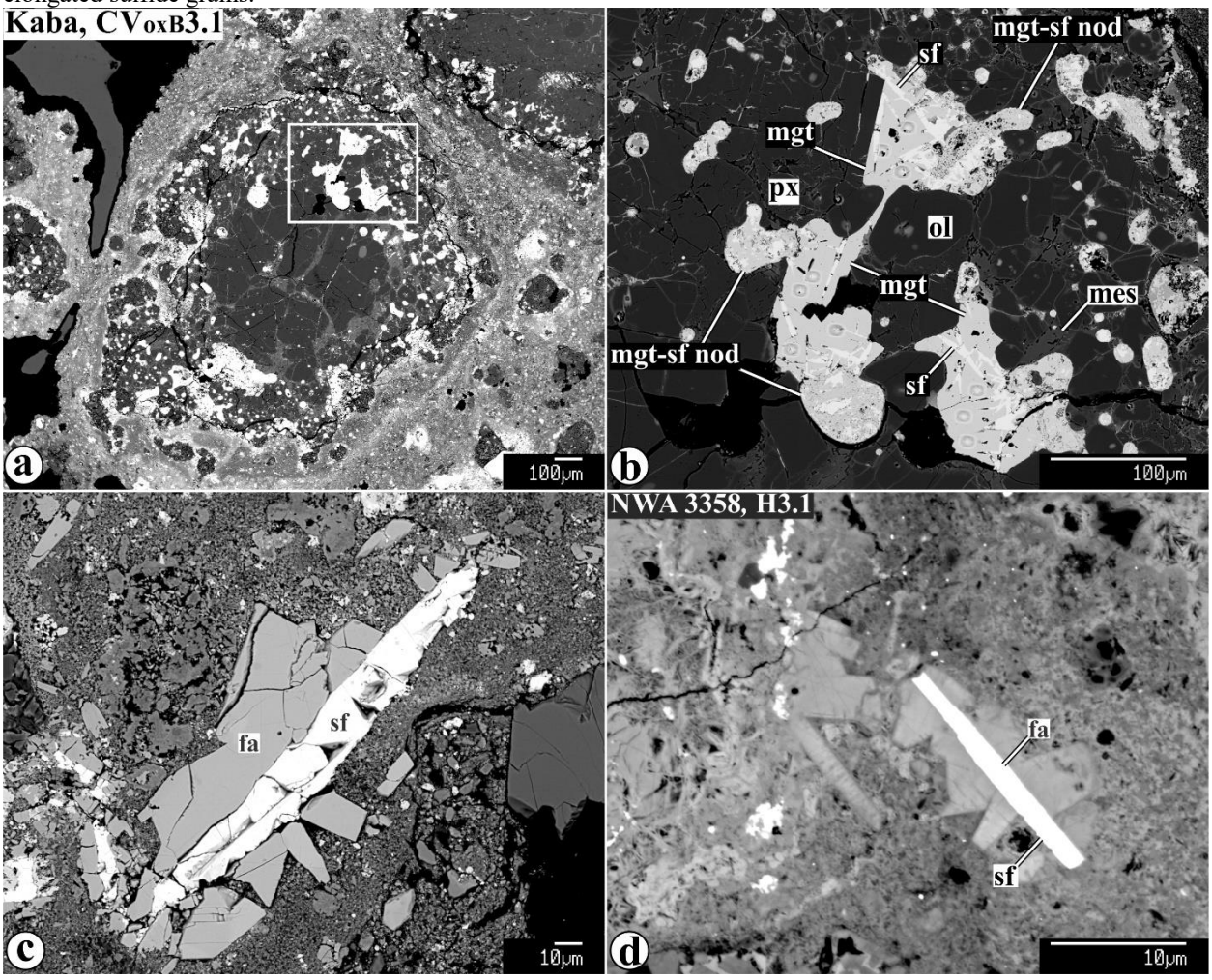

Figure SM58. Oxygen three-isotope plot for bulk CVs, matrix CVs, and dark inclusions in the Allende-like and Bali-like oxidized and reduced CVs (Clayton & Mayeda 1984, 1999; Greenwood et al. 2010) and secondary fayalite in the oxidized Bali-like CV3s (Doyle et al. 2015; Krot & Nagashima 2016; Marrocchi et al. 2018). Considering the low O-isotope fractionation factor between water and fayalite ($\alpha_{Fa\text{-}water}$) at the estimated temperatures of fayalite formation (100–200°C), $\alpha_{Fa\text{-}water}$ = −3.4 to −1.1‰ (Zheng 1993; Fig. SM59), O-isotope composition of the CV_{oxB} fayalite represents approximately that of the CV_{oxB} aqueous fluid. The main process controlling the O-isotope composition of the CV asteroid(s) is related to isotopic equilibration between ^{16}O-rich anhydrous silicates and $^{17,18}O$-rich aqueous fluid.

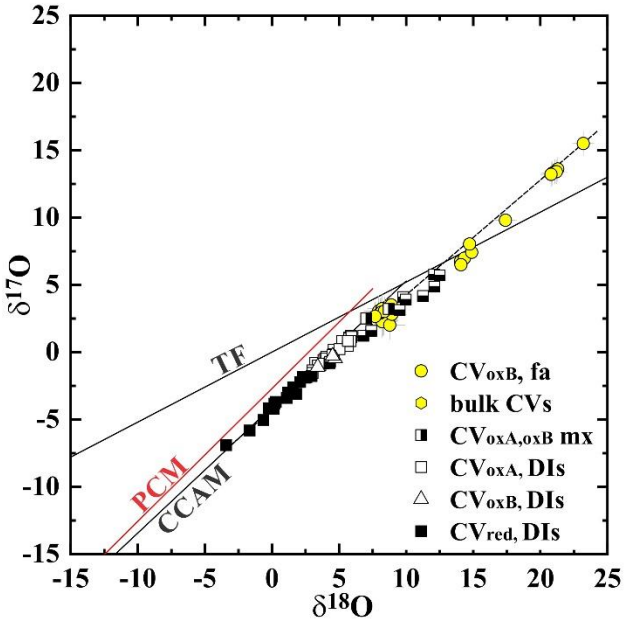

Figure SM59. Arrhenius plot of oxygen diffusion coefficients in spinel, åkermanite, gehlenite, diopside, forsterite, and anorthite under dry and wet conditions. Data from Giletti (1978), Farver (1989), Yurimoto et al. (1989), Ryerson & McKeegan (1994), and Costa & Chakraborty (2008).

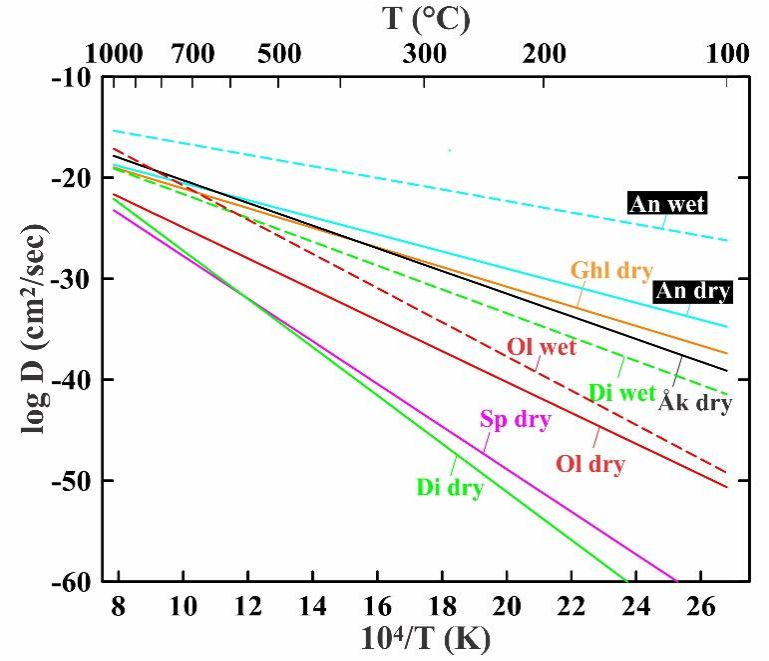

Supplementary Text 1

Gibbs free energies of Fe carbides

There are four Fe carbides – orthorhombic Fe_2C (η-carbide), hexagonal Fe_7C_3 (ε-carbide), monoclinic Fe_5C_2 (χ-carbide or Hägg carbide), and orthorhombic Fe_3C (θ-carbide or cementite, Ni-free analogue of meteoritic cohenite) – found in the Fe-C system (e.g., Agren 1979), but the thermodynamic source books (e.g., Robie & Hemingway 1995) list the standard thermodynamic data on cementite only.

The Gibbs free energy of cementite is positive at all temperatures implying that cementite is metastable relative to pure iron and carbon. Nevertheless, cementite or cohenite are found in a variety of C-bearing industrial and natural materials as well as among alteration products of Fe-rich catalysts during the Fischer-Tropsch synthesis. It is obvious that the metastable persistence of Fe_3C in natural and industrial materials is due to kinetic rather than thermodynamic factors. Therefore the previous thermodynamic analyses of mineral equilibria involving metastable cohenite as well as numerous experimental studies of Fe carburization (e.g., Pijolat et al. 1987 and references therein) may be of limited value in deciphering physicochemical formation conditions of the cohenite-bearing mineral assemblages. It appears to be more instructive to consider mineral equilibria involving other Fe-carbides if these are proved to be stable relative to Fe and C.

Chipman (1972) provides the only review of thermodynamic data on the Fe-C system which includes Fe carbides other than cementite. The standard Gibbs free energy of Hägg carbide (assumed chemical formula of $Fe_{2.2}C$) has been calculated from the experimental data of Browning et al. (1950). The apparent Gibbs free energy of the precipitates of ε-carbide (assumed chemical formula of $Fe_{2.4}C$) in α-Fe has been calculated from the experimental solubility of carbon in α-Fe. The latter value may be quite different from the standard Gibbs free energy of ε-carbide because it ignores the effect of particle size and precipitation strain. Although both Hägg and ε-carbides were correctly identified by the X-ray diffraction, their chemical formulas used by Chipman (1972) are different from those accepted to date. Here we use the experimental data of Browning et al. (1950) to calculate the standard Gibbs free energy of Hägg carbide, Fe_5C_2.

Browning et al. (1950) measured the partial pressures of H_2 (p_{H_2}) and CH_4 (p_{CH_4}) in the gaseous phase equilibrated with the α-Fe and Hägg carbide (assumed formula Fe_2C) in the temperature range of 569.45 – 632.25 K according to reaction:

$$2Fe_{(s)} + CH_{4(g)} = Fe_2C_{(s)} + 2H_{2(g)}$$

Using the correct chemical formula of Hägg carbide, this reaction must be rewritten as follows:

$$5Fe_{(s)} + 2CH_{4(g)} = Fe_5C_{2(s)} + 4H_{2(g)}$$

Then the standard Gibbs free energy of formation of Hägg carbide, $\Delta G°_f(T, Fe_5C_2)$, for any experimental run can be calculated as follows:

$$\Delta G°_f(T, Fe_5C_2) = \Delta G°_f(T, CH_4) - RT(4 ln\, p_{H2} - 2 ln\, p_{CH4}),$$

where R – gas constant and T – absolute temperature; the $\Delta G°_f(T)$ values of pure Fe and H_2 are zero by default. The least-square fit of the 23 experimental runs of Browning et al. (1950) gives the following expression for the standard Gibbs free energy of Hägg carbide:

$$\Delta G°_f(T, Fe_5C_2) = -81549 + 113.7\, T \text{ (J/mole)},$$

which reproduces the experimental data within ± 6 rel. %. The $\Delta G°_f(T, Fe_5C_2)$ is negative below 717 K implying that Hägg carbide is stable at low temperatures. The transformation of metastable Hägg carbide to metastable cementite (cohenite) would take place at ~ 850 K. Last equation is

used in thermodynamic analysis of mineral equilibria involving Hägg carbide. Although ε-carbide has been produced in Fe carburization experiments (e.g., Pijolat et al., 1987; Llorka & Casanova, 1998), it is not included in thermodynamic analysis because of insufficient thermodynamic data and lack of this carbide in type 3 chondrites.

Suppementary Text 2

Reactions for mutual replacements of metal, magnetite, cohenite, Hägg carbide, wüstite, and siderite:

(1) $5Fe_3C_{(s)} + CO_{2(g)} + 2H_{2(g)} = 3Fe_5C_{2(s)} + 2H_2O_{(g)}$

(2) $0.947\ Fe_{(s)} + H_2O_{(g)} = Fe_{0.947}O_{(s)} + H_{2(g)}$

(3) $Fe_3C_{(s)} + 6H_2O_{(g)} = Fe_3O_{4(s)} + CO_{2(g)} + 6\ H_{2(g)}$

(4) $0.947\ Fe_3C + 4.894H_2O_{(g)} = 3Fe_{0.947}O_{(s)} + 0.947CO_{2(g)} + 4.894H_{2(g)}$

(5) $3Fe_{0.947}O_{(s)} + 0.788H_2O_{(g)} = 0.947Fe_3O_{4(s)} + 0.788H_{2(g)}$

(6) $Fe_3C_{(s)} + 2CO_{2(g)} + 5H_2O_{(g)} = 3FeCO_{3(s)} + 5H_{2(g)}$

(7) $Fe_3O_{4(s)} + 3CO_{2(g)} + H_{2(g)} = 3FeCO_{3(s)} + H_2O_{(g)}$

(8) $3Fe_5C_{2(s)} + 32H_2O_{(g)} = 5Fe_3O_{4(s)} + 6CO_{2(g)} + 32H_{2(g)}$

(9) $5.28Fe_{0.947}O_{(s)} + 2CO_{2(g)} + 9.28H_{2(g)} = Fe_5C_{2(s)} + 9.28H_2O_{(g)}$

(10) $Fe_5C_{2(s)} + 3CO_{2(g)} + 9H_2O_{(g)} = 5FeCO_{3(s)} + 9\ H_{2(g)}$

Corresponding expressions for the equilibrium constants are as follows:

$log\ K_1 = log\ X_{mgt} - 4log\ (H_2O/H_2) - 3log\ X_{Fe}$

$log\ K_2 = 2log\ (H_2O/H_2) - log\ p_{CO2} - 3log\ X_{Fe}$

$log\ K_3 = 4log\ (H_2O/H_2) - 2log\ p_{CO2} - 5log\ X_{Fe}$

$log\ K_4 = 2log\ (H_2O/H_2) - log\ p_{CO2}$

$log\ K_5 = -\ 0.947log\ X_{Fe} - log\ (H_2O/H_2)$

$log\ K_6 = log\ X_{mgt} - 6log\ (H_2O/H_2) + log\ p_{CO2}$

$log\ K_7 = 0.947log\ p_{CO2} - 4.894log\ (H_2O/H_2)$

$log\ K_8 = 0.947log\ X_{Mt} - 0.788log\ (H_2O/H_2)$

$log\ K_9 = -5log\ (H_2O/H_2) - 2log\ p_{CO2}$

$log\ K_{10} = log\ (H_2O/H_2) - log\ X_{mgt} - 3log\ p_{CO2}$

$log\ K_{11} = 6log\ p_{CO2} - 32log\ (H_2O/H_2) - 5log\ X_{mgt}$

$log\ K_{12} = 9.28log\ (H_2O/H_2) - 2log\ p_{CO2}$

$log\ K_{13} = -\ 9log\ (H_2O/H_2) - 3log\ p_{CO2}$

where, X_{Fe} and X_{mgt} are atomic Fe/(Fe+Ni+Cr) ratios in metal and magnetite, respectively.

The metal-oxide and oxide-oxide reactions are independent of P_{tot} ($\Delta V_{gas} = 0$; although P_{tot} does have small effects on the values of $\log K_i$ due to small changes in ΔV_{solid} of all reactions above, these effects can be safely neglected at $P_{tot} \leq 100$ bars). In contrast, the reactions involving C-bearing compounds are pressure-dependent due to relatively large volume changes caused by either consumption or release of CO_2. As a result, the stability of Hägg carbide, cohenite and siderite relative to metallic iron and iron oxides in the Fe-C-O-H system depends upon temperature, P_{tot}, H_2O/H_2 ratio, CO_2 concentration in the gaseous phase, and atomic Fe/(Fe+Ni+Cr) ratios in metal and magnetite. Although the X_{CO2} and P_{tot} are independent parameters, each of them affects the phase boundaries in the Fe-C-O-H system in a similar fashion. The combined effect is expressed here as p_{CO2} ($p_{CO2} = X_{CO2} \times P_{tot}$).

Supplementary Text 3

Formation of pure magnetite and fayalite in association with FeNi-carbides

Fayalite and magnetite can coexist in a wide temperature range (e.g., well-known QFM buffer), therefore the key issue in the origin of the fayalite in CV, CO, and ordinary chondrites is not the temperature or redox conditions of the fayalite formation, but the mechanism of Si (and Mn) transport which results in the replacement of magnetite by fayalite at the second stage of alteration. The nebular model (Hua and Buseck 1995) of fayalite formation invokes relatively high temperature (~1300 K) necessary for the transport of gaseous SiO and H_2O/H_2 ratios much higher than those in the classic solar nebula (~10 *vs* ~0.0007) to stabilize large amounts of Fe^{2+} and oxidize Si^{2+} to Si^{4+}. Obviously, these parameters are far off the stability range of the assemblage of altered metal, magnetite, and Hägg carbide observed in chondrites (Fig. SM2). A near-equilibrium replacement of magnetite by fayalite in the nebular model would result in disappearance of both Hägg carbide and metal from the partially altered nodules, regardless of partial pressure of CO_2. The experimental data on the phase transformation among different Fe carbides (Keller 1998 and references therein) unequivocally show that Hägg carbide completely and irreversibly transforms to cohenite at temperatures higher than ~850 K. At high temperature and very oxidizing conditions required by the nebular model the metastable persistence of both cohenite and metal in association with magnetite and fayalite is highly unlikely.

Formation of both clean/pure magnetite overgrowing opaque nodules and of fayalite require the presence of an aqueous solution.

$$4Fe_{(s)} + 4H_2O_{(l,\,g)} + 2H^+_{(aq)} \rightarrow Fe_3O_{4(s)} + Fe^{2+}_{(aq)} + 5H_{2(g)}$$

$$3Fe^{2+}_{(aq)} + 4H_2O_{(l,\,g)} \rightarrow Fe_3O_{4(s)} + 6H^+_{(aq)} + H_{2(g)}$$

$$2Fe_3O_{4(s)} + 3SiO_{2(aq)} + 2H_{2(g)} = 3Fe_2SiO_{4(s)} + 2H_2O_{(g)}$$

$log\ K = 2log\ (H_2O/H_2) - 3log\ [SiO_2]$, where $log\ [SiO_2]$ is the concentration of silica in aqueous solution.

Liquid water (aqueous solution) is stable only if the partial pressure of H_2O (p_{H2O}) in the gaseous phase exceeds saturation, which is a function of temperature. Since $p_{H2O} = P_{tot} \times (1-X_{CO2})/[1 + 1/(H_2O/H_2)]$, the stability of liquid water (and an aqueous solution) therefore depends upon the P_{tot} and the composition of the gaseous phase. Following the model of a carbonaceous chondrite parent body of Grimm and McSween (1989), we assume a maximum P_{tot} in CO, CV, OC parent bodies of 100 bars; at this pressure an aqueous solution can be stable at the temperature range from ~0° (freezing point) to ~310°C (boiling point). For comparison, an increase in P_{tot} to 200 bars raises the boiling point of pure water to ~ 365°C.

Petrographic observations suggest that fayalite preferentially replaces 'pure' ($X_{mgt} = 1$) magnetite, whereas the Cr-bearing magnetite ($X_{Mt} \approx 0.98$) remains largely unaltered. This is consistent with the laws of chemical thermodynamics which predict that among several phases containing the same component (in this case, Fe_3O_4), the phase with the lower chemical potential of this component is the most stable. The chemical potential of Fe_3O_4 ($\mu_{Mt} = \mu°_{Mt} + RTlnX_{Mt}$) in the Cr-bearing magnetite at 200°C is only ~33 J/mole (0.004%) lower than that of the 'pure' magnetite, but this was enough to prevent the former from the replacement by fayalite. This is also a manifestation of the equilibrium nature of the fayalite formation which warrants the application of equilibrium thermodynamics to the analysis of this process.

To estimate physicochemical conditions of fayalite and clean magnetite formation, we superimpose the stability fields of fayalite equilibrated with an aqueous solution in the Fe-Si-O-C-H system on the stability fields of magnetite, Hägg carbide, and siderite in the aqueous solution-

free system (Fig. SMT3-1). Figure SMT3-1a shows a tiny stability field of fayalite in equilibrium with magnetite and Hägg carbide at X_{CO_2} = 10 ppmv and P_{tot} = 100 bar. At X_{CO2}> 20 ppmv no fayalite can be formed in this system. Because the stability field of Hägg carbide is X_{CO_2}-dependent, and that of fayalite is not, the stability field of fayalite increases substantially with diminishing concentration of CO_2 in the gaseous phase. For example, at X_{CO_2} = 1 ppbv (Fig. SMT3-1b) the stability field of fayalite is very large; it is limited by the freezing (~273 K) and boiling (~507 K) temperatures of the aqueous solution at the H_2O/H_2 ratio of ~0.6 or less. Figure SMT3-1b also shows that altered metal containing ~50 wt% Ni is not in equilibrium with the fayalite-magnetite-Hägg carbide assemblage. We interpret the presence of this disequilibrium mineral assemblage as a result of shielding of metal by magnetite and carbides from an aqueous solution during fayalite formation. The presence of metastable cohenite in addition to Hägg carbide implies that a brief heating of this mineral assemblage to ~850 K has partially transformed Hägg carbide to cohenite.

Figure SMT3-1. Mineral equilibria in the water-bearing Fe-C-O-H system at P_{tot} = 100 bar, X_{Fe} = 0.5, and different X_{CO_2} values. The concentration of SiO_2 in the aqueous solution equilibrated with the Allende matrix (Krot et al., 2000) is temperature-dependent: *log* [SiO_2] = 0.0039*T* – 5.677. Shaded are the areas in which the aqueous solution is not stable, and no transport of SiO_2 is possible. (A) X_{CO_2} = 10 ppmv. Metal (not shown) is stable above ~715 K. (B) X_{CO2} = 1 ppbv. The X_{CO_2} is too low to stabilize siderite at reasonable temperatures. Fayalite is not in equilibrium with the altered metal at all temperatures.

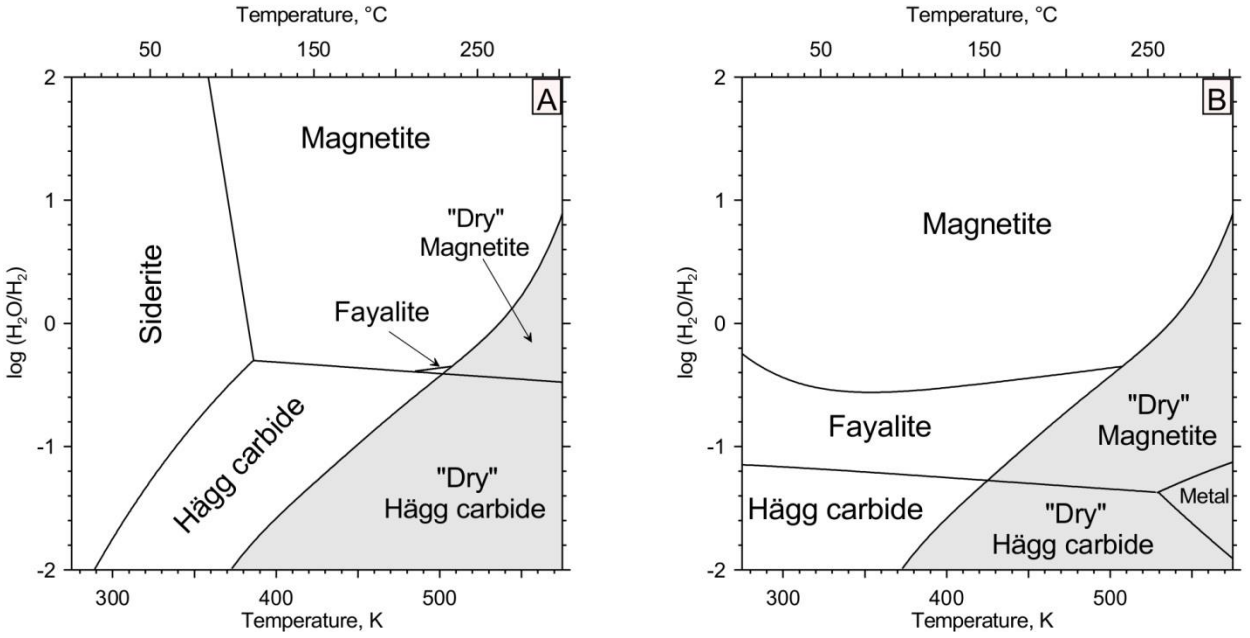

Supplementary Text 4

The thermodynamic data for solid, gaseous, and aqueous species are taken from compilations of Robie & Hemingway (1995) and Oelkers & Schott (1995), except for the gaseous H_4SiO_4 (Plyasunov 2011) and sodalite (Komada et al. 1995). The gaseous and solid solutions are treated as ideal. For the sake of temperature interpolation, the tabulated data were fitted with polynomials, with the deviation between fitted and tabulated data being typically < 0.1%. For the aqueous species, we have adopted the lowest pressure (0.004–16.55 MPa) tabulation set for the 25–350°C temperature range, with the pressure at any given temperature being equal to the partial pressure of the saturated H_2O vapor; i.e., the gaseous phase involved in alteration reactions is nearly pure H_2O steam equilibrated with an aqueous solution at any given temperature. For the same conditions, we calculated maximum concentrations of solutes in the steam and the aqueous solution formed by its condensation (Fig. SM22), using equations and regression parameters of Harvey & Bellows (1997).

To evaluate whether an observed alteration reaction can proceed via the gaseous phase only or requires a direct contact with an aqueous solution, one has to write appropriate reaction equations, calculate their intensive parameters, and compare them with each other and independent data if such exist. For example, mass-balanced equation describing replacement of melilite by grossular and Al-diopside (reaction 26) can be described by the following reaction equations:

(1*g*) $Ca_2MgSi_2O_{7(s)}+2Ca_2Al_2SiO_{7(s)} + 2H_4SiO_{4(g)} + 4CO_{2(g)} =$
$Ca_3Al_2Si_3O_{12(s)} + CaMgSiO_{4(s)} + CaAl_2SiO_{6(s)} + Ca^{2+}_{(aq)} + 4HCO_3^-{}_{(aq)} + H_{2(g)} + H_2O_{(aq)}$

$\log K_{1g} = \log[X_{di}] + \log[X_{Cts}] + \log[Ca^{2+}] + 4\log[HCO_3^-] + \log[PH_2] –$
$2\log[H_4SiO_4] – 2\log[X_{ghl}] – \log[X_{åk}] – 4\log[PCO_2]$

and

(1*aq*) $Ca_2MgSi_2O_{7(s)}+2Ca_2Al_2SiO_{7(s)} + 2SiO_{2(aq)} + 4CO_{2(g)} +3H_2O_{(aq)} =$
$Ca_3Al_2Si_3O_{12(s)} + CaMgSiO_{4(s)} + CaAl_2SiO_{6(s)} + Ca^{2+}_{(aq)} + 4HCO_3^-{}_{(aq)} + H_{2(g)},$

$\log K_{1aq} = \log[X_{di}] + \log[X_{Cts}] + 2\log[Ca^{2+}] + 4\log[HCO_3^-] –$
$2\log[SiO_2] – 2\log[X_{ghl}] – 2\log[X_{åk}] – 4\log[PCO_2]$

where *s*, *g*, and *aq* denote solid, gaseous, and aqueous species, respectively; X_{di}, $X_{CTs,}$ X_{ghl}, and $X_{åk}$ are more fractions of diopside, Ca-Tschermakite, gehlenite, and åkermanite, respectively, in Al-diopside and melilite solid solutions; P_{H2}, P_{H4SiO4}, and P_{CO2} are partial pressures of H_2, H_4SiO_4, and CO_2 in the gaseous phase dominated by H_2O; and $[Ca^{2+}]$, $[HCO_3^-]$, and $[SiO_2]$ are activities of ions and neutral species in the aqueous solution. Note, that Si and C in the reaction 1*g* are supplied via gaseous phase, but the removal of Ca requires the presence of an aqueous solution; i.e., the H_2O steam must condense to be able to dissolve the released Ca and drain it away from the reaction zone. Similar reaction equations can be written for reactions 21−32.

References

Agren J. (1979) A thermodynamic analysis of the Fe-C and Fe-N phase diagrams. Metall. Trans. 10A, 1847 – 1852.

Alexander C. M. O'D., Fogel M. L., Yabuta H., and Cody G. D. (2007) The origin and evolution of chondrites recorded in the elemental and isotopic compositions of their macromolecular organic matter. *Geochim. Cosmochim. Acta*, **71**, 4380–4403.

Alexander C. M. O'D., Newsome S. D., Fogel M. L., Nittler L. R., Busemann H., and Cody G. D. (2010) Deuterium enrichments in chondritic macromolecular material-Implications for the origin and evolution of organics, water and asteroids. *Geochim. Cosmochim. Acta*, **74**, 4417–4437.

Barosch J., Nittler L. R., Wang J., Dobrică E., Brearley A. J., Hezel D.. C., and Alexander C. M. O'D. (2022) Presolar O- and C-anomalous grains in unequilibrated ordinary chondrite matrices. *Geochim. Cosmochim. Acta*, **335**, 169–182.

Bonal L., Quirico E., Bourot-Denise M., and Montagnac G. (2006) Determination of the petrologic type of CV3 chondrites by Raman spectroscopy of included organic matter. *Geochim. Cosmochim. Acta*, **70**, 1849–1863.

Bonal L., Bourot-Denise M., Quirico E., Montagnac G., and Lewin E. (2007) Organic matter and metamorphic history of CO chondrites. *Geochim. Cosmochim. Acta*, **71**, 1605–1623.

Bose M., Zega T. J., and Williams P. (2014) Assessment of alteration processes on circumstellar and interstellar grains in Queen Alexandra Range 97416. *Earth Planet. Sci. Lett.*, **399**, 128−138.

Browning L. C., DeWitt T. W., and Emmett P. H. (1950) Equilibria in the systems Fe_2C-Fe-CH_4-H_2 and Fe_3C-Fe-CH_4-H_2. *J. Amer. Chem. Soc.*, **72**, 4211–4217.

Caffee M. W., Hohenberg C. M., Swindle T. D., and Hudson B. (1982) I-Xe ages of individual Bjurböle chondrules. *J. Geophys. Res.: Solid Earth*, **87**, A307−A317.

Chipman J. (1972) Thermodynamics and phase diagram of the Fe-C system. *Metall. Trans.*, **3**, 55–64.

Choi B.-G., McKeegan K. D., Leshin L. A., and Wasson J. T. (1997) Origin of magnetite in oxidized CV chondrites; in situ measurement of oxygen isotope compositions of Allende magnetite and olivine. *Earth Planet. Sci. Lett.*, **146**, 337–349.

Choi B.-G. and Wasson J. T. (2003) Microscale oxygen isotopic exchange and magnetite formation in the Ningqiang anomalous carbonaceous chondrite. *Geochim. Cosmochim. Acta*, **67**, 4655–4660.

Clayton R. N., Onuma N., Grossman L., and Mayeda T. K. (1977) Distribution of the presolar component in Allende and other carbonaceous chondrites. *Earth Planet. Sci. Lett.*, **34**, 209–224.

Clayton R. N. and Mayeda T. K. (1984) The oxygen isotope record in Murchison and other carbonaceous chondrites. *Earth Planet. Sci. Lett.*, **67**, 151–161.

Clayton R. N. and Mayeda T. K. (1999) Oxygen isotope studies of carbonaceous chondrites. *Geochim. Cosmochim. Acta*, **63**, 2089–2104.

Costa F. and Chakraborty S. (2008) The effect of water on Si and O diffusion rates in olivine and implications for transport properties and processes in the upper mantle. *Phys. Earth. Planet. Inter.*, **166**, 11–29.

Davidson J., Schrader D. L., Alexander C. M. O'D., Lauretta D. S., Busemann H., Franchi I. A., Greenwood R. C., Connolly H. C., Domanik K. J., and Verchovsky A. (2014a) Petrography, stable isotope compositions, microRaman spectroscopy, and presolar components of Roberts Massif 04133: A reduced CV3 carbonaceous chondrite. *Meteorit. Planet. Sci.*, **49**, 2133–2151.

Davidson J., Krot A. N., Nagashima K., Hellebrand E., and Lauretta D. S. (2014b) Oxygen isotope and chemical compositions of magnetite and olivine in the anomalous CK3 Watson 002 and ungrouped Asuka-881595 carbonaceous chondrites: Effects of parent body metamorphism. *Meteorit. Planet. Sci.*, **49**, 1456–1474.

Dobrică E. and Brearley A. J. (2011) Earliest stages of metamorphism and aqueous alteration observed in the fine-grained materials of two unequilibrated ordinary chondrites. *Lunar Planet. Sci.*, **42**, #2092.

Dobrică E. and Brearley A. J. (2020) Amorphous silicates in the matrix of Semarkona: The first evidence for the localized preservation of pristine matrix materials in the most unequilibrated ordinary chondrites. *Meteorit. Planet. Sci.*, **54**, 1973–1989.

Doyle P. M., Jogo K., Nagashima K., Krot A. N., Wakita S., Ciesla F. J., and Hutcheon I. D. (2015) Early aqueous activity on the carbonaceous and ordinary chondrite parent asteroids recorded by secondary fayalite. *Nature Commun.*, **6**, 1–10.

Doyle P. M., Jogo K., Nagashima K., Huss G. R., and Krot A. N. (2016) Mn-Cr relative sensitivity factor in ferromagnesian olivines defined for SIMS measurements with a Cameca ims-1280 ion microprobe: Implications for dating secondary fayalite. *Geochim. Cosmochim. Acta*, **174**, 102–121.

Dunn T. L., Krot A. N., and Petaev M. I. (2023) Oxygen isotope compositions of magnetite in CK3 chondrites Northwest Africa 4964 and Dar al Gani 431. *86th Meteorit. Soc. Meet.*, #6021.

Ebert S., Nagashim K., Krot A. N., and Bischoff A. (2020) Oxygen-isotope heterogeneity in the Northwest Africa 3358 (H3.1) refractory inclusions − Fluid-assisted isotopic exchange on the H-chondrite parent body. *Geochim. Cosmochim. Acta*, **282**, 98–112.

Farver J. R. (1989) Oxygen self-diffusion in diopside with applications to cooling rate determination. *Earth Planet. Sci. Lett.*, **92**, 322–330.

Floss C. and Haenecour P. (2016a) Presolar silicate abundances in the unequilibrated ordinary chondrites Meteorite Hills 00526 and Queen Alexandra Range 97008. *79th Ann. Meteorit. Soc. Meet.*, #6015.

Floss C. and Haenecour P. (2016b) Meteorite Hills (MET) 00526: An unequilibrated ordinary chondrite with high presolar grain abundances. *Lunar Planet. Sci.*, **47**, #1030.

Fukuda K., Tenner T. J., Kimura M., Tomioka N., Siron G., Ushikubo T., Chaumard N., Hertwig A. T., and Kita N. T. (2022) A temporal shift of chondrule generation from the inner to outer solar system inferred from oxygen isotopes and Al-Mg chronology of chondrules from primitive CM and CO chondrites. *Geochim. Cosmochim. Acta*, **322**, 194–226.

Giletti B. J., Semet M. P., and Yund R. A. (1978) Studies in diffusion − III. Oxygen in feldspars: an ion microprobe determination. *Geochim. Cosmochim. Acta*, **42**, 45–57.

Gilmour J. D., Whitby J. A., Turner G., Bridges J. C., and Hutchison R. (2010) The iodine-xenon system in clasts and chondrules from ordinary chondrites: Implications for early solar system chronology. *Meteorit. Planet. Sci.*, **35**, 445−455.

Greenwood R. C., Franchi I. A., Kearsley A. T., and Alard O. (2010) The relationship between CK and CV chondrites. *Geochim. Cosmochim. Acta*, **74**, 1684–1705.

Haenecour P., Floss C., Zega T. J., Croat T. K., Wang A., Jolliff B. L., and Carpenter P. (2018) Presolar silicates in the matrix and fine-grained rims around chondrules in primitive CO3.0 chondrites: Evidence for pre-accretionary aqueous alteration of the rims in the solar nebula. *Geochim. Cosmochim. Acta*, **221**, 379–405.

Harvey A. H. and Bellows J. C. (1997) Evaluation and correlation of steam solubility data for salts and minerals of interest in the power industry. *NIST Technical Note 1387.*

Hohenberg C. M. Pravdivtseva O. V., and Meshik A. P. (2004) Trapped Xe and I-Xe ages in aqueously altered CV3 meteorites. *Geochim. Cosmochim. Acta*, **68**, 4745−4763.

Holland G., Bridges J. C., Busfield A., Jeffries T., Turner G., and Gilmour J. D. (2005) Iodine-xenon analysis of Chainpur (LL3.4) chondrules. *Geochim. Cosmochim. Acta*, **69**, 189−200.

Hua X. and Buseck P. R. (1995) Fayalite in the Kaba and Mokoia carbonaceous chondrites. *Geochim. Cosmochim. Acta*, **59**, 563–578.

Itoh S., Russel S. S., and Yurimoto H. (2007) Oxygen and magnesium compositions of amoeboid olivine aggregates from Semarkona LL3.0 chondrite. *Meteorit. Planet. Sci.*, **42**, 1241−1247.

Jogo K., Nakamura T., Noguchi T., Zolotov M. Y. (2009) Fayalite in the Vigarano CV3 carbonaceous chondrite: Occurrences, formation age and conditions. *Earth Planet. Sci. Lett.*, **287**, 320−328.

Kawasaki N., Simon S. B., Grossman L., Sakamoto N., and Yurimoto H. (2018) Crystal growth and disequilibrium distribution of oxygen isotopes in an igneous Ca-Al-rich inclusion from the Allende carbonaceous chondrite. *Geochim. Cosmochim. Acta*, **221**, 318–341.

Keil K., Zucolotto M. E., Krot A. N. et al. (2015) The Vicência meteorite fall: A new unshocked (S1) weakly metamorphosed (3.2) LL chondrite. *Meteorit. Planet. Sci.*, **50**, 1089–1111.

Keller L. P. (1998) A transmission electron microscope study of iron-nickel carbides in matrix of the Semarkona unequilibrated ordinary chondrite. *Meteorit. Planet. Sci.*, **33**, 913–919.

Kita N. T., Nagahara H., Tachibana S., Tomomura S., Spicuzza M. J., Fournelle J. H., and Valley J. W. (2010) High precision SIMS oxygen three isotope study of chondrules in LL3 chondrites: role of ambient gas during chondrule formation. *Geochim. Cosmochim. Acta*, **74**, 6610–6635.

Komada N., Westrum E. F. Jr. Hemingway B. S., Zolotov M. Y., Semenov Y. V., Khodakovsky I. L., and Anovitz L. M. (1995) Thermodynamic properties of sodalite at temperatures from 15 K to 1000 K. *J. Chem. Thermodynamics*, **27**, 1119−1132.

Krot A. N., Zolensky M. E., Keil K., Scott E. R. D., and Nakamura K. (1998) Secondary Ca-Fe-rich minerals in the Bali-like and Allende-like oxidized CV3 chondrites and Allende dark inclusions. *Meteorit. Planet. Sci.*, **33**, 623–645.

Krot A. N., Brearley A. J., Petaev M. I., Kallemeyn G. W., Sears D. W. G., Benoit P. H., Hutcheon I. D., Zolensky M. E., and Keil K. (2000) Evidence for *in situ* growth of fayalite and hedenbergite in MacAlpine Hills 88107, ungrouped carbonaceous chondrite related to CM-CO clan. *Meteorit. Planet. Sci.*, **35**, 1365−1387.

Krot A. N., Petaev M. I., Meibom A., and Keil K. (2001) *In situ* growth of Ca-rich rims around Allende dark inclusions. *Cosmochemical Issue of Geochemistry International* **36**, 351–368.

Krot A. N., Nagashima K., Hutcheon I. D., Ishii H. A., Yin Q.-Z., Davis A. M., and Simon S. B. (2010) Mineralogy, petrography, oxygen and magnesium isotopic compositions and formation age of grossular-bearing assemblages in the Allende CAIs. *Lunar Planet. Sci.*, **41**, #1406.

Krot A. N., Keil K., Goodrich C., Weisberg M. K., and Scott E. R. D. (2014a) Classification of meteorites. In *Meteorites and Cosmochemical Processes* (ed. A.M. Davis) Vol. 1, *Treatise on Geochemistry* (eds. H. D. Holland and K. K. Turekian), Elsevier, Oxford, pp. 1–63.

Krot A. N. and Nagashima K. (2016) Evidence for oxygen-isotope exchange in chondrules and refractory inclusions during fluid-rock interaction on the CV chondrite parent body. *78th Ann. Meteorit. Soc. Meet.*, #6014.

Krot A. N., Nagashima K., Simon S. B., Ma C., Connolly H. C. Jr., Huss G. R., Davis A. M., and Bizzarro M. (2019a) Mineralogy, petrography, and oxygen and aluminum-magnesium isotope systematics of grossite-bearing refractory inclusions. *Geochemistry*, **79**, 125529.

Krot A. N., Ma C., Nagashima K., Davis A. M., Beckett J. R., Simon S. B., Komatsu M., Fagan T. J., Brenker F., Ivanova M. A., and Bischoff A. (2019b) Mineralogy, petrography, and oxygen isotopic compositions of ultrarefractory inclusions from carbonaceous chondrites. *Geochemistry*, **79**, 125519.

Krot A. N., Petaev M. I., and Nagashima K. (2021) Infiltration metasomatism of the Allende coarse-grained calcium-aluminum-rich inclusions. *Progress Earth Planet. Sci.*, **8**, 61.

Krot A. N., Doyle P., Nagashima K., and Dobrică E. (2022a) Mineralogy, petrology and oxygen-isotope compositions of magnetite±fayalite assemblages in CO3, CV3 and LL3 chondrites. *Meteorit. Planet. Sc.*, **57**, 392–428.

Krot A. N., Nagashima K., MacPherson G. J., and Ulyanov A. A. (2022b) On the nature of oxygen-isotope heterogeneity of igneous calcium-aluminum-rich inclusions in CV carbonaceous chondrites. *Geochim. Cosmochim. Acta*, **332**, 327–354.

Krot A. N., Nagashima K., Dunn T, L., Petaev M. I., and Ma C. (2023) Mineralogy, petrography, oxygen- and aluminum-magnesium isotope systematics of igneous CAIs from CK3 chondrites. *86th Meteoritic. Soc. Meet.*, #6116.

Krot A. N., Dunn T. L., Petaev M. I., Ma C., Nagashima K., and Zipfel J. (2024) Metasomatic alteration of coarse-grained igneous calcium-aluminum-rich inclusions from CK3 carbonaceous chondrites. *Meteorit. Planet. Sci.*, **59**, 809–835.

Llorca J. and Casanova I. (1998) Formation of carbides and hydrocarbons in chondritic interplanetary dust particles: A laboratory study. *Meteorit. Planet. Sci.*, **33**, 243–251.

MacPherson G. J., Nagashima K., Krot A. N., Doyle P. M., and Ivanova M. A. (2017) ^{53}Mn-^{53}Cr chronology of Ca-Fe silicates in CV3 chondrites. *Geochim. Cosmochim. Acta*, **201**, 260–274.

MacPherson G. J., Nagashima K., Krot A. N., Kuehner S. M., Irving A. J., Ziegler K., Mallozzi L., Corrigan C., and Pitt D. (2023) Northwest Africa 8418: The first CV4 chondrite. *Meteorit. Planet. Sci.*, **58**, 135–157.

Marrocchi Y., Chaussidon M., Piani L., and Libourel G. (2016) Early scattering of the solar protoplanetary disk recorded in meteoritic chondrules. *Sci. Adv.*, **2**, 11601001.

Marrocchi Y., Bekaert D. V., and Piani L. (2018) Origin and abundance of water in carbonaceous asteroids. *Earth Planet. Sci. Lett.*, **482**, 23–32.

McKeegan K. D., Leshin L. A., Russel S. S., and MacPherson G. J. (1998) Oxygen isotopic abundances in calcium-aluminum-rich inclusion from ordinary chondrites: Implications for nebular heterogeneity. *Science*, **280**, 414–418.

McKeegan K. D., Kallio A. P. A., Heber V. S., Jarzebinski G., Mao P. H., Coath C. D., Kunihiro T., Wiens R. C., Nordholt J. E., Moses R. W., Jr., Reisenfeld D. B., Jurewicz A. J. G., and Burnett D. S. (2011) The oxygen isotopic composition of the Sun inferred from captured solar wind. *Science*, **332**, 1528–1532.

Nagashima K., Huss G. R., Krot A. N., and Yurimoto H. (2011) Disturbance of magnesium isotopes in anorthite from an Allende CAI inferred from magnesium isotope mapping with isotope microscope. *Lunar Planet. Sci.*, **42**, #2447.

Nguyen, A. N., Nittler, L. R., Stadermann, F. J., Stroud, R. M. and Alexander, C. M. O'D. (2010) Coordinated analyses of presolar grains in the Allan Hills 77307 and Queen Elizabeth Range 99177 meteorites. *Astrophys. J.*, **719**, 166–189.

Nittler L. R., Alexander C. M. O'D., Davidson J., Riebe M. E. I., Stroud R. M. and Wang J. (2018) High abundances of presolar grains and ^{15}N-rich organic matter in CO3.0 chondrite Dominion Range 08006. *Geochim. Cosmochim. Acta*, **226**, 107– 131.

Oelkers E. H. and Schott J. (1995) Experimental study of anorthite dissolution and the relative mechanism of feldspar hydrolysis. *Geochim. Cosmochim. Acta*, **59**, 5039–5053.

Petaev M. I. and Mironenko M. V. (1997) Thermodynamic modeling of aqueous alteration in CV chondrites. In *Workshop on Parent-body and Nebular Modification of Chondritic Materials* (eds. Zolensky M. E., Krot A. N. and Scott E. R. D.), LPI Technical Report 97-02, 49–50.

Piani L., Robert F., and Remusat L. (2015) Micron-scale D/H heterogeneity in chondrite matrices: A signature of the pristine solar system water? *Earth Planet. Sci. Lett.*, **415**, 154–164.

Pijolat M., Perrichon V., and Bussière P. (1987) Study of carburization of an iron catalyst during the Fischer-Tropsch synthesis: Influence on its catalytic activity. *J. Catalysis*, **107**, 82–91.

Plyasunov A. V. (2011) Thermodynamic properties of H_4SiO_4 in the ideal gas state as evaluated from experimental data. *Geochim. Cosmochim. Acta*, **75**, 3853–3865.

Pohl L. and Britt D. T. (2020) Strengths of meteorites—An overview and analysis of available data. *Meteorit. Planet. Sci.*, **55**, 962−987.

Pravdivtseva O. V., Amelin Y., Hohenberg C. M., and Meshik A. P. (2002) I–Xe and Pb–Pb ages of Richardton chondrules. *Geochim. Cosmochim. Acta*, **66**, A614.

Pravdivtseva O. V., Krot A. N., Hohenberg C. M., Meshik A. P., Weisberg M. K., and Keil K. (2003) The I-Xe record of alteration in the Allende CV chondrite. *Geochim. Cosmochim. Acta*, **67**, 5011−5026.

Pravdivtseva O. V., Meshik A. P., and Hohenberg C. M. (2004a) The I–Xe record of long equilibration in chondrules from the unnamed Antarctic meteorite L3/LL3. In *Workshop on Chondrites and the Protoplanetary Disk*, #9069.

Pravdivtseva O. V., Amelin Y., Meshik A. P., and Hohenberg C. M. (2004b) I–Xe and Pb–Pb ages of individulal Elenovka (L5) chondrules. *Geochim. Cosmochim. Acta*, **68**, A760.

Pravdivtseva O. V., Hohenberg C. M., and Meshik A. P. (2005a) I–Xe dating: The time line of chondrule formation and metamorphism in LL chondrites. *Lunar Planet. Sci.*, **36**, #2354.

Pravdivtseva O. V., Hohenberg C. M., and Meshik A. P. (2005b) New I–Xe ages of chondrules from the NWA 267 (H4) meteorite. *68th Ann. Meteorit. Soc. Meet.*, #5234.

Pravdivtseva O. V., Meshik A. P., Hohenberg C. M., and Amelin Y. (2006a) New I–Xe ages of chondrules from the ordinary L4 chondrite Saratov. *Lunar Planet. Sci.*, **37**, #2418.

Pravdivtseva O. V., Meshik A. P., and Hohenberg C. M. (2006b) New I–Xe ages of chondrules from the L4 Bjurböle meteorite. *69th Ann. Meteorit. Soc. Meet.*, #5302.

Pravdivtseva O. V., Meshik A. P., and Hohenberg C. M. (2010) I-Xe in magnetic fractions of two ungrouped C2 and C3 carbonaceous chondrites. *73rd Ann. Meteorit. Soc. Meet.*, #5408.

Pravdivtseva O. V., Meshik A. P., and Hohenberg C. M. (2013) The I-Xe record: Early onset of aqueous alteration in magnetites separated from CM and CV carbonaceous chondrites. *Lunar Planet. Sci.*, **49**, #3104.

Pravdivtseva O., Meshik A., Tissot F. L. N., and Dauphas N. (2018) I−Xe studies of aqueous alteration in the Allende CAI Curious Marie. *Lunar Planet. Sci.*, **49**, #2959.

Pravdivtseva O., Meshik A., Tissot F. L. N., and Dauphas N. (2020) Xenon isotopic studies of aqueous alteration in fine-grained Allende CAIs. *Lunar Planet. Sci.*, **51**, #2326.

Robie R. A. and Hemingway B. S. (1995) Thermodynamic properties of minerals and related substances at 298.15 K and 1 bar (10^5 Pascals) pressure and at higher temperatures. *U. S. Geol. Survey Bull.*, **2131**, 461−461

Remusat L., Piani L., and Bernard S. (2016) Thermal recalcitrance of the organic D-rich component of ordinary chondrites. *Earth Planet. Sci. Lett.*, **435**, 36−44.

Ryerson F. J. and McKeegan K. D. (1994) Determination of oxygen self-diffusion in åkermanite, anorthite, diopside, and spinel: Implications for oxygen isotopic anomalies and the thermal histories of Ca-Al-rich inclusions. *Geochim. Cosmochim. Acta*, **58**, 3713–3734.

Schönbächler M., Theis K. J., Crowther S. A., and Gilmour J. D. (2014) Iodine-xenon systematics of mineral separates from the ordinary chondrite Allegan and the acapulcoite Dhofar 125. *77th Ann. Meteorit. Soc. Meet.*, #5325.

Smith L. R., Haenecour P., Barnes J., Dominik K., Neuman M., Wang K., Ogliore R., and Koefoed P. (2023) Abundance of presolar grains in the C3.00-ungrouped chondrite Chwichiya 002. *Lunar Planet. Sci.*, **54**, #2425.

Swindle T. D., Caffee M. W., and Hohenberg C. M. (1988) I-Xe studies of Allende inclucions: EGGs and the Pink Angel. *Geochim. Cosmochim. Acta*, **52**, 2215–2229.

Swindle T. D., Caffee M. W., Hohenberg C. M., Lindstrom M. M., and Taylor G. J. (1991a) Iodine–xenon studies of petrographically and chemically characterized Chainpur chondrules. *Geochim. Cosmochim. Acta*, **55**, 861−880.

Swindle T. D., Grossman J. N., Olinger C. T., and Garrison D. H. (1991b) Iodine–xenon, chemical, and petrographic studies of Semarkona chondrules: evidence for the timing of aqueous alteration. *Geochim. Cosmochim. Acta*, **55**, 3723−3734.

Swindle T. D., Cohen B., Li B., Olson E., Krot A. N., Birjukov V. V., and Ulyanov A. A. (1998) Iodine-xenon studies of separated components of the Efremovka (CV3) meteorite. *Lunar Planet. Sci.*, **29**, #1005.

Ushikubo T., Kimura M., Kita N. T., and Valley J. W. (2012) Primordial oxygen isotope reservoirs of the solar nebula recorded in chondrules in Acfer 094 carbonaceous chondrite. *Geochim. Cosmochim. Acta*, **90**, 242–264.

Vollmer C., Hoppe P., Stadermann F. J., Floss C., and Brenker F. E. (2009) NanoSIMS analysis and Auger electron spectroscopy of silicate and oxide stardust from the carbonaceous chondrite Acfer 094. *Geochim. Cosmochim. Acta*, **73**, 7127–7149.

Ushikubo T., Tenner T. J., Hiyagon H., and Kita N. T. (2017) A long duration of the ^{16}O-rich reservoir in the solar nebula, as recorded in fine-grained refractory inclusions from the least metamorphosed carbonaceous chondrites. *Geochem. Cosmochim. Acta*, **201**, 103–122.

Yurimoto H., Morioka M., and Nagasawa H. (1989) Diffusion in single crystals of melilite. I – Oxygen. *Geochim. Cosmochim. Acta*, **53**, 2387–2394.

Yurimoto H., Koike O., Nagahara H., Morioka M., and Nagasawa H. (2000) Heterogeneous distribution of Mg isotopes in anorthite single crystal from Type B CAIs in Allende meteorite. *Lunar Planet. Sci.*, **31**, #1593.

Zheng Y.-F. (1993) Calculation of oxygen isotope fractionation in anhydrous silicate minerals. *Geochem. Cosmochim. Acta*, **57**, 1079–1091.